Contribution to the Study of Magnetic Properties of Fe-Zr-Nb-B based nanocrystalline Ribbons and Thin Films

Salil Modak

ENSC-2008 N° 141

THESE DE DOCTORAT
DE L'ECOLE NORMALE SUPERIEURE DE CACHAN

Présentée par

Monsieur **Salil MODAK**

pour obtenir le grade de

DOCTEUR DE L'ECOLE NORMALE SUPERIEURE DE CACHAN

Domaine :

SCIENCES PHYSIQUES

Sujet de la thèse :

Contribution à l'étude des propriétés magnétiques d'alliages nanocristallins Fe-Zr-Nb-B sous forme de rubans et de couches minces

Thèse présentée et soutenue à Cachan le 22 décembre 2008 devant le jury composé de :

Nirina RANDRIANANTOANDRO	Professeur à l'université du Maine	Président
Fransisco ALVES	Professeur à l'université Paris XI	Rapporteur
Olivier ISNARD	Professeur à l'université Joseph Fourier	Examinateur
Marco COÏSSON	Chercheur à l'INRIM, Turin, Italie	Examinateur
Shashank KANE	Reader - Devi Ahilya University, Indore, Inde	Directeur de thèse
Frédéric MAZALEYRAT	Maître de conférences à université Paris XII	Directeur de thèse

Laboratoire des Systémes et Applications de Technologies de l'Information et de l'Énergie
(SATIE)
(ENS CACHAN/CNRS/UMR 8029)
61, avenue du Président Wilson, 94235 CACHAN CEDEX (France)

Contribution to the Study of Magnetic Properties of Fe-Zr-Nb-B based nanocrystalline Ribbons and Thin Films

Thesis submitted by

Salil Modak

For Partial Fulfillment of the Requirements for the

Degree of Doctor of Philosophy at Ecole Normale Superieure de Cachan

Cachan, France 2008

Remerciements

Il est difficile d'évaluer la contribution d'une mère au succès de son fils et il est tout aussi difficile de la payer en retour. A ma mère dotée de toutes les qualités, j'offre cette thèse, modeste témoignage de ma reconnaissance pour tout ce qu'elle m'a donné.

Merci Aai d'être ma mère ! Merci Baba, pour l'amour, la liberté, la confiance et la discipline dont tu m'as entouré. Merci mon cher frère Vaibhav, toi avec lequel j'ai partagé travail et responsabilités dans notre vie quotidienne à Indore. J'exprime aussi toute ma gratitude à ma femme Deepali pour son amour, sa compréhension et son soutien. Merci Deepali pour m'avoir incité à quitter la vie confortable d'un étudiant doctorant. J'adresse enfin mes remerciements à tous les membres de ma famille pour l'affection, les soins et la fierté qu'ils m'ont témoignés.

Les mots sont insuffisants pour exprimer ma gratitude envers mes professeurs. Dr. Shashank N. Kane, Reader, School of Physics Devi Ahilya Université d' Indore, Inde et Dr. Frederic Mazaleyrat, Maitre de Conférence, laboratoire SATIE, ENS de Cachan, France. Sans eux ce travail n'aurait pas abouti. Je les remercie ici de tout mon cœur de m'avoir guidé et encouragé dans ma recherche.

J'ai été émerveillé par les compétences du Dr. Frederic Mazaleyrat qui n'a jamais manqué de me fournir explications, idées et suggestions lors de nos discussions. J'adresse ma très profonde gratitude au Dr. Shashank N. Kane qui m'a toujours encouragé à aller plus loin et m'a aidé dans toutes les étapes de mon travail. Merci, monsieur, pour votre amabilité et votre compréhension. Je voudrais aussi remercier très sincèrement mon co directeur de thèse Prof. Ajay Gupta, Directeur du Centre UGC-DAE-CSR, pour m'avoir dirigé avec efficacité et permis de profiter des équipements du laboratoire UGC-DAE-CSR, Indore, Inde.

J’adresse mes sincères remerciements à la France et aux Français qui m’ont permis d’exprimer ma créativité, ma pratique professionnelle dans le respect de l’identité de chacun. Je voudrais remercier mes parents français, Gérard et Jacqueline Delaporte pour toute leur affection. Au moment où je quitte la France pour retourner dans mon pays, je me rends compte que j’ai appris beaucoup de ce grand pays et de sa culture mais ce qui me semble encore plus important, c’est que j’ai appris à mieux apprécier ce qui fait la grandeur de l’Inde et en particulier sa spiritualité.

Merci au Prof. Sylvain Allano (ex directeur) et au professeur Pascal Larzabal, directeur actuel du laboratoire SATIE qui m’ont donné accès à tous les équipements du laboratoire. Merci aussi au Prof Richard Barrué et au Prof François Costa de m’avoir accepté dans leur équipe.

Mes remerciements ne seraient pas complets si je ne mentionnais pas ceux que j’adresse au Dr. Martino Lobue pour son soutien, ses discussions fructueuses et ses suggestions qui m’ont permis d’avoir une vue plus claire dans la pratique de ma recherche. Merci au Dr. Mehdi Ammar pour m’avoir aidé pour de nombreuses questions pratiques durant la première année de mon séjour en France. Il a été un ami dévoué et efficace. Merci aussi au M. Arnaud Brosseau, laboratoire PPSM, ENS de Cachan, qui m’ont beaucoup aidé pour les mesures de l’AFM et de le DSC. Mes remerciements vont aussi au Dr.Vincent Loyau pour nos discussions utiles. Je n’oublierai pas le Dr. Gérard Chaplier, pour ses amicales tasses de café et sa question : « combien de pages ?»

Je suis reconnaissant à madame Bogdana Neuville, directrice des Relations Internationales, et à son équipe de m’avoir aidé dans toutes les démarches administratives.

Je voudrais adresser des remerciements particuliers au Pr Lajos Varga, RISSPO, Académie des Sciences, Budapest, Hongrie, pour ses suggestions et ses idées inestimables qui m’ont beaucoup aidé dans les mesures de la diffraction des rayons X et de l’ hysteresis.

Je suis aussi très reconnaissant aux professeur Franco Vinai et au Dr. Paola Tiberto, division Electromagnétique, INRIM, Italie, de m'avoir donné l'opportunité de travailler dans leur grand groupe de recherche magnétisme. Ma profonde gratitude va aussi au Dr. Marco Coïsson, Chercheur, division électromagnétique, INRIM, Italie, pour son total soutien et sa coopération dans tous les domaines. Sans son aide et ses suggestions très pertinentes cette thèse ne serait pas ce qu'elle est aujourd'hui. Merci à madame Frederica Celegato pour son aide dans la préparation de couches fines utilisant RF sputtering à INRIM, Italie.

Je voudrais aussi exprimer toute ma gratitude à Mr. Satish Poddar et Mlle Mona Gehlot pour son aide dans la préparation et la caractérisation des échantillons en couches minces utilisant IBS, à UGC-DAE-CSR Indore, Inde. Je suis reconnaissant à mes collègues Mr. Nandkishore Ghodke et Mr. Shailendra Singh Khinchi d'avoir su créer une très bonne ambiance de travail à Indore.
Je voudrais remercier mes fidèles amis Dr. Rajneesh Atre, Amit Goswami et Sagar Arondekar pour leurs encouragements constants et leur confiance.

La bourse reçue grâce au programme des bourses de l'ENS pour les étudiants étrangers, au titre de l'année universitaire 2005 -2006 et le salaire du CNRS, contrat de travail no. 94/07 Int 345 en 2007 -2008 m'ont permis de faire cette thèse et je suis reconnaissant aux instances qui me les ont attribués.

Bien des personnes ou des groupes ont grandement contribué, qu'ils le sachent ou non, à mon travail. Que tous ces anonymes soient aussi remerciés, Merci à tous.

Acknowledgements

The contributions of a mother to the success of her child can be neither measured nor directly repaid. To such a mother, who is but a manifestation of the divine qualities of the earth, this thesis is one small offering. Thank you Aai for being my mother! Thank you Baba for all the love, freedom, prosperity, confidence and discipline showered on me. Thanks to my dear brother Vaibhav who shared a lot of work and responsibilities of day to day life at Indore. And at last but not the least I am thankful to my wife Deepali for her love, understanding, and support and specially for inciting me to finally say a quick goodbye to the cozy and comfortable life of a Ph.D. candidate. Thanks are due to rest of the family members for all the love, care and pride.

Words are simply not enough for expressing gratitude towards my supervisors Dr. Shashank N. Kane, Reader, School of Physics Devi Ahilya University Indore, India and Dr. Frederic Mazaleyrat, Maitre de Conference, SATIE Laboratory, ENS de Cachan, France. Without them this work would have not reached success. I thank them deeply for providing me invaluable guidance as well as the mental support and encouragement in the research work. I arrived to be amazed by the technical expertise of Dr. Frederic Mazaleyrat, who never provided room for a vacuum of explanations of ideas through discussions and suggestions. A special mention of my deepest gratitude towards my supervisor Dr. Shashank N. Kane who encouraged me to go ahead and helped me through all the stages of this work, Thank you very much sir for your understanding and kindness. I would also like to thank sincerely to my co-supervisor Prof. Ajay Gupta, Center Director for UGC DAE CSR for his timely guidance, suggestions and providing an opportunity to use the facilities in his laboratory at UGC DAE CSR Indore India.

My sincere thanks are due to the France and her people for providing a platform to express creativity and practice professionalism while retaining one's own identity. I would like to thank my French Parents Gerard and Jacquline Delaporte for all the love and warmth. As I leave France and return to my motherland, India, I realize that not only have I learnt a lot from the work culture of this great country but, more importantly, I have been able to better understand and appreciate the greatness of India, especially her spirituality. I am grateful to Prof. Sylvain Allano (ex-director) and Prof. Pascale Larzabal, current director SATIE Laboratory, for providing me the opportunity for using all the facilities that are available. I also thank Prof. Richard Barrue and Prof. Francois Costa for accepting me as a member of their team. This note would be incomplete if I do not mention my thanks to Dr. Martino Lobue for his support and many helpful discussions and suggestions that helped me to develop a clear approach towards research. Thanks to Dr. Mehdi Ammar for helping me with lots of practical aspects during my first year of stay in France, he has been a good friend very kind and helping.

I thank Mr. Arnaud Brosseau, PPSM laboratory, ENS de Cachan, for the help with AFM and DSC measurements.Thanks are due to Dr. Vincent Loyau for some useful discussions. I will not forget Dr. Gerard Chaplier for, all the friendly cups of coffee and the question, "How many Pages"?

I am thankful to Madame Bogdana Neuville, Director, International Affairs, ENS de Cachan and her team for helping me with all the official procedures.

I would like to express sincere and special thanks to Prof. Lajos Varga, RISSPO, Hungarian Academy of Sciences, Budapest, Hungary, for his invaluable suggestions, ideas and help with hysteresis and X-ray diffraction measurements.

I am also thankful to Prof. Franco Vinai and Dr. Paola Tiberto, Electromagnetic division, INRIM Italy, for giving me an opportunity to work in their multi faced magnetic research group. I deeply acknowledge Dr. Marco Coisson, Researcher, Electromagnetic division, INRIM, Torino, Italy, for his wholesome support and co-operation in all aspects. I am grateful to him as without his valuable suggestions and help this thesis wouldn't have taken the present form. Thanks to Ms. Frederica Celegato for all the help in preparation of thin film samples using RF sputtering at INRIM, Italy.

I would also like to express my appreciation to Mr. Satish Poddar and Ms. Mona Gehlot for the help in preparing and characterizing the thin film samples using ion beam sputtering and XRR at UGC DAE CSR Indore, India. I am thankful to my colleagues Mr. Nandkishore Ghodke and Mr. Shailendra Singh Khinchi for making a wonderful work atmosphere at Indore. I would like to thank my dear friends Dr. Rajneesh Atre, Amit Goswami and Sagar Arondekar for all encouragement and confidence throughout.

Scholarship received within the ENS Scholarship program for international students during academic year 2005 -2006 and the financial support through CNRS work contract no. 94/07 Int. 345 during 2007 -2008 is gratefully acknowledged.

There are many more individuals and groups who have, knowingly or unknowingly, contributed in good measure to my life and towards this thesis. To all these unnamed contributors, thanks thank you one and all!

ABSTRACT

The characterization of structural and magnetic properties of soft amorphous and nanocrystalline Fe-Zr-Nb-B based alloy in the form of ribbons and thin films is presented and discussed in this work. Detailed study of amorphous and nanocrystalline phase of $Fe_{84}Nb_{3.5}Zr_{3.5}B_8Cu_1$ ribbons has been carried out using differential scanning calorimetry (DSC) , Thermal gravimetric analysis (TGA), X-ray diffraction (XRD) measurements and Mössbauer spectroscopy. Experimental determination of anisotropy field distribution for nanocrystallline $Fe_{84}Nb_{3.5}Zr_{3.5}B_8Cu_1$ ribbons is also presented and discussed in order to have a better idea of effective anisotropy of the system. Magneto transport properties of ribbons were studied by giant magneto impedance measurements. Also discussed is the possible limitation of applicability of random anisotropy model for optimally crystallized soft magnetic materials by presenting a grain size and volume fraction dependence of coercive field applied for the case of a Fe-Co alloy system. Thin film samples were prepared using ion beam sputtering and RF sputtering method using amorphous $Fe_{84}Nb_{3.5}Zr_{3.5}B_8Cu_1$ ribbons as target material. Complementary information on the structural properties of amorphous and nanocrystalline thin films was obtained using X-ray reflectivity (XRR), grazing incidence X-ray analysis and atomic force microscopy. Magnetic properties of ribbons and thin film samples were studied using standard hysteresis measurements, vibration sample magnetometer and alternating field gradient magnetometer. Ferromagnetic resonance studies done on as deposited thin film samples are also discussed.

Keywords: Soft magnetic Properties, Nanocrystalline materials, Effective anisotropy, Ribbons, Thin films.

RÉSUMÉ

La caractérisation des propriétés structurale et magnétique des alliages Fe-Zr-Nb-B amorphes doux et nanocristallins sous la forme de rubans et de films minces est présentée et discutée dans ce travail. L'étude détaillée des rubans de $Fe_{84}Nb_{3.5}$ $Zr_{3.5}B_8Cu_1$ dans leur phase amorphe et nanocristalline a été faite au moyen de mesures par scan calorimétrique différentiel (Differential Scanning Calorimetry – DSC), analyse thermo-gravimétrique (Thermal Gravimetric Analysis – TGA), diffraction de rayon X (X Ray Diffraction – XRD) et spectroscopie Mössbauer. La détermination expérimentale de la distribution de champ d'anisotropie pour des rubans nanocristallins de $Fe_{84}Nb_{3.5}$ $Zr_{3.5}B_8Cu_1$ est aussi présentée et discutée dans le but d'avoir une meilleure idée de l'anisotropie effective du système. Les propriétés de magnéto transport de ces rubans ont été étudiées en conduisant des mesures de magneto impédance géante. Egalement discutée est la possible limitation de l'applicabilité du modèle d'anisotropie aléatoire des matériaux magnétiques doux de cristallisation optimale par présentation de la dépendance du champ coercitif appliqué en fonction de la taille de grain et de la fraction volumique dans la cas d'un alliage Fe-Co. Des échantillons de films minces ont été préparés en utilisant des méthodes de sputtering par faisceau d'ions et de sputtering par radio fréquences avec des rubans de $Fe_{84}Nb_{3.5}$ $Zr_{3.5}B_8Cu_1$ comme matériau cible. Des informations complémentaires sur les propriétés structurelles des films minces amorphes et nanocristallin ont été obtenues en usant de la réflexivité des rayons X (X ray reflectivity – XRR), analyse par diffraction de rayons X en incidence rasante (Grazing Incidence X rays) et microscope à force atomique (Atomic Force Microscopy – AFM). Les propriétés magnétiques des rubans et films minces étudiés furent caractérisées grâce aux mesures d'hystérésis standard, magnétomètre à échantillon vibrant (Vibrating Sample Magnetometer – VSM) et magnétomètre à gradient de champ alternatif. Les

études de résonance ferromagnétique faites sur des échantillons de films minces déposés tel quel sont aussi discutées. L'interdépendance des propriétés structurales et magnétiques pour à la fois les rubans et les films minces est discutée.

Mots clés : Propriétés magnétiques de matériaux doux, Matériaux nanocristallins, Anisotropie effective, Rubans, Couches minces.

CONTENTS

1. Introduction **1**

1.1 Philosophical background

1.2 Soft magnetic materials

1.3 Magnetic properties of amorphous and nanocrystalline alloys

1.3.1 Basic aspects

1.3.2 Origin of soft magnetic behavior in amorphous and nanocrystalline materials

1.4 Objectives of the work

References

2. Preparation and micro structural investigation of amorphous and nanocrystalline FeZrNbBCu ribbons **28**

2.1 Technique for preparation of amorphous ribbons

2.2 Differential scanning calorimetry

2.2.1 Introduction

2.2.2 Crystallization of amorphous $Fe_{84}Nb_{3.5}Zr_{3.5}B_8Cu_1$ ribbons

2.3 X-ray diffraction measurements

2.3.1 Introduction

2.3.2 Nanocrystallization of amorphous $Fe_{84}Nb_{3.5}Zr_{3.5}B_8Cu_1$ ribbons

2.4 Mössbauer spectroscopy analysis

2.4.1 Introduction

2.4.2 Mössbauer spectra of amorphous and nanocrystalline $Fe_{84}Nb_{3.5}Zr_{3.5}B_8Cu_1$ ribbons

References

3. Preparation and micro structural characterization of FeZrNbBCu thin films **60**

3.1 Preparation of FeZrNbBCu thin films

3.1.1 Introduction

3.1.2 Preparation of thin film samples

3.2 X-ray scattering analysis

3.2.1 Thickness determination using X-ray reflectivity measurements

3.2.2 Grazing incidence XRD measurements

3.3 Atomic force microscopy images

3.3.1 Introduction

3.3.2 AFM images of as-deposited and annealed thin film samples

References

4. Investigation of magnetic properties of amorphous and nanocrystalline FeZrNbBCu ribbons **91**

4.1 Determination of soft magnetic properties

4.1.1 Introduction

4.1.2 Effect of annealing on the soft magnetic properties of $Fe_{84}Nb_{3.5}Zr_{3.5}B_8Cu_1$ ribbons

4.2 Determination of anisotropy field distribution

4.2.1 Experimental method

4.2.2 Results and discussion

4.3 Giant magneto impedance measurements

4.3.1 Introduction

4.3.2 Effect of annealing on magneto transport properties of $Fe_{84}Nb_{3.5}Zr_{3.5}B_8Cu_1$ ribbons

4.4 Departure from random anisotropy mechanism

4.4.1 Introduction

4.4.2 Results and discussion

References

5. Investigation of magnetic properties of FeZrNbBCu thin films **129**

5.1 Introduction

5.2 Magnetic properties of ion beam sputtered FeZrNbBCu thin films

5.2.1 Effect of annealing treatment on magnetic properties

5.2.2 Ferromagnetic resonance measurements

5.3 Magnetic properties of RF sputtered FeZrNbBCu thin films

References

Conclusions **161**

Future work **164**

Appendices **166**

List of publications **178**

CHAPTER 1

Introduction

This chapter presents the philosophical background of the research that has been carried out in the field of magnetism. A variety of soft magnetic materials are summarized in order to present relative alloy systems. Some basic concepts related to the magnetic properties of soft magnetic nanocrystalline materials is also discussed in order to understand the mechanisms and various energies that play important role in determining the soft magnetic behavior. Motivation and objectives of the present work carried out by us is briefly introduced.

- ***Philosophical background***
- ***Soft magnetic materials***
- ***Magnetic properties of amorphous and nanocrystalline alloys***
- ***Objectives of the work***
- ***References***

1.1 Philosophical background

The incessant changes which experience brings before us, taken in conjunction with the thought of unity in productive force of nature, leads to the all-important conception of the duality, the polar opposition through which nature expresses itself in its varied products. The dynamical series of stages in nature, the forms in which the ideal structure of nature is realized, are matter, as the equilibrium of the fundamental expansive and contractive forces; light, with its subordinate processes--magnetism, electricity, and chemical action. The fact that certain bodies, after being rubbed, appear to attract other bodies, was known to the ancients. In modern time's great varieties of other phenomena has been observed and have been found to be related to these phenomena of attraction. They have been classed under the name of electric phenomena and Amber was the substance in which those were first described. Other bodies particularly loadstone and piece of iron which have been subjected to certain conditions have also been long known to exhibit phenomena of action at a distance and these were classed under magnetic phenomena as the loadstone being found in Thessalian magnesia. These two classes of phenomena have since been found to be closely related to each other and the relations between the various phenomena of both classes so far as they are known, constitute the science of electromagnetism which is the basis of the successful discovery of electricity and the implementation of the devices that uses electricity. Just as nature exhibits to us the series of dynamical stages of evolutionary processes by which spirit struggles towards consciousness of itself, so the world of intelligence and practice, the world of mind, exhibits the series of stages through which a civilization with inevitable oppositions and reconciliations, develops in its ideal form. The development of civilization has been dependent upon the ability of humans to work, or to

produce work, far beyond the physical limitations of their own muscles. The Natural laws of thermodynamics say that “energy can neither be created nor can be destroyed” and “it can never be completely and continuously converted into work” (though it can be transformed from one form into another). These Natural laws have not yet confined the technological pursuits of humans and the ability to find and expand resources for individual power and useful energy. Electricity is certainly energy beyond our muscles; it is highly ordered and can be converted efficiently into other energy forms. It is usually generated as it is needed because it cannot be stored conveniently. And despite a great variety of energy conversion possibilities, practically all electrical power at present is still generated by devices employing magnetic fields. Understanding magnetism and tailoring magnetic materials, therefore contribute fundamentally to the progress of science, technology and humankind. Enabled by the significant content of ferromagnetic elements, mainly Fe, in the earth’s crust, spontaneous magnetism and magnetic phenomena were discovered many centuries ago by ancient cultures in all continents, including Indian, Persian, Mesoamerican, Greek and Chinese. However, even today magnetism is, astonishingly, continuing to surprise us with the observation of new phenomena and the discovery of novel advance materials. Magnetic materials are broadly classified into two main groups with either hard or soft magnetic characteristics. Soft magnetic materials can be magnetized by relatively low-strength magnetic fields, and when the applied field is removed, they return to a state of relatively low residual magnetism. Soft magnetic materials typically exhibit coercivity values of the order of 400 A m^{-1} (5 Oe) to as low as 0.16 A m^{-1} (0.002 Oe). Soft magnetic behavior is important in any application involving a change in magnetic induction. Hard magnetic materials retain a large amount of residual magnetism after

exposure to a magnetic field. These materials typically have coercivities, of the order 10 kA/m (125 Oe) to 2 MA/m (12 kOe). The materials at the high coercivity end of this range are known as permanent magnets. These materials are used principally to supply a magnetic field. The magnetic properties of materials can be divided into two general categories: those that are structure sensitive and those that are structure insensitive. Structure insensitive refers to properties not markedly affected by changes in materials processing (heat treatment or mechanical deformation) or by small changes in composition, including small amounts of certain impurities. Structure-insensitive properties include the saturation magnetization and resistivity. These properties are largely dependent on the composition of the particular alloy and are not changed substantially in the process of manufacturing a component from the alloy. Structure-sensitive properties are those that are drastically affected by impurities. Small amounts of elements such as carbon, oxygen, nitrogen, and sulphur are commonly found in small quantities in magnetic materials. These elements tend to locate at interstitial sites in the crystalline lattice and consequently the lattice can be severely strained. As a result small concentrations of these elements can have large effects on some of the magnetic properties of the materials. Permeability, coercivity, hysteresis losses, remanence, and magnetic stability are all considered to be structure sensitive. The structure sensitive properties are controlled through processing of the material including mechanical and thermal treatments. The progress by soul meaning has been the ability to systematically evaluate science and society with hypotheses, experimentations, data collection, interpretation and the assessment of results. Science can be pursuit of truth and revelation then, and engineering the use of these truths revealed to advance the well being of humankind. In materials science and engineering, this scientific method is combined

with the philosophy that there are four ideas that motivates research in the field: Structure, processing, properties and performance. All research and development in the field of magnetic materials is motivated by the aim of improving the materials useful to society and this development proceeds as the understanding of structure, processing, properties and performance improves. Magnetism has played a major role in various scientific revolutions, transcending its pure scientific significance for society. For example the introduction of relatively soft magnetic steels as magnetic cores in transformers around one hundred years ago enabled more efficient distribution of electrical energy from its source to factories, public spaces and private homes. More recently magnetic recording has been contributing to significantly improve the way of life. Nowadays application ranges from large variety of hard magnets widely employed in everyday life to sophisticated magnetic sensors controlling artificial satellites and the mapping of tiny magnetic fields in human brain. The present trends in scientific and technological research in magnetism are related to recent advances in nanosciences and nanotechnologies. With the optimization of experimental techniques new phenomena have been demonstrated which have stimulated the emergence of new research areas. It should be emphasized that progress to a large extent is being made possible by current development of techniques for the fabrication and processing of materials with controlled characteristics on the nanoscale which facilitates the preparation of novel materials with tailored nanometric dimensions, 0D (nanoparticles and nanodots), 1D (nanowires and nanotubes) or 2D (hetrostructures, thin films and multi layers) and characteristic bulk nanocomposites, nanocrystalline alloys, surface coatings etc.

1.2 Soft magnetic materials

Soft magnetic materials can be defined in a very simple yet in a categorical way as, "The material is called as a soft magnetic material when the magnetization processes i.e. domain wall motion and domain magnetization rotation can occur in weak fields, ($< 10^3$ A/m)" [1]. Soft magnetic materials are generally used in applications where high permeability is required. In soft magnetic materials the flux density is dominated by the contribution of magnetization. Broadly the soft magnetic materials are classified in following categories.

(a) *Fe-Si steels:* The pure iron is considered as soft magnetic material with very high saturation magnetization (2.2 Tesla) and a relatively low magnetocrystalline anisotropy value ($48kJ/m^3$). Usually impurities like carbon, nitrogen and oxygen are present in common grades of iron and it is possible to remove these impurities by employing hydrogen annealing which remarkably improves the permeability of iron. On the other hand introduction of silicon into iron results in great decrease in the core losses. Although silicon reduces the saturation magnetization value but it has added advantage as it increases the electrical resistivity and mechanical strength of alloy but more than 4% Si starts to reduce the ductility of the Fe-Si steel.

(b) Fe-Ni alloys: Magnetic iron nickel alloys are generally termed as Permalloys.

Originally permalloy was a typical trademark composition for certain Fe-Ni alloy but now it is widely known as a family constituting of $Fe\text{-}Ni_3$ FCC compound with the percent of nickel varying from 35 to 100. It is important family of alloy as transverse anisotropy can be induced in order to compensate the crystalline anisotropy. Nevertheless this family of alloy has four major categories from view point of technical importance.

- Supermalloy is alloy with 78% nickel which exhibits almost negligible magnetostriction and anisotropy. It also offers high initial permeability and hence is quite favuorite candidate in differential transformer applications.
- 65% nickel permalloy which exhibits very low anisotropy and it is possible to tailor the hysteresis properties suitably by inducing anisotropy by field annealing etc.
- 50% nickel permalloy offers relatively higher saturation magnetization (1.6 Tesla) and is also strongly responsive to the field annealing.
- 36% nickel pemalloy is quite useful for metrological applications.

(c) Fe-Co alloys: The equiatomic BCC Fe-Co alloys called as Permendur exhibits a very high saturation value (2.4 Tesla) and relatively low magnetic anisotropy value (~ -10kJ/m^3). Anisotropy is nearly zero for the ordered state. For this family of alloy anisotropy, magnetostriction and mechanical properties depend strongly upon the annealing and cooling rates. Although commercially the cobalt is relatively expensive still iron cobalt alloys of Permendur family are used in applications where the highest flux density, relatively lower weight is preferable over the AC loss and cost. For example these alloys are widely used in transformers and generators of aircraft power systems.

(d) Soft spinel ferrites: The soft ferrites offer some excellent magnetic properties. The resistivity of these ferrites is quite higher than conventional metallic soft magnetic materials which make ferrites an industrial favourite specifically for high frequency applications. Ferrites also offer high corrosion resistance. However low saturation induction, low curie temperature and poor mechanical properties are some of the

disadvantages that are associated. The ferrites are based on the spinel structure of Fe_3O_4. The two common categories of ferrites are Mn-Zn and Ni-Zn ferrites.

(e) Amorphous alloys: The first metallic glass was made by Kramer in 1934. This was based on the chemical vapour deposition [2]. In 1946 noncrystalline deposits were observed on Ni-P electrodeposits [3]. Duwez developed a method for the preparation of amorphous metals by quenching the melt directly [4]. Later Salli and co workers invented a splat cooling apparatus in which the molten metal alloy drop was rapidly flattened on a cold surface [5]. This idea was later developed as an apparatus that was capable of producing long length amorphous ribbons on a commercial scale [6]. For years it was believed that amorphous state could not exhibit ferromagnetic properties because of lack of long range ordering till Gubanov [7] predicted that short range order played an important role in ferromagnetism and hence glassy materials can be ferromagnetic. The amorphous or glassy state can be considered as an extended liquid state displaying some aspects of solid state also. More generally it can be said that all alloys can exist in amorphous state if the cooling rate that is employed is fast enough to freeze the topologically disordered substance. The glass transition temperature is a characteristic parameter above which the glassy material is in so called super cooled liquid state where it behaves like a very viscous liquid up to crystallization temperature. At glass transition temperature (T_g) the temperature dependence of enthalpy starts to increase discontinuously as shown in figure 1.2.1. The most important parameter in the production of amorphous alloys is the glass forming ability which gives information about the possibility of acquiring amorphous state. The amorphous alloys are generally categorized on the basis of their physical extent.

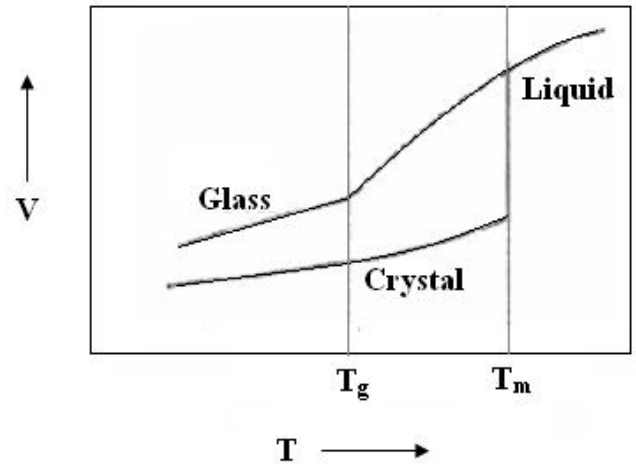

Figure 1.2.1: Temperature dependence of enthalpy in glassy metals.

This depends mostly upon the glass forming ability of a given composition. On the basis of this characteristic, amorphous alloys can be divided in following broad families.

- **Bulk amorphous alloys:** It was considered that the multi component alloy system with more than 3 elements with significant difference in atomic size ratio is suitable for producing bulk amorphous alloy. It is preferable that some of the constituent elements have negative heat of mixing with the ferromagnetic metal component of the composition. Bulk amorphous alloys can be produced in the form of amorphous ribbons by melt spinning with a well controlled thickness of 25- 200 μm. In some cases where super cooled liquid region is large enough the possible method of producing bulk metallic glasses is copper mold casting and thickness ranging upto 6mm can be reached without any sign of crystallization. For ferromagnetic ribbons the super cooled liquid region is much smaller than the bulk alloys. Moreover the magnetic properties are having more priority over the glass forming ability in terms of design because very high quenching rates can be achieved by melt spinning

method so the compositions are optimized for lower residual stresses after quenching and from view point of possible production in air. Three main families of amorphous ribbons produced commercially are mainly iron based, cobalt based and Fe-Ni based with some glass formers like boron, silicon carbon etc. as additives.

- **Glass covered amorphous micro wires:** The glass coated amorphous micro wires are produced by first melting the alloy in a glass nozzle at a high temperature so that alloy melts together with the nozzle. Then the filament is stretched under water jet to produce cylindrical wires of typical diameter of 3-30 μm. The glass coating around the wire is about 1-15 μm thick. This process produces wires in a large range of compositions which were otherwise not possible using conventional method of producing amorphous alloys.

- **Thin films:** Another important group consists of thin magnetic films. The fundamental properties are linked to the local environment that can be different at the surface than in the bulk. These films are produced by sputtering method which will be describe in much details in chapter 3 of this work. Unlike most of vapour deposition techniques sputtering does not involve any melting of material which permits deposition of many metastable amorphous materials, such as oxides, that cannot be produced by melt spinning.

(f) Nanocrystalline magnetic alloys: Until late eighties a large variation in the compositions, preparation methods and annealing treatments were developed in order to

improve the soft magnetic properties. Due to vary fast casting process the amorphous structure is always far from the equilibrium state. This amorphous or frozen glass state always tends to reach to a more stable state by say for example diffusion of atoms. The attempt to acquire a partially crystallized structure was motivated by the requirement of stabilizing the magnetic properties for elevated temperatures. Another consideration was to minimize the magnetostriction by creating a two phase system where the magnetostriction values corresponding to two phase cancel out each other resulting into an almost zero magnetostrictive state. Preliminary efforts in order to obtain partially crystallized structure were not encouraging until for the very first time Yoshizawa and co workers reported the soft magnetic material in 1988 [8] at the Hitachi Metals laboratory. This discovery introduced a new family of soft magnetic materials termed as FINEMET. This material was derived from the amorphous Fe-Si-B alloy and the composition $Fe_{73.5}Si_{13.5}Nb_3B_9Cu_1$ is patented worldwide as FINEMET^{TM}. This alloy when was annealed at 540^{o}C for 1 hour exhibited a homogeneous grain structure comprising of 12nm nanograins. This offers high saturation induction (1.24 Tesla), high permeability (10^5@ 1kHz) and low coercivity (0.5 A/m). In 1990 another type of Fe-Zr-B based nanocrystalline alloy was reported by Suzuki and co-workers termed as NANOPERM [9]. This system of alloy yields higher saturation induction (1.5-1.7 Tesla) as compared to the FINEMET alloys. The nanogranular structure consists of α- Fe nanocrystallites of average size 10nm.Most recently a nanocrystalline alloy named HITPERM with high cobalt content has been derived from Nanoperm with the aim of improving high temperature magnetic properties [10].

1.3 Magnetic properties of amorphous and nanocrystalline alloys

1.3.1 Basic aspects

Applications that require small hysteresis losses per cycle are categorized as soft magnetic materials that have following attributes.

- High Permeability: This is the parameter that describes the magnetic flux density produced by a given applied magnetic field. When a material has high permeability very large changes in magnetic flux density can be produced by applying very small magnetic fields.
- Low hysteresis loss: This represents the energy consumed in cycling a magnetic material between peak values (H_{max} and - H_{max}) of applied magnetic field. It is usually denoted by the area of the hysteresis cycle and for AC applications power loss is determined by multiplying the frequency of applied field to the hysteresis loss per cycle.
- Large saturation and remnant magnetization.
- Low eddy current losses
- High Curie temperature: suitable for applications employing high temperature.

The shape of the hysteresis curve is basically determined by minimization of the magnetic free energy of the material. Magnetic free energy of the ferromagnetic material consists of following energy terms.

Zeeman energy (Field energy): This energy density term describes the relation between magnetization of magnetic material and the applied external magnetic field.

This energy term is minimized when the magnetization is parallel to the external applied field.

Demagnetization energy: The free poles created on the ends of a magnetic material gives rise to an effective field given as $H_{eff} = N H_{ext}$ where N is demagnetizing factor whose value depends upon the position and orientation of magnetization inside the sample.

Exchange energy: This energy term is the real origin of the ordered spin structure. It is well known from Pauli's exclusion principle that no two fermions can have same quantum mechanical state. This is the reason why two electrons with anti parallel spins try to approach each other. The electrostatic Coulomb energy is smaller for parallel spin configuration rather than the anti parallel spin state. The difference in the energy of above two states is basically called exchange energy. It should be noted that the exchange interaction is an electrostatic phenomenon and it is not an interaction between magnetic moments. As a result of exchange interaction declination of a local moment induces the alteration in the direction of other spin orientations but this effect decays exponentially with distance. So the characteristic distance over which the local moment declines by a factor of 1/e is called exchange length.

Magnetic anisotropy energy: If the direction dependence of any physical property is observed then it is considered that the property exhibits anisotropy. In magnetic material if magnetization orientation is along some preferred direction then the material is said to posses magnetic anisotropy. In such case any parameter governing the magnetization process will have strong direction dependence. The magnetic anisotropy energy term thus describes the angular dependence of the magnetic energy, i.e. its dependence on angles between the magnetization and the easy axis of magnetization. The magnetic anisotropy

represents a barrier in switching of magnetization. For amorphous and crystalline soft magnetic materials it s required that the anisotropy should be minimized. One way of doing this can be seen as developing random anisotropy on a nanoscale where averaging over exchange length can give rise to fair reduction of anisotropy. This mechanism involving the magnetocrystalline anisotropy along with some other types of anisotropies and their effect on the soft magnetic properties will be described in detail later in this section itself.

1.3.2 Origin of soft magnetic behavior in amorphous and nanocrystalline materials

Origin of soft magnetic behavior in amorphous and nanocrystalline materials can be understood in terms of the magnetic interactions between various magnetic entities (objects) over various characteristic length scales. For instance in case of amorphous magnetic materials these magnetic entities are atomic dipoles whereas in case of nanocrystalline material nanocrystallites precipitated as result of divitrification of amorphous precursor are the objects. The interaction among these objects is effective over certain length scales which are determined predominantly by the structural properties. Although the structure of the amorphous alloys has been referred as random dense packed but the atoms of a metallic glass are not arranged as randomly as in a gas for example. The magnetic interactions between atomic dipoles in metallic glasses extend over approximately two orders of magnitude greater than the length scale of short range order. The disordered structure of amorphous materials gives rise to the randomness in the interaction of these magnetic dipoles. This randomness in interaction can be of two types. First is the random isotropic exchange and second is the random anisotropy. Random isotropic exchange does not considerably affect the magnetic behavior whereas the random anisotropy strongly

influences the magnetic properties by breaking the rotational symmetry of the associated interaction energy. The magnetic moments are strongly affected by the crystal field which originates in the asymmetry of the local environment giving rise to strong local random anisotropies. In other words we may say that in case of amorphous alloys the magnetic anisotropy that arises from long range crystallinity is absent and magnetocrystalline anisotropy is depicted by local fields. Orientation and strength of local anisotropy in amorphous materials varies with position and hence termed as random anisotropy. The effect of these random anisotropies does not cancel out just by the virtue of the fact that these are random in amorphous materials. Rather a balance between the anisotropic and exchange forces determines the magnetic behavior by controlling the various length scales associated with magnetic interaction. The randomness in the magnetic interactions leads to the magnetization fluctuations over regions with random anisotropies. The length scale determined by the balance between the anisotropy and exchange interaction is called ferromagnetic exchange length which scales similar to domain wall width. The exchange length is given by:

$$L_{ex} = \varphi \, (A / K_1)^{1/2}$$

where A is exchange constant and φ depends upon the rotation of spins over this exchange length and K_1 is the anisotropy constant. It should be noted that exchange constant A is described by the formula:

$$A = (M_s \, D_{sp}) / 2 \, g \, \mu_B$$

Where D_{sp} is the spin wave stiffness constant, g is gyro-magnetic ratio and μ_B is Bohr magneton. Thus a volume defined by this exchange length is termed as exchange volume. In the region defined by exchange volume there will always be some easiest preferred

direction of magnetization determined by the statistical fluctuations in a way that the random anisotropies add up. Following the random walk consideration in which the amplitude of the mean fluctuations varies as inverse square root of number of independent contributions, the averaging of random anisotropies takes place according to following:

$$K_{eff} = K_1 / (N)^{1/2}$$

In case of nanocrystalline magnetic materials N is identified with number of nanocrystallites present within the exchange volume. Figure 1.3.1 shows a schematic of the random anisotropy mechanism proposed by Herzer for nanocrystalline magnetic alloys [11-14]. It represents an assembly of exchange coupled nanograins of average size D, and the volume fraction of crystalline phase is V_x with randomly oriented magnetocrystalline anisotropies. The effective anisotropy results from the averaging of anisotropy constant over the nanocrysatllites present within the correlation volume defined by the exchange length.

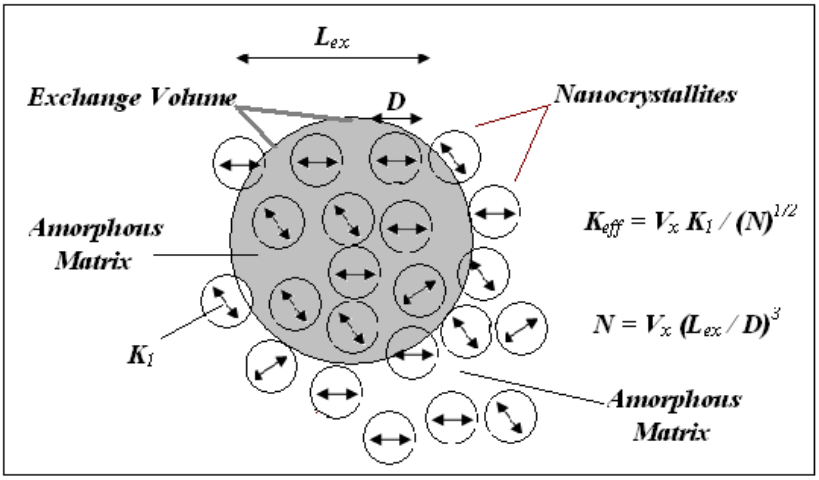

Figure 1.3.1: Schematic representation of random anisotropy model for nanograins embedded in soft magnetic matrix.

In figure 1.3.1 the shaded area indicates the exchange volume determined by the ferromagnetic correlation length whereas the double headed arrows represents randomly fluctuating anisotropy axis. Considering the statistical fluctuations the effective anisotropy constant is represented by: $K_{eff} = V_x K_1 / (N)^{1/2}$ where N is the number of exchange coupled nanograins given by: $N = V_x (L_{ex} / D)^3$. Thus effective anisotropy energy density for a two phase system in which nanograins are embedded in an ideally soft magnetic amorphous matrix is given by:

$$K_{eff} = V_x {}^2K_1 {}^4 D^6 / (A)^3$$

where A is exchange stiffness constant.

Coercivity for the systems where magnetocrystalline anisotropy dominates the magnetization behavior is given by:

$$H_c = p_c K_{eff} / J_s \quad \text{Or} \quad H_c = p_c [V_x {}^2K_1 {}^4 D^6] / (A^3 . J_s)$$

Above expression represents the most significant feature predicted by random anisotropy model proposed by Herzer [13, 14]. Effective anisotropy and hence the coercivity varies strongly with sixth power of average grain size. The magnetic properties of NANOPERM^{TM} ($Fe_{86}Zr_7B_6Cu_1$) has been studied and compared to that of FINEMET ($Fe_{73.5}Si_{13.5}Nb_3B_9Cu_1$) alloys [15]. Both materials precipitate BCC Fe nanocrystallites but 20 at. % of silicon in FINEMET reduces both magnetic anisotropy and saturation magnetization. The saturation magnetostriction values were observed to be shifted towards more negative values. It has been predicted on the basis of random anisotropy model (RAM approach) described above that the good soft magnetic properties of the partially crystallized amorphous matrix emerge from the exchange averaging of the magnetocrystalline anisotropy of the nanocrystallites and from the averaging of the

effective magnetostriction as a weighted sum of positive (amorphous matrix) and negative (nanograins) contributions. The difference of saturation magnetization between the amorphous matrix and nanocrystallites also affects the soft magnetic properties. A small difference in saturation magnetization avoids the formation of strong free poles and the phase boundary which would otherwise impede the domain wall motion and thereby decrease in initial permeability [13].The random anisotropy model was originally addressed for amorphous alloys but as described above the arguments of random anisotropy mechanism were successfully applied in the case of optimally annealed alloys system characterized by two phase microstructure [14, 16]. Figure 1.3.2 represents the variation of coercivity with average grain size for Fe-based nanocrystalline along with the data for amorphous and conventional polycrystalline soft magnetic materials [13]. Nanocrystalline materials basically fill in the gap between amorphous and conventional polycrystalline alloys. Although deviations from the grain size dependence has been observed which will be discussed in next section that forms the basis for the objectives proposed for the work presented in this thesis.

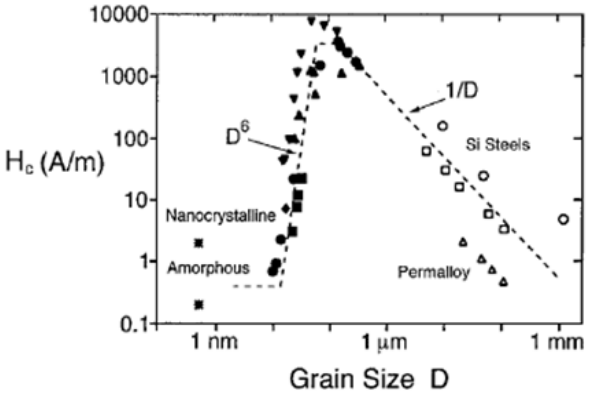

Figure 1.3.2: Coercivity variation with average grain size for various soft magnetic alloys [13].

1.4 Objectives of the work

Gradually devitrified nanocrystalline soft magnetic materials have originated from the research aimed at the improvement of the soft magnetic properties of amorphous alloys. Earlier it was believed that the magnetic softness of an amorphous alloy deteriorates with increasing the annealing temperature far beyond the crystallization temperature. Later on, as described in earlier section also that it was realized that the soft magnetic behavior of amorphous alloys can be enhanced significantly by partial crystallization, when excellent soft magnetic properties were first reported for nanocrystalline $Fe_{73.5}Si_{13.5}B_9Cu_1Nb_3$ alloy (also known as FINEMET alloy) produced by suitable annealing treatments [8]. Today there are number of nanocrystalline soft magnetic materials available, offering unique properties important for applications, e.g. - high saturation induction, low core losses and high permeability, required in the field of electronics, power electronics, magnetic field sensors etc. The nanocrystalline FeCuNbSiB alloys are currently available for various magnetic components such as common-mode choke coils for noise filters, power transformers for inverters, magnetic switches for accelerators or excimer lasers, and so on. Studies have also revealed that partial substitution of Fe by Co in classical Finemet alloys show improved magnetic properties suitable for such electromagnetic applications employing high frequency and elevated temperatures [17-20]. Apart from the promising industrial applications these nanocrystalline soft magnetic materials are of immense interest from view point of fundamental research as these materials offer unique opportunity to understand the physics of magnetization processes which are the cause of the excellent soft magnetic behaviour. These nanocrystalline materials are made up of small size crystallites (~ 8-15 nm) dispersed in an amorphous matrix. The key requirement for superior soft

magnetic behaviour generally is a low or vanishing anisotropy. Degree to which the anisotropy is finally averaged out has been successfully addressed in terms of random anisotropy model proposed by Herzer (see section 1.3.2), originally developed by Alben, Becker and Chi in order to explain the soft magnetic properties of amorphous ferromagnets [14, 16]. Devitrification process (nanograins dispersed in residual amorphous matrix) leads to a distribution of magnetic anisotropy axis randomly varying, over the length scale of average diameter (~ nm) of nanograins. The soft magnetic properties basically arise from the delocalization of these random anisotropies, which is a consequence of the exchange interactions among the crystallites. This becomes effective for the grain sizes smaller than the ferromagnetic exchange length. Thus the effective anisotropy contribution of the small randomly oriented nanograins embedded in amorphous matrix is essentially reduced and leads to an extraordinary sixth power dependence of coercivity on the average grain size [11-14]. However the experimental variation of grain size cannot be performed in a completely straightforward way, as it inevitably requires changes of alloy composition and annealing conditions. This changes the composition of crystallites and the residual amorphous phase that produces a significant change in the anisotropy and hence in the exchange interactions among the grains. Effect of thickness, preparation conditions and post preparation treatments are known to affect magnetic properties. Studies have also been done in order to investigate the effect of thickness and preparation conditions of the nanocrystalline materials (both in ribbon shape and thin film shape) on their soft magnetic properties [21-23]. However systematic studies on the comparison of the influence of structural properties on the soft magnetic properties for the same composition in the form of a ribbon (thickness~ μm) and thin film (thickness ~ nm), is lacking. Such studies will

enrich the understanding of delocalization process that turns out to depend considerably on the topology of the system, which basically affects the number of exchange-coupled particles. Therefore the study of the soft magnetic nanocrystalline system in different possible topologies can be of great importance, which would provide information on the influence of the structure on delocalization.

The development of the nanocrystalline Fe-Si-B-Cu-Nb alloy [8] was soon followed by many studies on the Fe-metal based nanocrystalline alloys e.g. $Fe_{91}Zr_7B_2$, exhibiting excellent soft magnetic properties [24-29]. Some of the most important and widely studied nanocrystalline alloys offering exceptional soft magnetic properties are: FINEMET alloys (Fe-Si-B-Cu-Nb), NANOPERM alloys (Fe-M-B-Cu), HITPERM alloys (Fe-Co)-M-B-Cu), where M = Zr, Nb, Hf. FINEMET^{TM} has been commercialized by Hitachi metals and is also being sold (under licensed agreement) by Vacuumschmelze GMBH. NANOPERM is a trademark of Alps electric but is not currently being produced commercially. The potentially high operating temperatures desirable in many evolving power electronic and motor applications have led to the development of nanocrystalline Fe-Co based alloys called HITPERM.

The unique microstructure in the nanocrystalline soft magnetic materials has stimulated intensive investigations on the decomposition behaviour in the amorphous precursor, which showed that the nanostructural evolution is due to primary crystallization of the precursor amorphous phase and the resultant nanoscale structure consists of the crystalline phase precipitates and the residual amorphous matrix [8, 11-14]. The origin of soft magnetic properties was explained on the basis of random anisotropy model, which was primarily proposed for almost fully crystallized system. This means that the sixth power dependence

of coercivity on the average grain size was addressed for a single-phase system consisting of randomly oriented grains with sizes considerably less than the ferromagnetic exchange length. The phenomenological arguments of random anisotropy model become less adequate when it comes to the consideration of two-phase character (crystalline and the amorphous matrix) of the real systems. Later on some modifications were proposed by taking into account the two phase character of the systems which raised further questions regarding the relationship between the structural parameters and magnetic behaviour, as smaller exponents for the grain size power dependence, were reported for some alloy systems [30-35]. Attempts have been made to explain the inadequacy of the original arguments proposed by Herzer for the case of two-phase systems. Random anisotropy mechanism, at present, seems to be one of the widely accepted mechanisms for the delocalization of the anisotropy in nanocrystalline soft magnetic materials though the possibility of other mechanisms responsible for the delocalization cannot be denied. There exists no straightforward experimental method to estimate the averaged anisotropy that poses hindrance in the path leading to a clear-cut understanding of the interplay between structural changes and the delocalization of the anisotropy. Studies were done in order to account for the changes in anisotropy with temperature via observing the changes in the coercivity with temperature as average anisotropy is theoretically related to the coercivity though the relationship among two is not analytical and hence it is still to be explored as to what is the exact interdependence of the average anisotropy and the structural parameters (e. g. – average grain diameter, volume fraction of the nanocrystalline phase) which eventually affect the delocalization of anisotropy and hence the soft magnetic behavior of nanocrystalline alloys [36-38]. Dimensionality of the system plays an important role in

determining the delocalization process which results from the competition between the exchange energy and anisotropy energy that basically decides the variation in the number of particles lying within the length scale over which the exchange interactions are dominant. Influence of thickness and preparation conditions of the materials in both ribbon shape and thin films of nanocrystalline materials on their soft magnetic properties is reported [21-23]. Recently random anisotropy model has been proposed for the system of thin films. The coercive field has been reported to follow inverse thickness dependence as shown in figure 1.4.1 [39]. Considering the thickness of the thin film to be *t*, the effective anisotropy for thin film can be written as

$$K_{eff} = V_x K_1 / (N)^{1/2}$$

Where number of nanograins present in exchange coupled volume is given as

$$N = V_x (L_{ex}^2 \, t / D^3)$$

where t is the thickness of thin film.

Thus effective anisotropy for the case of thin films is given by:

$$K_{eff} = (V_x K_1^2 D^3) / (A \, t)$$

It should also be noted that effective anisotropy is inversely proportional to the thickness of the thin film and varies as third power of grain size. Thus coercive field for the system of thin films scales like:

$$H_C = (V_x K_1^2 D^3) / (A \, t \, J_s)$$

Nevertheless studies on the influence of structural properties on the soft magnetic properties for the same composition in the form of a ribbon (thickness~ μm) and thin film (thickness ~ nm), would be enriching.

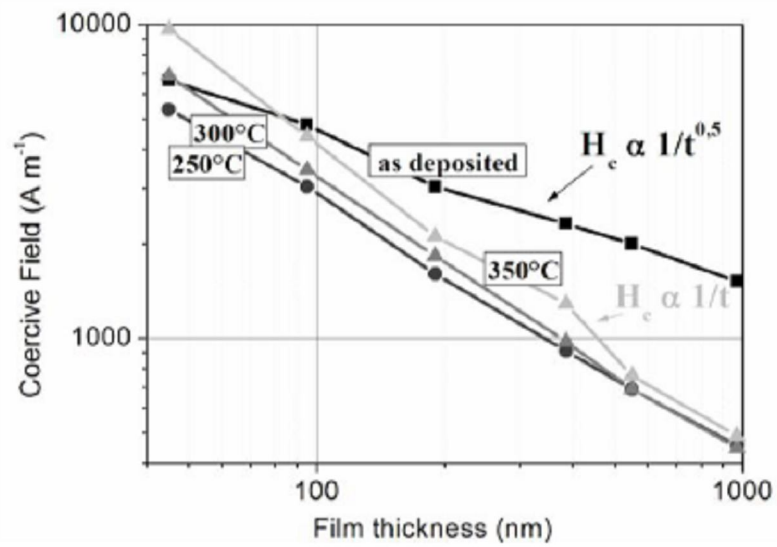

Figure 1.4.1: Coercive field as a function of thickness for FINEMET films [39].

Therefore the study of the soft magnetic nanocrystalline system in possible different dimensionalities will be of great significance.

This thesis will present experimental data on the structural and magnetic properties of $Fe_{84}Nb_{3.5}Zr_{3.5}B_8Cu_1$ alloy in the form of ribbons being nanocrystallized by suitable annealing treatment [40, 41]. Structural and magnetic investigations done on the thin films of various thicknesses prepared using $Fe_{84}Nb_{3.5}Zr_{3.5}B_8Cu_1$amorphous ribbons are also reported. Presented studies are efforts in order to address the relationship among the structural parameters and magnetic properties for the better understanding of the delocalization of anisotropy being originated from the micro-structural evolution.

References:

[1] R. C. O'Handley, Modern Magnetic Materials, New York John Wiley and Sons (2000).

[2] J. Kramer, Ann. Phys. 19 (1934) 37.

[3] A. B. Rener, G. Riddell, J. Res. Nat. Bur. Stand (1946).

[4] P. Duwez, S. C. H. Lin, J. Appl. Phys. 38 (1967) 4096.

[5] I. S. Miroshninenko and I. V. Salli, Ind. Lab. 25 (1959) 1463.

[6] R. Pond, R. Maddin, TMS-AIME 245 (1969) 2475.

[7] A. I. Gunbanov, Physica 2 (1960) 502.

[8] Y. Yoshizawa, S. Oguma and K. Yamauchi, J. Appl. Phys. 64 (1988) 6044.

[9] K. Suzuki, N. Kataoka, A. Inoue, A. Makino, T. Masumoto, Mater. Trans. JIM 31 (1990) 743.

[10] M. A. Willard, D. E. Laughlin, M. E. McHenry, D. Thoma, K. Sickafus, J. Gross, V. G. Harris, J. Appl. Phys. 84 (1998) 6773.

[11] G. Herzer, IEEE Trans. Mag. 25(1989) 3327.

[12] G. Herzer, IEEE Trans. Mag. 26 (1990) 1397.

[13] G. Herzer, Scripta Metallurgica et Materialia vol.33 (1995) 1741.

[14] G. Herzer, J. Magn. Magn. Mater 294 (2005) 99.

[15] L. K. Varga, L. K. Novak, F. Mazaleyrat, J. Magn. Magn. Mater 210 (2000) L25.

[16] R. Alben, J. J. Becker and M. C. Chi, J. Appl. Phys. 49 (1978) 1653.

[17] C. Gomez-Polo, P. Marin, L. Pascual, A. Hernando, M. Vázquez, Phys. Rev. B65 (2001) 24433.

[18] Zs. Gercsi, S. N. Kane, J. M. Greneche, L. K. Varga and F. Mazaleyrat, Phys. Stat. Sol. (C) 1 (2004) 3607.

[19] A. D. Bensalah , F. Alves, R. Barrue, F. Simon, S.N. Kane, Sensors and Actuators A 129 (2006) 142–145.

[20] F. Alves , F. Simon, S. N. Kane, F. Mazaleyrat, T. Waeckerlé, T. Save and A. Gupta J. Magn. Magn. Mater. 294 (2005) e141.

[21] S. N. Kane, A. Gupta , T. Kulik and L. Kraus J. Magn. Magn. Mater 254-255 (2003) 498.

[22] P. Sharma, A. Gupta, Nuclear Instruments and Methods B vol.244 (2006) 105.

[23] P. Sharma, A. Gupta, J. Magn. Magn. Mater 208 (2005) 347.

[24] K.Suzuki, M. Kikuchi, A. Makino, A.Inoue, T. Masumoto, Materials Trans. JIM, 32 (1991) 961.

[25] K.Suzuki, A. Makino, N. Kataoka, A.Inoue, T. Masumoto, Materials Trans. JIM, 32 (1991) 93.

[26] K.Suzuki, A. Makino, A.Inoue and T. Masumoto, J.Appl.Phys. 74 (1993) 3316.

[27] A.Makino, A.Inoue and T. Masumoto, Nanostructured Materials vol.6 (1995) 985.

[28] K.Suzuki, A. Makino, An-Pang Tsai, A.Inoue and T. Masumoto,Materials Sciences & Engineering A179/A180 (1994) 501.

[29] A.Makino, A.Inoue and T. Masumoto, Material Trans. JIM, 36 (1995) 924.

[30] A. Hernando, M. Vàzquez, T. Kulik, C. Prados, Phy.Rev.B 51 (1995) 3581.

[31] A. Hernando, I. Navarro P. Gorria, Phy.Rev.B 51 (1995) 3281.

[32] K. Suzuki, J. M. Cadogon, Phy.Rev.B 58 (1998) 2730.

[33] J. Arcas, A. Hernando, J. M. Barandiaran, C. Prados, M. Vàzquez, P. Marin, A. Neuweiler, Phy. Rev. B 58 (1998) 5193.

[34] K.Suzuki, A. Makino, A.Inoue and T. Masumoto, J.Appl.Phys. 70 (1991) 6232.

[35] K. Suzuki, G. Herzer, J. M. Cadogon, . J. Magn. Magn. Mater 177-181 (1998) 949.

[36] Xiang-Yuan Xiong and Kai-Yuan Ho, J.Appl. Phys 77 (1995) 2094.

[37] V. Franco, C. F. Conde, A. Conde, J. Magn. Magn. Mater 185 (1998) 353.

[38] V. Franco, C. F. Conde, A. Conde, J.Appl.Phys 84 (1998) 5108.

[39] Johan Moulin, F. Mazaleyrat, A. Mendez, E. D. Gergam, Presented JEMS'08 Dublin 14-19 September 2008.

[40] S. S. Modak, N. Ghodke, B. Rathore, F. Mazaleyrat, M. LoBue, L. K. Varga , A. Gupta and S. N. Kane J. Magn. Magn. Mater. 320 (2008) e828.

[41] F. Celegato, M. Coïsson, S. N. Kane, F. Mazaleyrat, S. S. Modak, P. Tiberto, L. K. Varga, F. Vinai, Physica Status Solidi a 205 (2008) 1749.

CHAPTER 2

Preparation and micro-structural investigation of amorphous and nanocrystalline FeZrNbBCu ribbons

This chapter gives a brief introduction of the experimental methods used for the preparation and the structural characterization of as cast and nanocrystallized ribbons of nominal composition $Fe_{84}Zr_{3.5}Nb_{3.5}B_8Cu_1$. Samples in amorphous state were subjected to controlled partial crystallization by employing thermal treatment in an inert atmosphere. Complementary information and results obtained by room temperature X-ray diffraction and Mössbauer measurements, for identification of nanocrystalline phase, local compositional changes occurring in nanocrystalline phase and related parameters e.g. lattice constant, average grain size, volume fraction of nanocrystalline phase, are also reported.

- ***Technique for preparation of amorphous ribbons***
- ***Differential scanning calorimetry***
- ***X ray diffraction measurements***
- ***Mössbauer spectroscopy analysis***
- ***References***

2.1 Technique for preparation of amorphous ribbons

Amorphous alloys are materials with noncrystalline state that is a result of some non equilibrium process. This non equilibrium process, typically known as rapid solidification, often includes a very fast removal of heat energy from alloy system in molten state. This rapid quenching also requires at least one dimension of alloy system to be small enough so that heat transfer can be carried out easily. Fast cooling prevents the establishment of long range structural and chemical order. Usually in order to stabilize the disordered state it is required to add some glass forming elements like boron, carbon, silicon etc. Absence of long range order results in no grain boundaries, and almost no micro structural inhomogeneties like precipitates and segregation. For this reason leave amorphous alloys exhibit properties governed by a short range order interaction e.g. low corrosive behaviour, high resistivity, and low magnetocrystalline anisotropy, improved mechanical and magnetic properties. Amorphous materials date back in nature and history of human civilization as the oldest human made amorphous solids are reported to be in Mesopotamia and Egypt about 1500 B.C which was the result of a bad cooking of ceramics. Formation of some amorphous solid minerals naturally occurred in geologic periods by volcanic eruptions such as obsidian. The first silica glasses are reportedly from the Middle Orient toward 300 B.C. [1].

The first metallic glass was made in 1934 by Krammer [2] using the chemical vapour deposition technique. Apart from conventional synthesis routes e.g. casting, crystal growth, rolling etc. bulk amorphous alloys are typically formed by rapid solidification processing routes. Duwez developed a method to produce amorphous $Au_{75}Si_{25}$ through quenching the melt by atomizing it against a cold substrate [3]. Later Miroshninenko and Salli [4]

discovered the splat-cooling method which employed squashing the melt using two pistons. Actually, this second method led to the first device allowing the production of long length amorphous magnetic ribbons by Pond and Maddin [5] in 1969 which are now commercially produced by companies like Vacuumschmelze. In the early stages of the development in processing of metallic glasses, Fe-P was mainly used as the melt spun material but since the commencement of industrialization of the processing techniques in late 1970's (Fe, Ni, Co)-B-based alloys were produced primarily. Iron based alloys usually were ternary or quaternary systems composed of 74–80 atomic percent of iron, 15–20% of silicon and boron in balance with a small amount of additives like carbon or chromium. On the other hand cobalt-based alloys comprised of 65–75% cobalt, 10–15% boron, 5–15% silicon and a small percentage of several transition metals. Iron-nickel based alloys basically composed of Fe and Ni in majority (~80%) with about 18% of Boron and several additives (Mo, Si etc). Since the year 1990 melt spinning of Fe-Co alloys have added a new family of alloys to the list. With the commencement of the industrial production of amorphous ribbons, by the early 1980s, the melt spinning and planar flow casting systems were standardized as quenching apparatus allowing the continuous casting of ribbons at a speed of some 40 ms^{-1}. The basic requirement of producing amorphous alloys is rapidly quenching the molten alloy mixture and this can be fulfilled by achieving very high cooling rates. In order to achieve higher cooling rates, the molten alloy is projected on a cold substrate with a small thickness depending on the glass forming ability of the alloy. The continuous production of amorphous alloy is possible if the substrate moves with sufficient speed to keep a very small liquid thickness. In practice the jet of molten alloy is spew out of a nozzle with a small hole at a distance of few mm from a rotating wheel. As a consequence, the thickness

of ribbon depends on melting temperature, viscosity, pressure, diameter of hole through which the molten alloy is ejected, and the speed of wheel. It also depends upon the characteristics of the substrate e.g. thermal conductivity, ability to be wet, and also the reactivity with the alloy. For above said reasons, the wheel is generally made from copper alloys. The method melt spinning casting, as it is usually known, allows the production of 1–15 mm wide ribbons with a nominal thickness ranging between 10 - 50μm. To make wider ribbons the twin roller and the planar flow casting methods are considered better methods. As shown in figure 2.1.1 the twin roller method [1] employs squashing of alloy between two wheels, but it was realized that this process is very delicate because of the proximity of wheels (about 50 μm) which requires very high precision regarding parallelism, roughness and cylindrical symmetry. On the other hand the planar flow casting technology uses a single roller similar to that of the melt spinning apparatus (see fig. 2.1.1) but the nozzle, that allows the molten alloy to flow through, is quite different. In this case instead of a circular nozzle hole it is in the form of a slit. If the nozzle is located close enough to the wheel's radial surface, the ribbon has exactly the width of the slit. This process has two major advantages over the melt spinning technique apart from the difficulties in slit machining. First, the width of ribbon is constant and is least affected by the speed of wheel. It is not too sensitive to the temperature and pressure of melt also. Secondly the width of ribbon, constrained by the size of slit, can reach 25cm in industrial production. These amorphous alloy ribbons of appropriate chemical compositions crystallized at temperatures above their primary crystallization temperature but below the secondary crystallization temperature, can yield nanocrystalline grains with an amorphous inter granular material. The properties (see also Chapter 1) of these nanocrystalline

materials are very different than what would have been expected on the basis of constituent elements in the amorphous state. Crystallization parameters can be optimized in a way so as to yield an ultrafine grain structure comprising of 10-50 nm α-Fe-Si, α -Fe, α or α '-Fe-Co grains surrounded by a thin inter granular phase (TL-TE-B-Cu) comprising of late and early transition element along with B and Cu. The initial precursor material is fully amorphous. Cu rich small clusters serves as nucleating agents and the nanocrystals nucleates at the site of incipient clustering. Nanocrystalline phase grows while expelling the additives e.g. B, Nb etc to inter granular region. By and large the crystallization process is performed by inert gas furnace annealing. The resulting structure gives rise to many interesting aspects as far as the soft magnetic properties are concerned. This is the basis of the processing routes used to produce the interesting family of alloys namely FINEMET, NANOPERM and HITPERM.

The amorphous ribbons of nominal composition $Fe_{84}Nb_{3.5}Zr_{3.5}B_8Cu_1$ were prepared by planar flow casting method; the ribbons were 15mm wide and have typical thickness of about 20μm. Ribbon samples of about 7cm length were used for various characterizations in as cast and nanocrystalline state obtained after thermal annealing treatment.

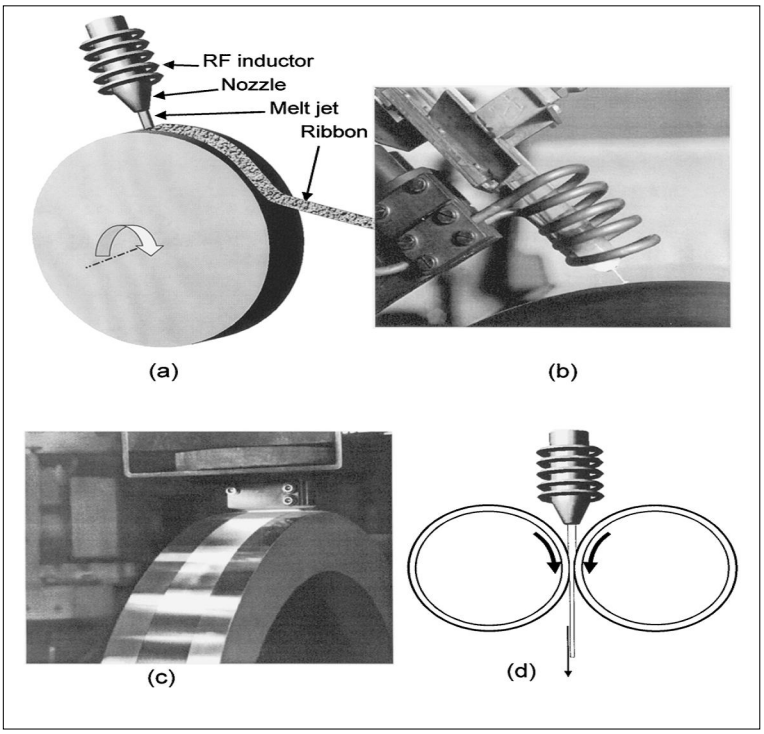

Figure 2.1.1: Various casting methods used for rapid quenching of amorphous metallic ribbons, (a) Sketch of the planar flow casting method (b) Detailed view of the planar flow casting apparatus (c) Planar flow casting apparatus (d) Twin roller scheme.

2.2 Differential scanning calorimetry

2.2.1: Introduction

Understanding the onset of crystallization process is of significant interest in the study of amorphous and nanocrystalline magnetic alloys. As in case of an alloy that shows superior magnetic properties in its amorphous phase the crystallization process gives an idea of the limit at which the magnetic properties start to deteriorate. So in a way thermal stability gives a good idea of the magnetic stability of the amorphous phase. On the other hand in case of nanocrystalline alloys that exhibit excellent magnetic properties with a microstructure comprising of nanocrystallites hosted in an amorphous matrix, understanding the crystallization process can help in tailoring e.g. the amount of nanocrystallites formed within the matrix. This way desired magnetic performance could be schemed on the basis of crystallization behaviour. In particular, chemical composition can be a deciding factor that stabilizes a fine microstructure starting from an amorphous precursor starting material. The process of crystallization from the metastable amorphous phase to stable crystalline state depends upon various parameters like the composition, concentration of nucleation sites, diffusion coefficients of various components, the activation energy for diffusion, the free energy difference between the amorphous and possible nanocrystalline phases and also on the thermal history of the system [6, 7]. There are three basic modes that well describe the process of crystallization of an amorphous alloy.

- Polymorphous crystallization: Polymorphous crystallization describes the crystallization of an amorphous phase to a crystalline phase without any change in the composition. The transformation typically forms a metastable or supersaturated

alloy that leads to a precipitate reaction finally reaching a stable state. No concentration difference occurs during this transformation

- Primary crystallization: An amorphous to crystalline transformation, accompanying crystallization of a phase of one of the constituents of the alloy system first, is termed as primary crystallization event. This dispersed primary crystallized phase coexist with the amorphous matrix and may serve as the nucleation site for the secondary or tertiary crystallization. Subsequent growth of these crystallites results in a loss of amorphous precursor and results in another metastable equilibrium.
- Eutectic crystallization: Eutectic crystalline transformation is based upon simultaneous crystallization of two crystalline phases occurs by a discontinuous reaction. This reaction has no concentration difference across the reaction front but it takes longer time as the two components have to separate by diffusion into two separate phases within the crystallized region.

Crystallization process of an amorphous material is indicated by the change in heat flow with the temperature or time.

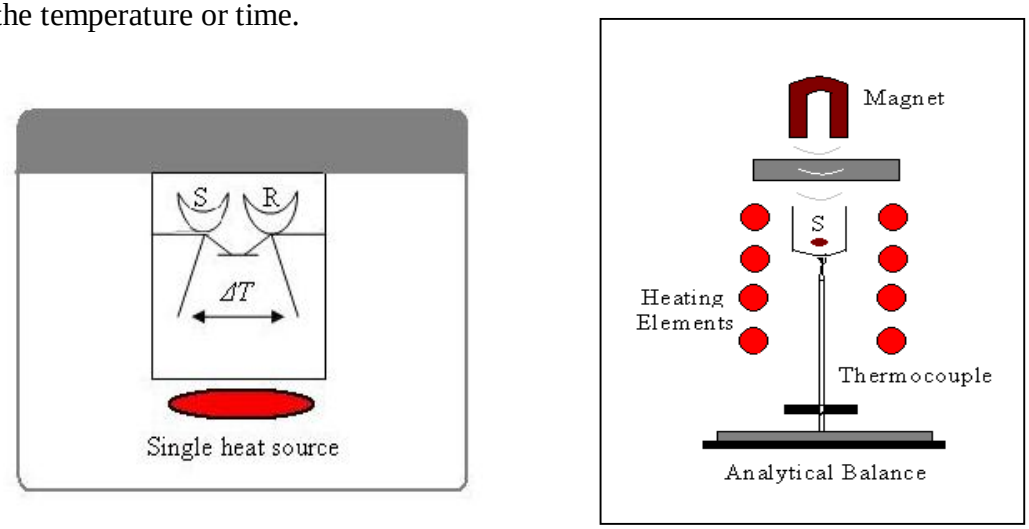

(a) **(b)**

Figure 2.2.1 Schematic of **(a)** differential scanning calorimeter **(b)** TGA apparatus.

The differential scanning calorimetry is a standard method employing the measurement of the difference in the heat required to maintain a constant temperature between the sample under investigation and a standard reference to monitor the changes in heat flow with temperature or time. Basically this method is useful for the study of meta stable systems and it widely finds applications in fields other then material sciences. Figure 2.2.1 (a) shows the basic scheme of a heat flux differential scanning calorimeter. Sample is placed in (S) one pan generally made of high purity alumina and another identical empty pan is used as (R) reference. The sample chamber is kept in an inert environment. The temperature is measured in both pans to determine the heating or cooling curves of sample. In TGA experiment change of phase from magnetic to non magnetic state is indicated by the change in the apparent weight of the sample S as the force between the sample and magnet changes as depicted in figure 2.2.1 (b). Basically differential scanning calorimetry follows Newton's law of cooling i.e. the rate at which the heat is transferred from the surface of a solid to a fluid with in contact is proportional to the difference between the temperatures of the solid and that of the fluid. It also depends simultaneously upon the area through which the flow occurs. The outcome of a typical calorimetry experiment is the variation of temperature, mass (TGA) and heat flow (DSC) as a function of time. The DSC signal describes the heat flow required to keep the sample and reference material at the same temperature. A difference in heat flow corresponds to exothermic or endothermic reactions inside the sample e.g. change of phases, change of state like melting or evaporation. Basically this kind of analysis is accompanied by reactions that bring about the differences in mass and thermo physical properties of sample and the reference. The change in heat flow versus temperature or time, whether exothermic or endothermic, can be monitored in order to

determine the onset of crystallization, the peak crystallization temperature, secondary crystallization events and the transformation of phase as a result of heating. Conventionally exothermic reactions in the sample may be shown with a positive or negative peak depending upon the different kind of technology used by the instrumentation to make the experiment. This curve can be used to calculate the enthalpies of transition. This is done by integrating the peak corresponding to a given transition. The enthalpy of transition can be expressed as $\Delta H = KA$; where K is the calorimetric constant, and A is the area under the curve. The calorimetric constant will vary from instrument to instrument, and can be determined by analyzing a well-characterized sample with known enthalpies of transition.

2.2.2: Crystallization of amorphous $Fe_{84}Nb_{3.5}Zr_{3.5}B_8Cu_1$ ribbons

Nanoperm family of alloy is based upon the primary nanocrystallization of α–Fe phase which makes them interesting as they exhibit higher curie points and larger inductions. The amorphous precursor relies on additions of early transition metals (Zr, Nb, Hf) and boron as glass forming elements. Magnetic properties and microstructure after crystallization of Nanoperm family of alloys has been examined [8, 9, and 10] and resulting microstructure was characterized by a 10-15 nm bcc Fe phase. For instance the amorphous alloy composition $Fe_{88}Zr_7B_8Cu_1$ exhibits primary nanocrystallization at 500^{o}C followed by a secondary crystallization at 730^{o}C when the material is heated at a constant rate of 10^{o}C /min. The amorphous precursor to NANOPERM ^{TM} has a curie temperature just above room temperature ~ 77^{o}C and is well below its primary crystallization temperature as identified with following crystallization sequence:

Amorphous $\longrightarrow$ bcc α–Fe + Amorphous' (504^{o}C) $\longrightarrow$ α–Fe + Fe_3Zr (704^{o}C).

In case of $Fe_{86}Zr_7B_6Cu_1$ amorphous alloy primary crystallization of bcc Fe occurs at 687^{o}C followed by secondary crystallization of the Fe_3Zr phase and an unidentified phase at 747^{o}C.

In the present study we have used amorphous ribbon samples of nominal composition $Fe_{84}Nb_{3.5}Zr_{3.5}B_8Cu_1$, with the measured weight of 12 mg ± 2mg, were studied using a Perkin Elmer differential scanning calorimeter (Diamond DSC) at heating rates of 5^{o}C/min, 7^{o}C/min and 10^{o}C/min. Sample were heated from 30^{o}C to 590^{o}C. Figure 2.2.2 a, b and c depicts the heating curves at heating rate of 5^{o}C/min, 7^{o}C/min and 10^{o}C/min respectively. It should be noted that peak temperature does depend upon rate of heating. The peak crystallization temperatures corresponding to three different heating rates are 520^{o}C, 530^{o}C and 543^{o}C. The temperature corresponding to the onset of primary crystallization was determined to be 480^{o}C. Secondary crystallization peaks between 700-750^{o}C for Nanoperm family of alloys has been reported [6, 7, 8] but the range of DSC apparatus used was limited to 600^{o}C and as a result, it could not detect the second transition peak in case of our sample. In order to determine the curie temperature of amorphous and crystalline state, change in the weight of samples as a function of temperature was monitored using Perkin Elmer Pyris 6 TGA apparatus. As shown in figure 2.2.3 amorphous sample was heated from 30^{o}C to 370^{o}C at a heating rate of 5^{o}C/min. The curie temperature of amorphous phase is determined to be ~ 70^{o}C which is above the room temperature. Crystallized samples that were heated at different heating rates during DSC scan were analysed by TGA by heating between 30^{o}C to 900^{o}C at heating rate of 10^{o}C/min. Figure 2.2.4 depicts the TGA curves for the samples crystallized at three different heating rates, showing the curie temperature of crystalline phase to be ~ 700^{o}C.

In order to prepare set of partially nanocrystallized samples temperatures of annealing were chosen in the neighbourhood of the onset temperature of crystallization so that we can have a set of sufficiently small values of crystalline volume fraction. Thermal annealing of 7cm long samples was done in flowing Ar for 60 min at chosen temperatures. Annealing treatment was also performed at 480^{o}C and 490^{o}C for 10, 20 and 40mintues in order to achieve possibly smaller extent of crystallization. Samples were pre annealed at 350^{o}C for 1 hour in order to allow the structural relaxation to remove the quenched in stresses.

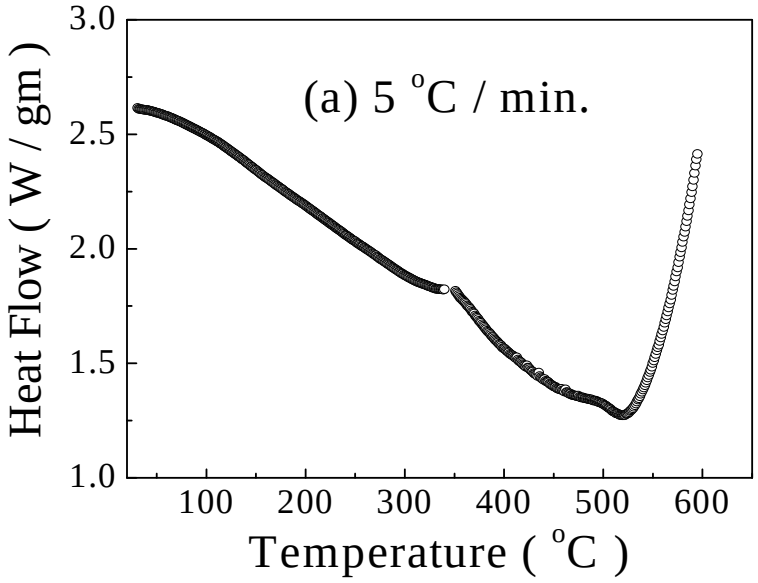

Figure 2.2.2: Crystallization of amorphous $Fe_{84}Nb_{3.5}Zr_{3.5}B_8Cu_1$ determined by DSC at heating rate of **(a)** 5^{o}C/min.

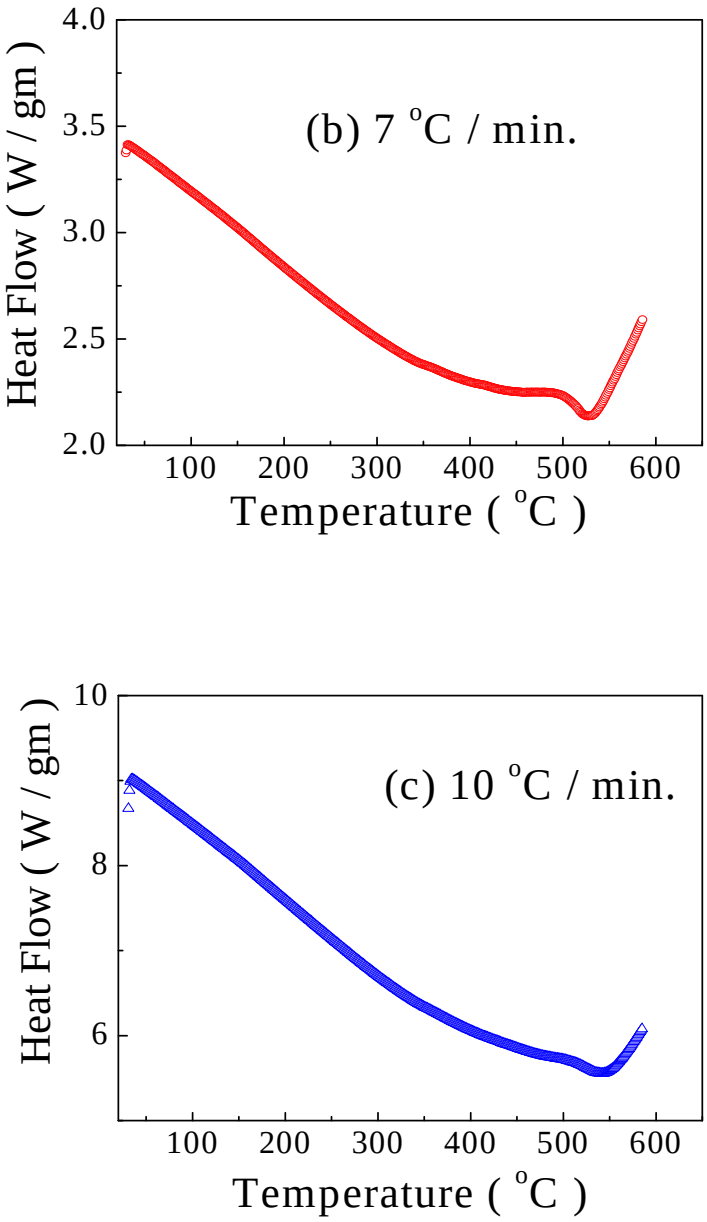

Figure 2.2.2: Crystallization of amorphous $Fe_{84}Nb_{3.5}Zr_{3.5}B_8Cu_1$ determined by DSC at heating rate of **(b)** 7°C/min **(c)** 10°C/min.

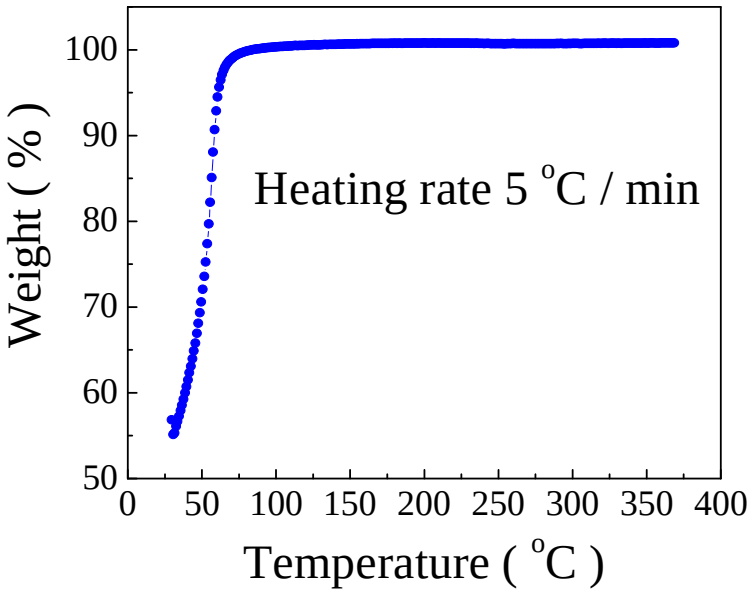

Figure 2.2.3: Curie temperature of amorphous phase of $Fe_{84}Nb_{3.5}Zr_{3.5}B_8Cu_1$.

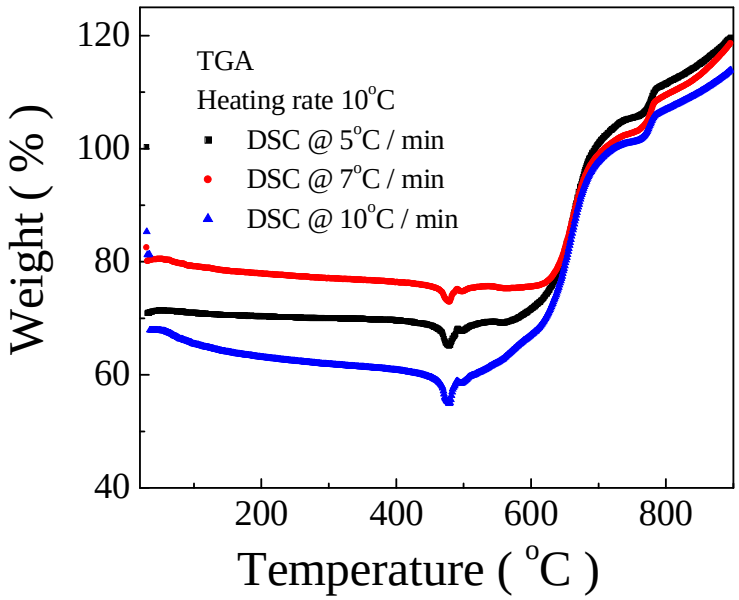

Figure 2.2.4: Curie temperature of crystalline phase of $Fe_{84}Nb_{3.5}Zr_{3.5}B_8Cu_1$.

2.3 X ray diffraction measurements

2.3.1: Introduction

X-ray diffraction method is a versatile non destructive and a non contact analytical technique for identification and quantitative determination of various crystalline forms known as phases of compounds present in the powdered or solid samples under investigation. Another practical advantage of this investigation is that it requires almost no or little efforts for preparation of sample and can be carried out in majority of environments. When X-rays are incident on matter possible interactions that may occur include photoelectric effect, fluorescence, Compton scattering etc. But the interaction that leads to phenomena of diffraction is the elastic collision that takes place between photon and an electron that results in change in the direction of photon without any change in its energy and phase [11]. Figure 2.3.1 shows that coherent scattering takes place when incident X-rays gets scattered from a set of parallel planes of crystal and if the path difference between incident and reflected waves is an integer multiple of wavelength of incident waves. Fulfilment of above condition that gives rise to the constructive interference is commonly termed as Bragg's law:

$$n\,\lambda = 2\,d\,Sin\,\theta \qquad \textbf{- (2.3.1)}$$

where λ is the wavelength of incident X-ray, θ is the angle of incidence; d is the spacing between two consecutive parallel planes and in practice order of diffraction n for a given plane is considered as unity.

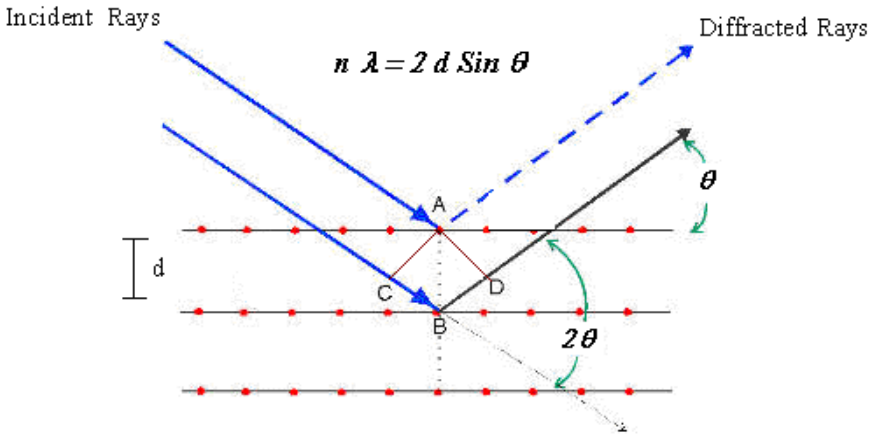

Figure 2.3.1: Braggs condition for diffraction, the distance CB + BD must be an integer multiple of wavelength of incident X-rays.

Conventionally the angle of incidence relative to the surface of sample is varied and the angle of detection is kept equal to it. The result of X-ray diffraction experiment is a pattern showing the phases present (depicted by the position of the peak corresponding to maximum intensity), phase concentration (related to the height of corresponding peak), amorphous content (represented by background hump) and the crystallite size (determined by width of respective peak). Schematic of an intensity peak for a crystalline material is depicted in figure 2.3.2. The width of the diffraction curve decreases as the size of the crystallites decreases. The width W is measured in radians at intensity equal to half of the maximum intensity and can be represented as $W = f(2\theta)$. The thickness through which the diffraction occurs is evaluated using Sherrer formula:

$$D = 0.9\,\lambda / W \cos\theta_W \qquad \text{–(2.3.2)}$$

where λ is the wavelength of radiation used, θ_W is the position of peak and W is the full width at half maximum. For crystalline materials equation 2.3.2 is used to determine the average size of very small crystallites from the measured width of their diffraction curves.

In case of amorphous materials the thickness gives an approximation that the short range order is a factor greater than inter atomic distance if it were crystalline. Materials in the amorphous state exhibit short range order or local ordering as a result X-ray diffraction analysis shows broad peaks with relatively low intensities. The ideal curve for the crystalline solid is almost zero everywhere except at Bragg angles where high sharp maxima occur due to diffracted beams. On the other hand amorphous solid has a structure characterized by complete lack of periodicity. Atoms are packed tightly together and show statistical preferences for particular inter atomic distance. The result is an X-ray scattering curve showing one or two broad humps. However parameters like width of slits, imperfect focusing, and source line widths also contribute to the broadening of diffracted intensity pattern.

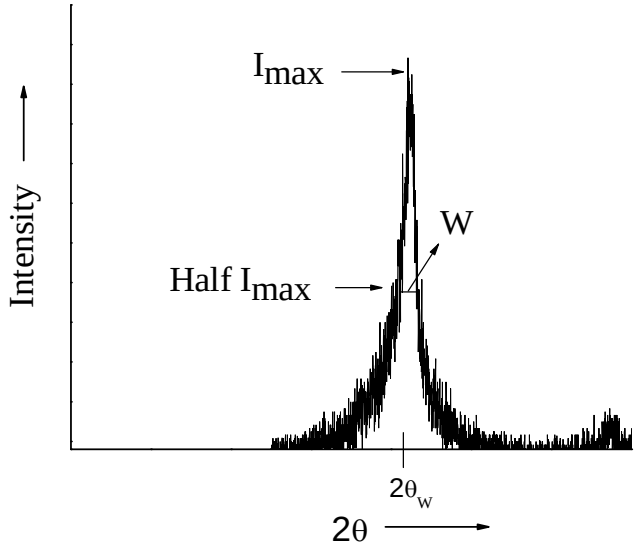

Figure 2.3.2: Schematic curve representing intensity peak from X-ray diffraction analysis for a crystalline material.

2.3.2: *Nanorystallization of amorphous $Fe_{84}Nb_{3.5}Zr_{3.5}B_8Cu_1$ ribbons*

X-ray diffraction measurements, as shown in figure 2.3.3, on as-cast and thermally annealed samples were performed with Co-K_α radiation using X-pert diffractometer. X-ray diffraction patterns were analyzed by fitting a crystalline and amorphous component using pseudo-Voigt line profile in order to obtain average grain size *D* (by using eq.2.3.2), lattice parameter *a* and crystalline volumetric fraction V_x . In order to have a set of low crystalline volume fraction, samples were annealed at 480 and 490 ^oC for different times also. Table 2.3.1 summarizes the annealing temperature dependence of evolution of micro structural properties as a result of nanocrystallization. X- ray diffraction reveals the amorphous state of the as quenched state of ribbons. Figure 2.3.3 shows that the crystallization starts after annealing of the specimen at 470^oC, exhibiting the co-existence of crystalline phase and the residual amorphous matrix with a changed composition.

Table 2.3.1 depicts the annealing temperature and time dependence of the average grain size *D*, volume fraction of the nanograins V_x and lattice parameter *a,* for annealed samples, obtained by analyzing X-ray diffraction patterns. Perusal of table 2.3.1 shows that the volume fraction of nanocrystals ranges between 15 to 48 % whereas the corresponding grain diameter of the nanograins ranges between 7 to 10 nm. It should be noted that with increasing annealing temperature, the increase of volume fraction is faster as compared to the growth of the nanograins. Obtained lattice parameter ranges between 0.2672 to 0.2782 nm, revealing the presence of Fe-rich bcc crystalline phase. Obtained lattice parameter is smaller than that of Fe (0.286 nm) and can be explained on the basis of presence of small

amount of boron in the nanocrystals as observed earlier [12], so presence of small amount of boron affects the lattice parameter in the similar manner as the Si does [13].

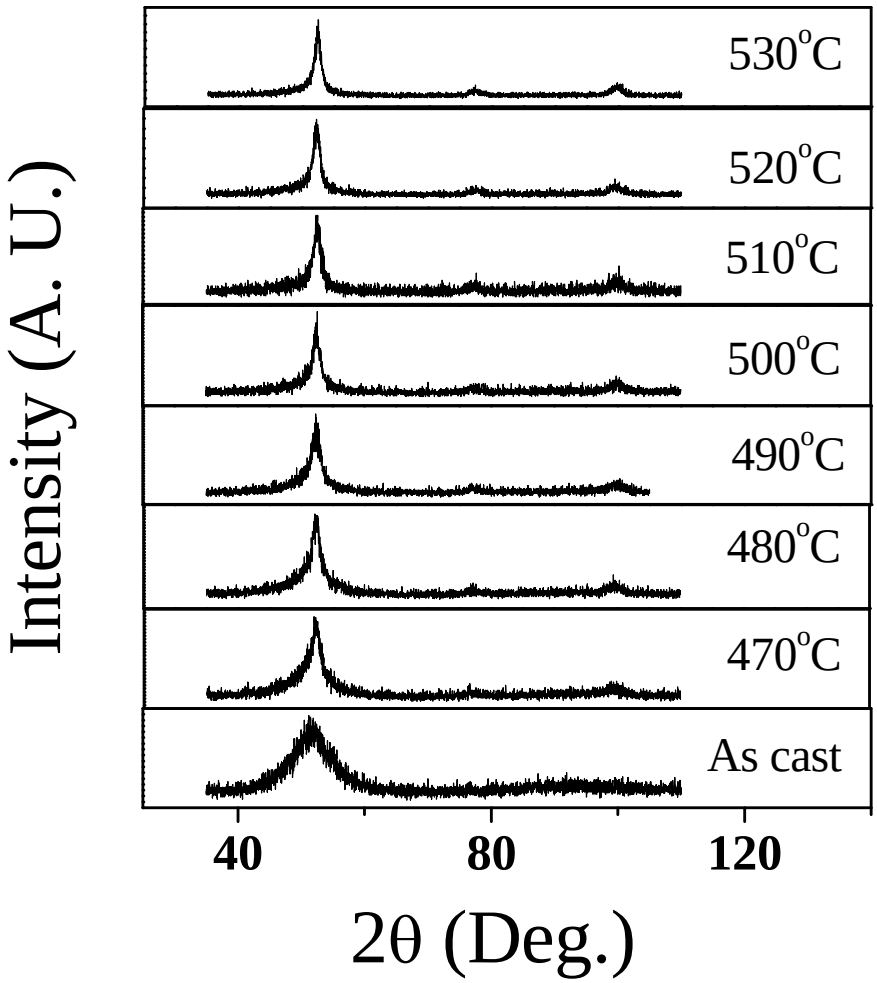

Figure 2.3.3: Representative XRD patterns showing annealing temperature dependence of crystalline phase for the $Fe_{84}Nb_{3.5}Zr_{3.5}B_8Cu_1$ samples annealed for 60 minutes at various temperatures. All samples were pre annealed at 350°C for 60 minutes.

Table 2.3.1: Annealing temperature dependence of V_x, D and a (lattice parameter**)** for the studied composition $Fe_{84}Nb_{3.5}Zr_{3.5}B_8Cu_1$.

Annealing Time (in minutes)	**Annealing Temperature (^{O}C)**	V_x **(%) (±2)**	D**(nm) (±1)**	**Lattice parameter (nm)**
60	470	15.9	7.42	0.26720
10	480	16.2	7.68	0.26728
20	480	17.6	7.8	0.26867
40	480	18.4	8.2	0.26892
60	480	19.5	8.38	0.27129
10	490	20.1	8.48	0.27252
20	490	21.4	8.78	0.27494
40	490	22.8	9.1	0.27622
60	490	23.2	9.25	0.27678
60	500	27.8	9.4	0.27683
60	510	31.2	9.52	0.27688
60	520	36.4	9.6	0.27701
60	530	48.6	10.2	0.27824

Figure 2.3.4 depicts the variation of the micro structural parameters with the annealing temperature. The primary crystallization of bcc Fe is essentially controlled by diffusion processes and is therefore accompanied by changes of the chemical composition in the environment of growing crystallites. It brings about changes in the stress exerted by the amorphous phase. It should also be noted that as the density of crystalline phase is higher than that of amorphous phase hence formation of nanocrystallites may also result in an effective decrement in the volume. Thermal expansion may partly contribute to the increase in lattice constant. The growth of bcc Fe is controlled by the lower diffusion of Nb and Zr which eventually leads to nanocrystalline structure. It should be noted that lattice parameter is increasing at lower annealing temperature which may be considered as an indication of formation of a metastable solution of Nb and/or Zr in the first stages of crystallization [14]. At higher annealing temperatures lattice parameter remains practically constant as only small amount of Zr is soluble in bcc Fe [15] as the equilibrium state is reached.

From figure 2.3.4 it can be inferred that the growth rate of crystallite size is slow initially. It may be noted that lattice parameter and grain size does not increase after 490^{o}C. This indicates that the composition of nanocrystalline phase remains independent of the annealing temperature and time for higher annealing temperature. At higher annealing temperature the average size of crystallite is not changing much. It may be attributed to the accumulation of slowly diffusing inhibitors at the surface of crystallites. The increasing annealing temperature increases the rate of diffusion of Cu, which acts as nucleating agent; thereby the process of crystallization takes place rapidly. It can be easily seen, in figure 2.3.4, as volume fraction of nanocrystalline phase is increasing faster with annealing temperature than the rate at which crystallites are growing.

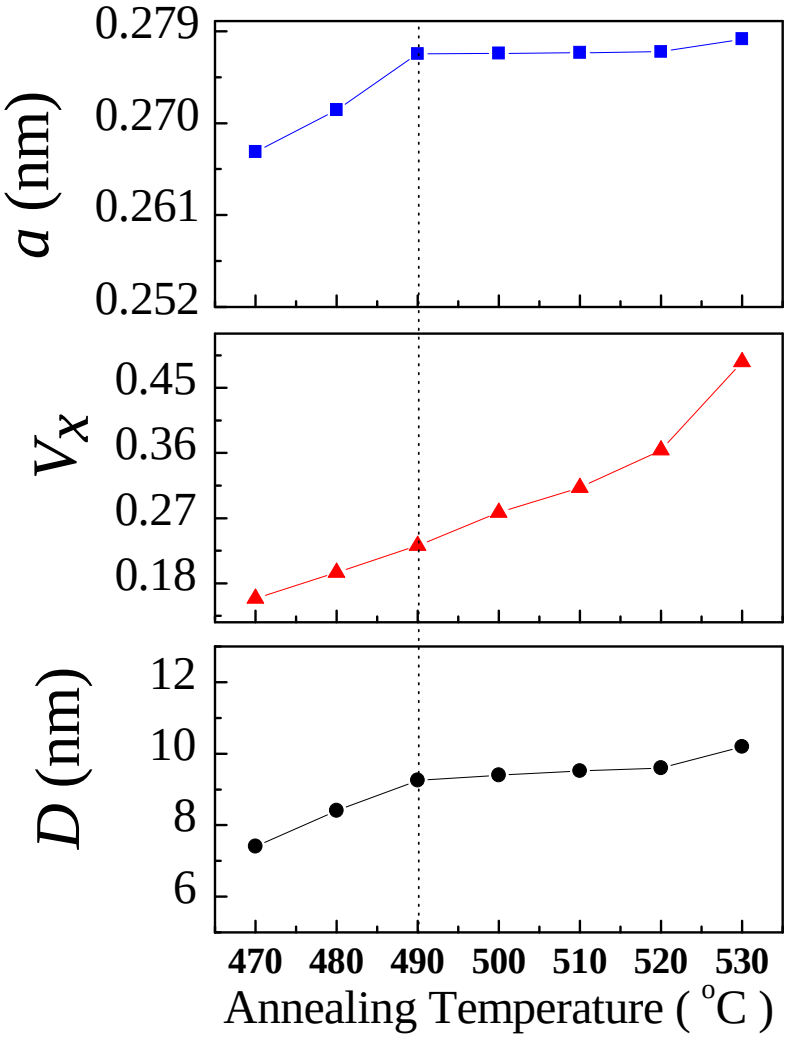

Figure 2.3.4: Annealing temperature dependence of V_x, ***D*** and ***a*** lattice parameter for the nanocrystalline phase for the Fe_{84} $Nb_{3.5}$ $Zr_{3.5}$ B_8Cu_1 samples annealed at various temperatures for different times.

2.4 Mössbauer spectroscopy analysis

2.4.1: Introduction

The Mössbauer effect refers to the recoilless gamma ray resonance absorption. This is the basis for Mössbauer spectroscopy which is commonly used as a probe of local environments and magnetic structure in solids. Nuclei in atomic system undergo a variety of energy level transition associated with the emission or absorption of gamma rays. The magnitude of energy associated with the transition among nuclear levels is about three orders of magnitude larger as compared to the electronic level transitions. As a result of high gamma ray energy, as shown in figure 2.4.1(a), the emitting atom is recoiled back and therefore in a free atom the nucleus recoils due to conservation of momentum just like a gun recoils when firing a bullet, resulting in the emission of gamma ray of energy lower than the nuclear transition energy and same is also observed during gamma ray absorption when absorbing nucleus recoils.

(a)

(b)

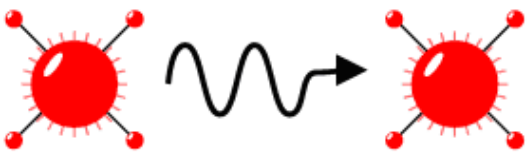

Figure 2.4.1: (a) Recoil of free nuclei in emission or absorption of a gamma-ray.
(b) Recoil-free emission or absorption of a gamma-ray when the nuclei are in a solid matrix such as a crystal lattice.

In 1957 Rudolph Mössbauer [16] discovered the phenomenon of recoil free nuclear resonance fluorescence in solids which later became to known as Mössbauer effect that involves the decay of a nucleus from an excited state to its ground state with the emission of γ-ray. In a solid the whole lattice takes up the recoil energy required for momentum conservation as depicted in figure 2.4.1 (b). The large mass of the lattice means that the recoil energy ($P^2/2m$) is negligible and the γ-ray energy is precisely the difference in energy between the excited and ground states of the emitting nuclei. An emitted γ - ray can in turn be absorbed to pump a nuclei into it's excited state; where after a mean lifetime t it will fall back into the ground state re-emitting the γ – ray in an isotropic manner. This γ - ray resonance fluorescence is used as a spectroscopic tool when the emitted γ -ray energy is

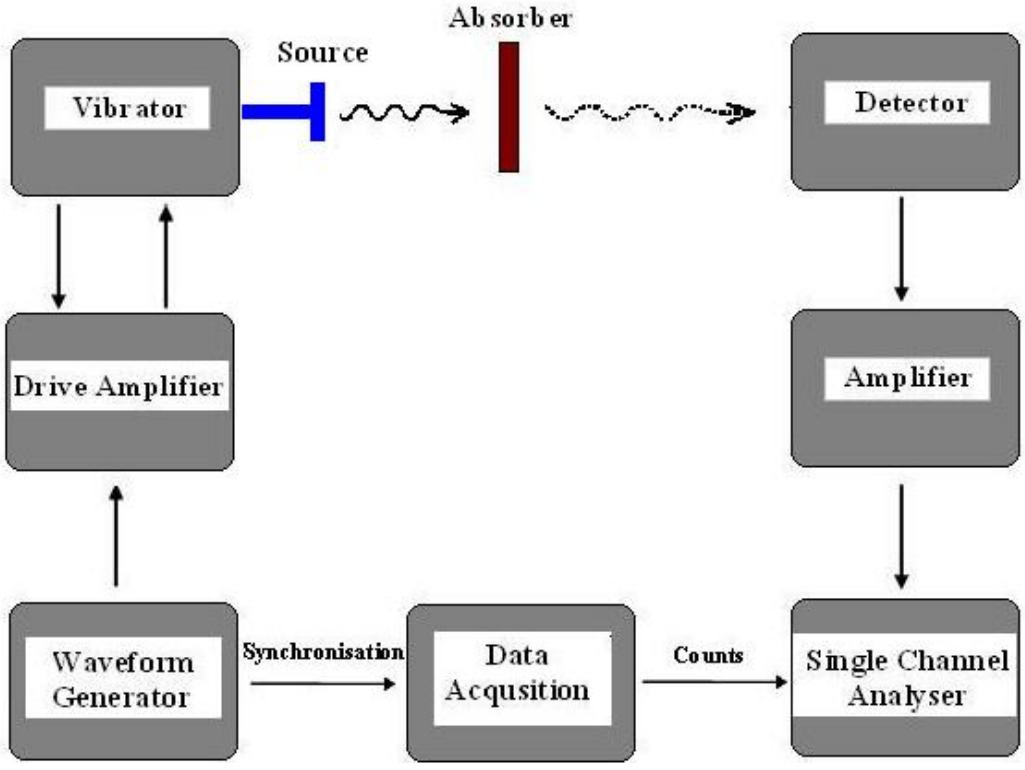

Figure 2.4.2: Basic scheme of Mössbauer spectrometer

modulated by a Doppler shift associated with the harmonic motion (relative velocity) of the γ -ray source and the emitting nuclei. This Doppler energy shift is given by $E = (v/c)\ E_\gamma$ where v is the source velocity, c is the speed of light and E_γ is the γ -ray energy. Using this method it is possible to measure the energy of nuclear levels with high accuracy which plays an important role in determining the slight variations in the nuclear energy levels caused by monopole and dipolar electric, and magnetic dipolar interactions between nucleus and electrons. The two conventional methods employed in order to obtain a Mössbauer spectra are: Transmission Mössbauer spectroscopy and Conversion electron Mössbauer spectroscopy. Transmission Mössbauer spectroscopy gives information of the changes in environment in the bulk whereas Conversion electron Mössbauer spectroscopy reveals the information of the surface of the system under investigation. Figure 2.4.2 presents a basic scheme of a transmission Mössbauer spectrometer.The source velocity is controlled by a transducer which is oscillated with constant acceleration. A waveform generator sends a reference waveform to the drive amplifier, via a digital to analogue converter. This signal is sent to the vibrator where it is converted to a mechanical oscillation of the drive shaft and source. A small coil within the vibrator provides a feedback signal to correct any deviations from the reference waveform. The detector is generally a proportional counter containing a 90% argon and 10% methane gas mixture. The pulse magnitude from the detector is directly proportional to the γ -ray energy and is sorted by a single channel analyser after amplification. This allows the selection of the Mössbauer γ -ray from any other radiation emitted from the source. The detector counts and source velocity are synchronised by a microprocessor system. The counts accumulate in 576 channels for one complete cycle, which contain two complete spectra: one for positive

acceleration and one for negative acceleration of the source. As the acceleration is constant the time interval is equal for all velocity intervals, hence each channel records for the same amount of time. During analysis the full spectrum is folded around a center point to produce a single spectrum. This increases the number of counts (and hence gives better statistics) and flattens the background profile produced by the difference in intensity of the source radiation as the source moves relative to the absorber and detector.

2.4.2: Mössbauer spectra of amorphous and nanocrystalline $Fe_{84}Nb_{3.5}Zr_{3.5}B_8Cu_1$ ribbons

Transmission Mössbauer spectroscopy has been used extensively to identify the phases formed in annealing of NANOPERM^{TM} Fe-M-B alloys e.g. [17], Kopcewicz et al. [18.19] have examined $Fe_{93-x-y}Zr_7B_xCu_y$ (x = 4, 6, 8, 12, and y= 0 or 2) alloys using Mössbauer spectroscopy to follow the formation of nanocrystalline bcc-Fe at annealing temperatures between 430 and 600 ^oC. Brzozka et al. [20] reported a bimodal hyperfine distribution with an additional low field component in the Mössbauer spectra of Fe-Zr-B (Cu) amorphous alloys. The bimodal distribution is interpreted in terms of Fe atoms with nearly full coordination and others partially coordinated by Zr and B atoms. The distribution of Fe-Fe pairs is used to postulate the existence of both ferromagnetic and anti ferromagnetic exchange interactions. Magnetic exchange frustration resulting from this distribution of exchange interactions gives rise to the re-entrant spin glass behavior in this alloy. A strong dependence of the Mössbauer spectra on boron content was observed. Presence of Zr rich component at the surface bcc Fe grains has been reported to affect the magnetic coupling between nanograins in Fe-Zr-B (Cu) alloys [21].

Mössbauer spectra of as cast and nanocrystalline $Fe_{84}Nb_{3.5}Zr_{3.5}B_8Cu_1$ samples were recorded at room temperature in a constant acceleration mode, using ^{57}Co:Rh source. This source is fabricated by diffusing cobalt atoms in rhodium foil matrix. This rhodium matrix provides a solid and non magnetic environment for the ^{57}Co atoms with high recoil free fraction to produce gamma rays. Mössbauer spectra were computer fitted with either distribution of hyperfine fields or overlapping of amorphous and crystalline components by using NORMOS program [22].

Representative Mössbauer spectra and the corresponding hyperfine field distributions of $Fe_{84}Nb_{3.5}Zr_{3.5}B_8Cu_1$ annealed at: (a) different temperatures for 1 hour and (b) annealed at 480 ^{0}C for different times are depicted in figure 2.4.3(a) and 2.4.3(b) respectively. Hyperfine field distributions of the amorphous phase exhibited complex structures as observed earlier [23]. Similar results were reported for some Fe-rich Fe-Zr alloys [24, 25] and the complex hyperfine field distribution was ascribed to the formation of magnetic clusters. In fact, the complex shape of hyperfine field distribution for the residual amorphous matrix is a feature observed in nanocrystalline soft magnetic materials [26, 27]. Figures 2.4.3(a) and 2.4.3(b) shows differences in the hyperfine field distributions with increasing annealing temperature and time, which can be ascribed to the modification of the environment around Mössbauer atom.

Figure 2.4.4(a) shows the variation of average hyperfine field (B_{hf}) and the crystalline fraction (%) with annealing temperature whereas Figure 2.4.4(b) shows the effect of the annealing time (for the sample annealed at 480^{o}C). Perusal of figure 2.4.4 (a, b) shows that the crystalline fraction of the nanocrystals ranges between 16 to 56 %.

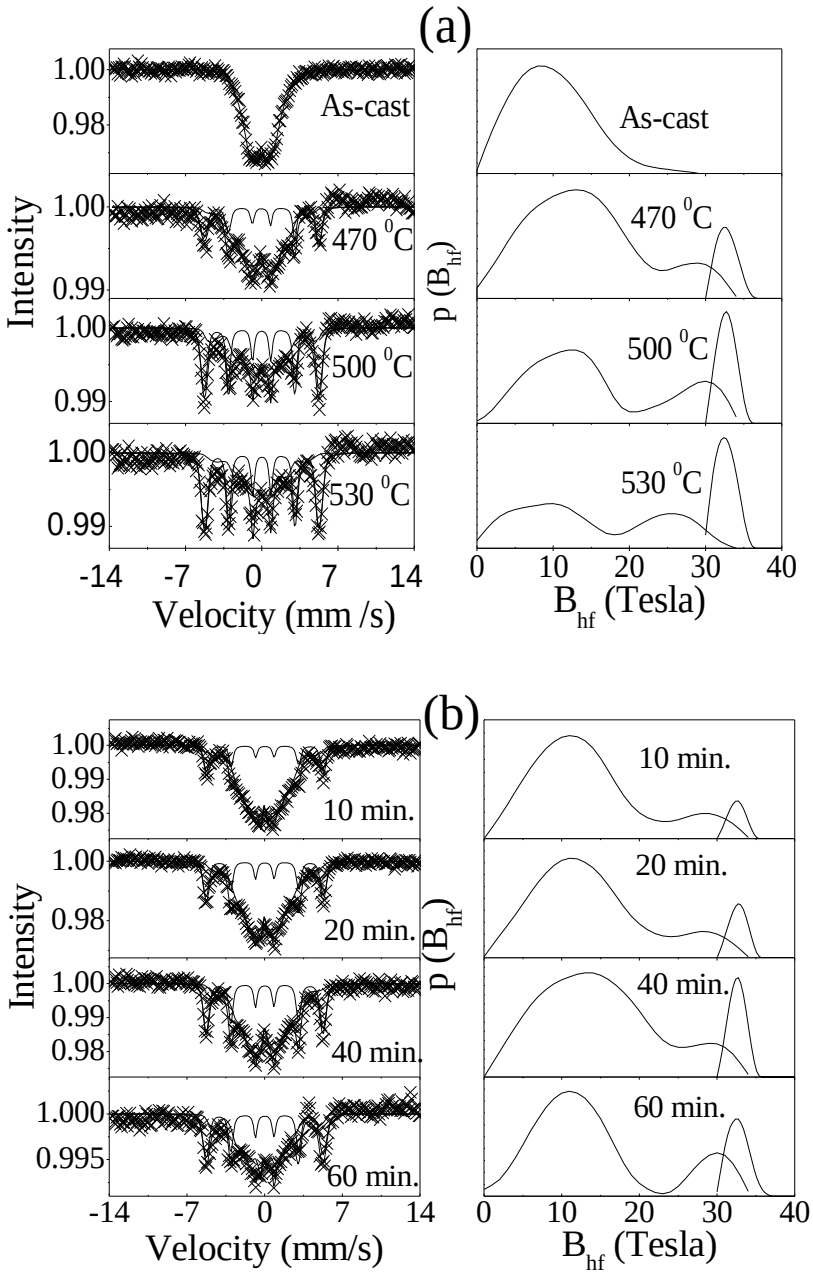

Figure 2.4.3: Representative Mössbauer spectra and the corresponding hyperfine field distributions of $Fe_{84}Nb_{3.5}Zr_{3.5}B_8Cu_1$ annealed at **(a)** different temperatures for 1 hour and **(b)** 480 ^oC for different times.

Observed difference in the crystalline fraction obtained from XRD and Mössbauer measurements can be explained by the fact that Mössbauer measurements looks selectively for Fe present in the phase whereas XRD measurements reveal the presence of all elements in the crystalline phase. In figure 2.4.4 (a, b) variation of average hyperfine field B_{hf} of the crystalline component as a function of annealing temperature and time varies between 32.50 to 32.78 Tesla.

It is worth noting that B_{hf} value for pure iron is 33.33 Tesla and the obtained lower value of B_{hf} for the crystalline component (by $\approx$ 1 Tesla as compared with the B_{hf} value for pure iron) suggests the formation of Fe-rich nanocrystalline phase with small amount of non-magnetic element (boron), resulting in the decrease of B_{hf} value as compared with that of pure iron, also suggested by XRD measurements and discussed above. Obtained lower B_{hf} values for the residual amorphous matrix, ranging between 13.5 to 15.8 Tesla (as shown in figure 2.4.4), suggests the presence of non-magnetic elements (e. g. – Nb, Zr, B) in the Fe-near neighbor shell, thus reducing the magnetic moment of iron, contributing to the decrease of B_{hf} values of the residual amorphous matrix as shown in figure 2.4.4 .

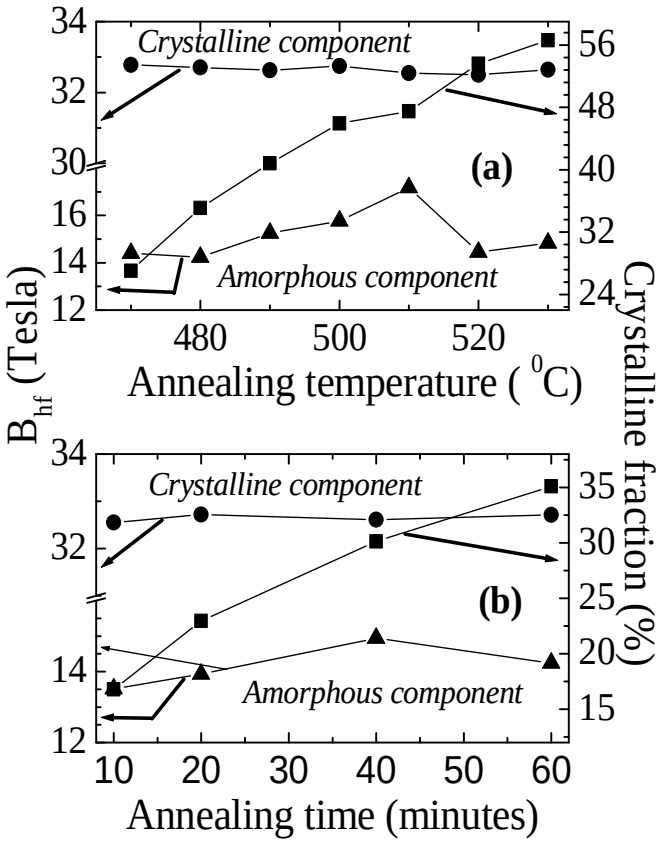

Figure 2.4.4: Dependence of average hyperfine field (B_{hf}) and the crystalline fraction on: **(a)** Annealing temperature and **(b)** Annealing time at 480 ^{o}C.

References:

[1] F. Mazaleyrat, R. Barrué, Handbook of Advanced Electronic and Photonic Materials and Devices, Vol. 6: Nanostructured Materials, edited by Nalwa, Academic press (2001) 59-102.

[2] P. Duwez, S. C. H. Lin, J. Appl. Phys. 38 (1967) 4096.

[3] J. Krammer, Ann. Phys. 19 (1934) 37.

[4] I. S. Miroshninenko and I. V. Salli, Ind. Lab. 25 (1959) 1463.

[5] R. Pond, R. Maddin, TMS-AIME 245 (1969) 2475.

[6] Takahara, Yoshihiro, Mat. Trans. JIM 37 (1996) 1453.

[7] Hornbogen, E. I. Schmidt, Liquids and Amorphous Metals edited by E. Lushcher, H. Coufal, Sijthoff and Nordhoff, Alphen 353-380 (1980).

[8] K. Suzuki, A. Makino, N. Kataoka, A. Inoue, T. Masumoto, Mat Trans JIM 32 (1991) 93.

[9] K. Suzuki, A. Makino, A. Inoue, T. Masumoto, J Appl Phys 70 (1991) 6232.

[10] K. Suzuki, M. Kikuchi, A. Makino, A. Inoue, T. Masumoto, Mat Trans JIM 32 (1991) 961.

[11] R. L. Snyder, X-ray characterization of materials, Wily-VCH New York, 1999.

[12] Y. Zhang, J.S. Blazquez, A. Conde, Paul J. Warren and A. Cerezo, Mater. Sci. Eng A 353 (2003) 158.

[13] R. M. Bozorth, Ferromagnetism, IEEE Press, Trenton (1993), p. 192.

[14] A.Makino, A. Inoue and T. Masumoto, Material Trans. JIM 36 7 (1995) 924.

[15] P. Villars and L. D. Calvert, Pearson's Handbook of crystallographic data for inter metallic phases, The Materials Information Society 1991.

[16] R. L. Mössbauer, Z. Physik 151 (1958) 124.

[17] A. Cserei, J. Jiang, F. Aubertin, U.Gonser J. Mat. Sci. 29 (1994) 1213.

[18] M. Kopcewicz, A. Grabias, P. Nowicki Mat. Sci. Eng. A 226-228 (1997) 515.

[19] M. Kopcewicz, A. Grabias, D. L. Williamson J Appl. Phys. 82 (1997) 1747.

[20] K. Brzozka, A. Slawska-Waniewska, K. Jezuita, J Magn. Magn. Matr.160 (1996) 255.

[21] T. Kemeny, J. Balogh, I. Farkas, D. Kaptas, L. F. Kiss, T. Pusztai, et al. J Phys. Condense Matter10 (1998) L221.

[22] R. A. Brand, Nucl. Instr. Meth. B58 (1987) 398.

[23] K. Suzuki and J. M. Codogan, Phys. Rev. B 58 (1998) 2730.

[24] S. N. Kaul, V. Siruguri and G. Chandra, Phys. Rev. B 45 (1992) 12343.

[25] D. Kaptas, T. Kemeny, L. F. Kiss, J. Bologh, L. Granasy and I. Vincze, Phys. Rev. B 46 (1992) 6600.

[26] C. Gomez-Polo, D. Holzer, M. Multigner, E. Navarro, P. Agudo, A. Hernando, M. Vazquez, H. Sassik and R. Grossinger Phys. Rev. B 53 (1996) 3392.

[27] M. Miglierini and J. M. Greneche J. Phys. Conedns. Matter 9 (1997) 2303.

CHAPTER 3

Preparation and micro-structural characterization of FeZrNbBCu thin films

A brief introduction of the experimental techniques that have been used for the preparation of thin films using amorphous ribbons of nominal composition $Fe_{84}Nb_{3.5}Zr_{3.5}B_8Cu_1$ *is presented in this chapter. Complementary structural investigation techniques that were employed are also discussed. Thin film samples in as prepared state were crystallized by performing thermal annealing treatment in vacuum. The central interest of this chapter consists in representing the effect of annealing conditions on the structure of the prepared thin films samples. Various structural characterizations were performed at room temperature.*

- ***Preparation of FeZrNbBCu thin films***
- ***X- ray scattering analysis***
- ***Atomic force microscopy images***
- ***References***

3.1 Preparation of FeZrNbBCu thin films

3.1.1: Introduction

With the advancement of microelectronics, the need for thin film products for electronic and semiconductor layers lead to the development of the "sputtering" of layers using physical vapour deposition (PVD) on to a selected substrate from a "target" bearing the layer material. The term vacuum deposition is often used instead [1, 2] of PVD in older literature. W. R. Grove was [3] the first to study what came to be known as sputtering in 1835. He sputtered from the tip of a wire held close to a highly polished silver surface. With the advancements in sputtering technology; sputtering of thin film layers found application in numerous scientific and industrial fields, including optical and architectural glass, memory storage devices, tool coatings and, most recently, fuel cells and solar energy panels. Sputtering targets are now essential to the coating and manufacturing of optical storage devices such as CDs and DVDs to provide both wear protection and reflectivity. Thin films find a variety of application ranges by offering the properties useful for commercial utility. Magnetic memory devices, thin film resistors, anti reflection coatings, Josephson devices etc. are some of the important areas where thin film system are being capitalized. Magnetic recording media is particularly interesting which include magnetic tapes, hard disks, read and write heads, consumer audio and video equipments, credit cards etc. Depending upon the thickness and the physical properties current thin film applications include magnetic and electrical sensors, waveguides, filters, optical switches interconnectors, holography, piezoelectric coatings, biochemical and environmental sensors, miniaturized photovoltaic and integrated circuits etc.

Sputtering, alternative to evaporation, is a term to describe the mechanism in which atoms are ejected from the surface of a material when that surface is incident upon by sufficiently energetic beam of particles. This was first discovered in 1852 and was later developed as thin film deposition technique by Langmuir in the year 1920. In principle the target is bombarded by energetic ions which eject the target atoms as a result of momentum transfer to the target surface. When an ion approaches the target, one of the following may occur:

1. It may undergo elastic collision and be reflected.
2. It may undergo inelastic collision and be buried into the target.
3. It may produce structural rearrangement in the target material.
4. The impact may set up a series of collisions between atoms of the target leading to the ejection of one of these targets; this process is known as sputtering.

Thus the sputtering process can be likened to a break in a game of "atomic" billiards. The excited ion, representing the cue ball, strikes the atomic array of the target - the neatly arranged pack - scattering them in all directions. Some of these will be ejected in the direction of the original approaching ion i.e. normal to the target surface. It is this ejected particle which is useful for deposition on the surface of the substrate. Hence the sputter process essentially involves knocking an atom or molecule out of the surface of a target. Under the right conditions, the sputtered species will travel through space until it strikes and condenses on the surface of the substrate**.** Basic scheme of sputtering process is shown in figure 3.1.1. Sputtering system consists of an evacuated chamber, a target (cathode) and a substrate table (anode). Two conventional methods used for preparing thin films using sputtering process are ion beam sputtering and RF sputtering. Ion beam sputtering technique employs a separate ion source to produce an ion beam that actually works like an

ion gun that shots the ions onto target material to detach the atoms of the target.On the other hand RF sputtering is an indirect ion beam assisted method that uses argon gas between the target (Cathode) and the substrate (Anode). A plasma discharge of this sputtering gas is then generated by applying RF electric field (~10-20 MHz) inside a sputtering chamber.

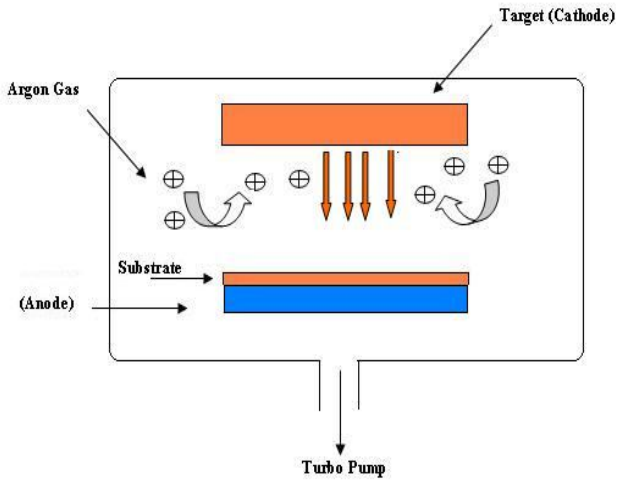

Figure 3.1.1: Schematic of sputtering process

The applied voltage accelerates electrons which collide with argon atoms producing Ar^+ ions. These ions fly towards the target and detach its atoms which then fly towards the substrate to stick and form the film. Ion beam sputtering extends a better control over the energy and current density of bombarding ions as the ion source is kept outside the physical dimensions of the vacuum chamber. Ion beam technique produces negligible re-condensation of sputtered atoms on the target surface thus provides a better composition control also. The beam can have high directionality at any angle. The beam current and energy can be controlled independently. On the contrary plasma assisted RF sputtering restricts the substrate to the perpendicular ion impact in plasma. In general it is considered

that ion beam sputtering has much lower deposition rate as compared to RF sputtering which allows deposition of even non conducting materials at a practical rate. Usual DC sputtering methods cannot be used to sputter non conducting materials because of charge accumulation at the surface of target. RF sputtering overcomes this difficulty as a single RF sputtering apparatus can be used to deposit electrically conducting, semiconducting and insulating coatings. RF sputtering has found wide applications in electronic industry. RF power alone is capable of generating plasma and accelerates the ions towards the target. RF sputtering is though faster but usually gives rough surfaces as compared to ion beam sputtered surface which allows preparation of rather smooth surfaces, interfaces and provides a better thickness control. It may be possible that ion beam sputtering induces anisotropy because there is always a preferential direction decided by the direction in which the ions are shot.

3.1.2: Preparation of thin film samples

(a) Samples prepared by ion beam sputtering technique

One set of thin film samples were prepared by using ion beam sputtering on a silicon substrate (3cm× 3cm) using a target made by amorphous ribbons of nominal composition $Fe_{84}Nb_{3.5}Zr_{3.5}B_8Cu_1$. A Kaufman type broad beam ion source with a plasma chamber inside was used to produce ion beam. It is a hot cathode grided source in which ions are accelerated by multiple aperture grids to produce a broad beam of ions. In the ion source, working gas is introduced in to the discharge chamber through a port in the discharge chamber wall. Working gas is argon gas. Argon gas is used because it is the inert gas so it doesn't react with target material. Electrons from the cathode strike the atoms or molecules

in the discharge chamber and produce ions of argon gas. These ions are formed in to parallel beams by passing them through the screen grid with suitable aperture, which are attracted by the accelerator grid that is negatively charged. The beam passes through the accelerator grid without striking it because of the alignment of the apertures in the two grids. Thus the ion beam composed of the individual beams leaves the accelerator grid and strikes with the target. In case if target is an insulator the ion beam is neutralized by the electrons from neutralizer. To increase the probability of ionization by an energetic electron from the cathode is acted upon by a magnetic field that is applied between cathode and anode using permanent magnets. The ion beam source voltage used was 750V and the corresponding beam current was 20mA. The Energy of bombarding Ar^+ ions was 1keV. It is always the case when an alloy target is used we supposed that the chemical composition is the same as that of the target [4]. Operating pressure in the sputtering chamber was of the order of 1.2×10^{-4}Torr whereas ultimate vacuum in the sputtering chamber was monitored to be ~ 3.2×10^{-7} Torr. Distance between the substrate and target was kept 17cm. Films of three different thickness were sputtered by varying the time of deposition (e.g. 12, 24 and 36 minutes) while keeping all the deposition parameters like beam voltage, beam current almost constant. The samples in this set shall be designated as per following scheme here onwards: (1) IBS 190 12min (2) IBS 190 24min (3) IBS 190 36min. For general addressing these samples will be called IBS samples in this work. Samples (3mm× 3mm) from the above set were subjected to furnace annealed in vacuum (pressure ~ 4×10^{-4} mbar) at 200, 250, 300, 350, 400, 450, 500 and 550^o C for 80 minutes respectively in order to crystallize them.

(b) Samples prepared by RF sputtering method

Second set comprises of thin film samples prepared by RF sputtering on glass substrate starting from a target made by amorphous ribbons of nominal composition $Fe_{84}Nb_{3.5}Zr_{3.5}B_8Cu_1$. The base chamber pressure was ~ 2×10^{-7} mbar and the argon gas pressure was maintained ~ 1.2×10^{-4} mbar. Samples of 11 different thicknesses were prepared by varying the time of deposition and simultaneously keeping the other sputtering parameters fixed. Thicknesses of the films have been estimated from sputtering time after calibration. The samples from this set will be addressed by using names as listed in the Table 3.1.1 along with the thickness as measured using from sputtering deposition time only. Samples were then annealed in vacuum at various temperatures between 200^{o}C and 600^{o}C for 60 minutes. These set of samples will be addressed as RF samples for general context in the present work.

Table 3.1.1: Thickness of RF sputtered thin film samples prepared using glass substrate.

RF Sample	**Thickness (± 2nm)**
RF5	5nm
RF10	10nm
RF15	15nm
RF20	20nm
RF25	25nm
RF30	30nm
RF40	40nm
RF50	50nm
RF64	64nm
RF80	80nm
RF104	104nm

3.2 X-ray scattering analysis

3.2.1: Thickness determination using X-ray reflectivity measurements

(a) Introduction

X-ray reflectivity (XRR) is a non-destructive, non-contacting method to measure film thickness, interface and surface roughness and density of layered structures. XRR is basically a grazing incidence scattering technique, with the incident and scattered beams at equal angles to the surface of the sample. In XRR, X-ray-beam strikes a solid-surface at a small angle ($0–2^{\circ}$) and is totally reflected. X-rays are part of the broad spectrum of electromagnetic waves. The most widely used X-rays in materials science have typical wavelength of the order of 0.1 nm. This wavelength is associated with a very high frequency of the order of 10^{19} Hz which is at least four orders of magnitude greater than the eigen frequency of an electron bound to a nucleus. The scattering of X-rays takes place by electrons and therefore this process is sensitive to the electron density [5, 6, and 7]. This provides the key information of the surfaces and the interfaces in terms of density variation in a non-destructive way. The interaction of X-rays with matter involves acceleration of electrons of the material by the incident X-ray field. Consequently an index of refraction which characterizes the change of direction of the X-ray beam due to interaction with electrons can be written as

$$n = 1 - \delta - i\,\beta \qquad \textbf{–(3.2.1)}$$

where δ and β account for the scattering and absorption coefficient of the material, respectively. The sign preceding β depends on the convention of signs used to define the

propagation of the electric field. The values of δ and β (which are positive) depend on the electron density and linear absorption coefficient of the material is described [7] by the following relations:

$$\delta = \lambda^2 \rho (R_e / 2\pi) \qquad \textbf{– (3.2.2 a)}$$

$$\beta = \lambda (\mu / 4\pi) \qquad \textbf{– (3.2.2 b)}$$

where λ is the X-ray wavelength, R_e= 2.813×10^{-6} nm is the classical electron radius, ρ the electron density, μ is the linear absorption coefficient. The magnitudes of δ and β are simply related to the electron density of the material, and are of the order 10^{-5} to 10^{-7}. The real part, $n = 1 - \delta$, is connected to the phase-lag of the propagating wave whereas the imaginary part, β, corresponds to the decrease of the wave amplitude. When a beam of X-rays falls on the interface of two different media, it suffers reflection and refraction depending upon the angle of incidence and the refractive indices of the media. When X-rays are incident on the material from air such that the incident angle is smaller than the critical angle α_c total external reflection of X-rays takes place. If we consider that negligible absorption of X- rays takes place then we may write for the critical angle for reflection:

$$\alpha^2_c = \lambda^2 \rho (R_e / \pi) \qquad \textbf{–(3.2.2 c)}$$

Thus measurement of the critical angle provides the determination of the density of the material. Whereas the thickness of the film is measured from the periodicity of reflectivity fringes, the density from the angle at which the intensity begins to drop and the roughness from the damping of the thickness fringes and rate of intensity decrease with angle. These are not affected by the crystalline nature of the film. XRR patterns for monolithic (single layer) films can be directly analyzed without invoking tedious fitting analysis. However for if higher accuracy is expected for thickness, density, and roughness of thin film samples

fitting of the experimental reflectivity patterns to simulated once is needed. Generally Parratt fitting analysis is used for analyzing the thin film reflectivity patterns [5, 7].

(b) Experimental Results

The XRR measurements have been carried out on as deposited (1) IBS 190 12min (2) IBS 190 24min (3) IBS 190 36min samples using a D8 Discover diffractometer equipped with a grazing incidence attachment. The schematic of the experimental set up used for above measurements is shown in figure 3.2.1. The diffractometer comprises of a sealed X-ray tube (B) with a Cu anode. The maximum rated power of this tube is 3 kW. The divergence of the incident beam is limited in the vertical direction (dispersing direction) by a 50 μm slit termed as the 'divergence slit' (S1). A Soller slit is used to collimate the incident beam in the horizontal direction. The goniometer is of a vertical type and consists of two concentric circles for sample (θ) and detector (2θ) rotation. The sample stage (P) is horizontal and rotates about a vertical axis that is normal to the sample surface passing through its center. A razor blade edge (um slit) is placed very close to sample surface at the axis of rotation to generate a slit of the size of few microns [8]. The slit together with the divergence slit acts as a collimator resulting in a low incident beam divergence and is 0.02^0 for the above set up. This also reduces the sampling area of the beam. The exit beam path comprises of a 100 mm long soller slit arm (S2) which has a divergence of 0.4^o, a flat LIF (100) mono chromator (M) set to reflect Cu-K_α radiation (λ = 1.542 A^0) and a Nal (T1) scintillation detector (D) for counting the numbers of photons per unit time in the scattered radiation. The measurement in the present case has been carried out at a power of 1.2 kW (40 kV, 30mA), a limit set for a longer life of the x-ray tube. The instrumental resolution in θ is

0.02^{o} ($0.003\ A^{o-1}$ in the wave vector transfer). θ-2θ motions are mechanically de-coupled which facilitates independent motions of the sample and the detector.

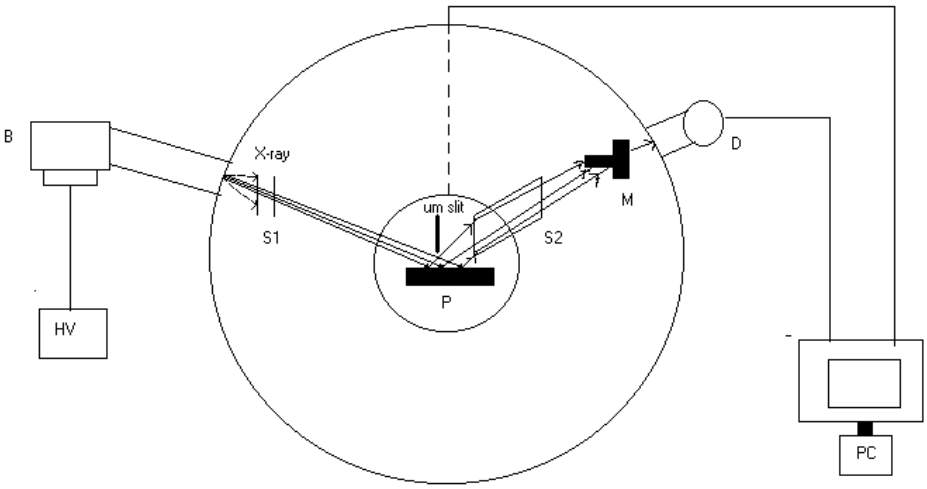

Fig. 3.2.1: Schematic diagram of the D8 Discover diffractometer.

The reflected intensity patterns obtained by XRR measurements were fitted using software based on the formalism developed by Parratt [5]. The surface roughness of the substrate (~ 0.8nm) before depositing the films has been measured and used as input parameter for fitting the reflectivity patterns. The thickness values obtained by fitting the X ray reflectivity patterns are 27, 53 and 80 nm (± 2nm) for IBS 190 12min, IBS 190 24min and IBS 190 36min samples respectively. An oxide layer of average thickness ~ 2nm was obtained as one of the fitted parameter too. Representative intensity pattern obtained by X-ray reflectivity measurements along with fitted curve for IBS 190 36min is depicted in figure 3.2.2. Thickness values of the thin film samples produced by the ion beam sputtering on the silicon substrate are depicted in table 3.2.1. Films were sputtered using the target

made by amorphous ribbons of nominal composition $Fe_{84}Nb_{3.5}Zr_{3.5}B_8Cu_1$ as described earlier in this chapter.

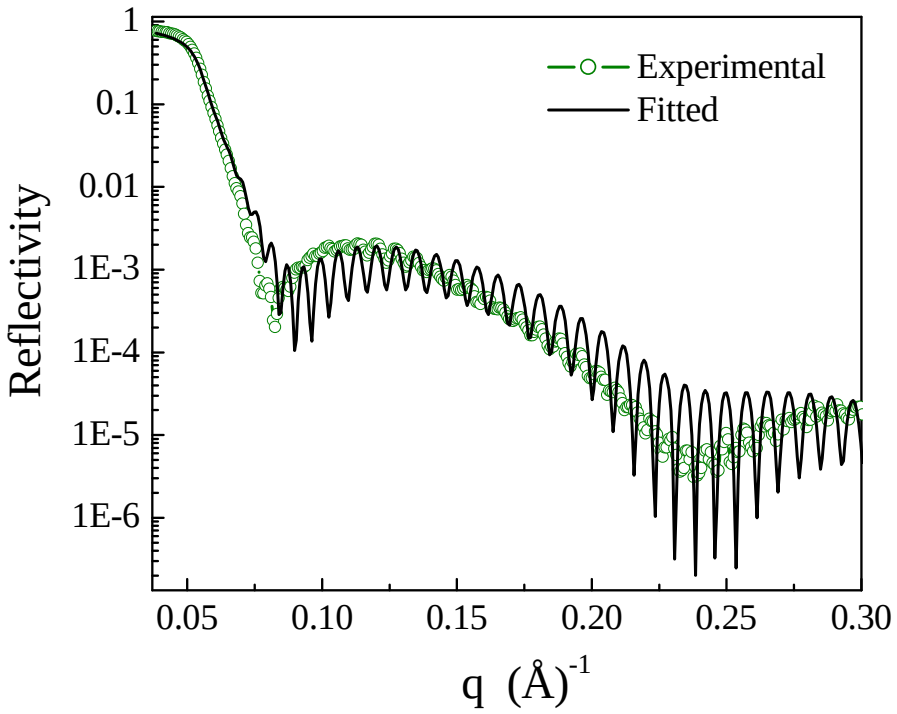

Figure 3.2.2: Representative X-ray reflectivity pattern of IBS190 36min sample in as deposited state.

Table 3.2.1: Thickness of ion beam sputtered thin film samples determined by XRR.

IBS Sample	Thickness (±2nm)
IBS190 12min	27nm
IBS190 24min	53nm
IBS190 36min	80nm

3.2.2: Grazing incidence XRD measurements

(a) Introduction

X-rays are not intrinsically a surface-selective probe. Nowadays very intense sources of X-rays are available so it is sometimes possible to obtain surface information simply by observing the deviations from the ideal bulk scattering, and attributing these deviations to the surface. This is done primarily when the bulk is a good single crystal, because then the scattering from it is largely limited to Bragg peaks. The excess scattering between Bragg peaks can then be attributed to a reconstructed surface or an adsorbed monolayer. This method has been used extensively in the study of surfaces of inorganic single crystals, and of mono layers and thin films deposited on these crystals [9-12]. Its disadvantages are that the substrate must be a good single crystal with little scattering between Bragg peaks, and the truncation rod profiles must generally be fitted using assumed models in order to extract information, as in the case of reflectivity. When the substrate is thin enough to be largely transparent to X-rays, as in the case of thinly-cleaved mica [13], or when there is a sample without a substrate, as in the case of freestanding liquid-crystal films [14], it is possible to look at the lateral structure by going right through the sample. This geometry is rarely used, because very few substrates are sufficiently transparent to X-rays. Hence it is sometimes very difficult to analyze thin films due to their small diffracting volumes, which result in low diffracted intensities compared to the substrate and background. This combination of low diffracted signal and high background makes it very difficult even to identify the phases present. The grazing incidence geometry (Figure 3.2.3) is surface selective, i.e. it largely avoids scattering from the substrate, and does not even require a transparent substrate. Grazing incidence angle arrangement combined with parallel beam geometry is

most commonly used technique for analyzing thin films. By increasing the path length of the incident X-ray beam through the film, the intensity from the film can be increased so that conventional phase identification analysis can be run. Figure 3.2.3 compares the grazing incidence angle geometry used for thin film with the more common $\theta / 2\theta$ geometry used for bulk analysis. In the conventional θ-2θ geometry, a para focusing arrangement is used where the X-ray source and the detector slit are at the focal points of the incident and diffracted beams, respectively. For the thin film arrangement, on the other hand, the incident and diffracted beams are made nearly parallel by means of a narrow slit on the incident beam and along soller slit on the detector side. In addition, the stationary incident beam makes a very small angle with the sample surface (typically 1^o to 3^o or even as small as 0.05^o depending upon the substrate electron density and the energy of X-ray beam.), which increases the path length of the X-ray beam through the film. This helps to increase the diffracted intensity, while at the same time, reduces the diffracted intensity from the substrate. Overall, there is a dramatic increase in the film signal to the background ratio. Since the path length increases when the grazing incidence angle is used, the diffracting volume increases proportionally. This is the reason for the increased signal strength. During the collection of the diffraction spectrum, only the detector rotates thus keeping the incident angle, the beam path length, and the irradiated area constant. The long Soller slit on the receiving side allows only those beams that are nearly parallel to arrive at the detector. This has an added advantage of reducing sensitivity to sample displacement from the rotation axis. For films in the range of 100 Å to 2000Å, grazing incidence analyses should preferably be used. The lower detection limit is also strongly dependent on the film chemistry so under optimal conditions there are some limitations to the method.

For example one gets better results if the surface is very smooth. On the other hand very small grazing incidence angle most of the incoming X-ray beam is wasted so one needs a compact and highly collimated beam. Also, if the film has a high degree of preferred orientation (such as an epitaxial film), the method is not very effective.

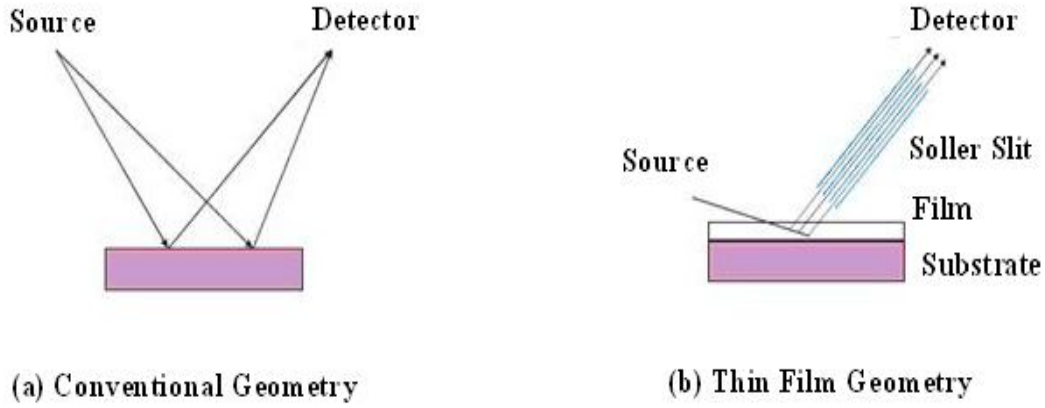

Figure 3.2.3 Geometries for a) Bulk analysis and b) thin film analysis showing the difference in the beam path lengths

(b) Experimental Results

X-ray diffraction measurements on as-deposited and thermally annealed samples were performed with Co-K_α radiation using X-pert diffractometer apparatus. Both set of thin film samples produced by ion beam and RF sputtering were X-ray amorphous in as deposited state. Figure 3.2.4 depicts the X-ray diffraction patterns of representative as deposited samples prepared by RF sputtering which clearly shows the amorphous nature of samples. Figure 3.2.5 shows the representative diffraction patterns of annealed samples that were produced by ion beam sputtering as described in the earlier section of this chapter. It may be noted that the signal strength is not as good as that was observed in case of bulk

Table 3.2.2: Annealing temperature dependence of grain size of representative IBS thin film samples.

Sample	Annealing Temp. (^{o}C)	Peak Position (degree)	FWHM (degree)	Grain size (nm)
IBS 190 36 min	550°C	52.1400	0.8130	12.6± 0.5
IBS 190 36 min	450°C	51.7800	0.8530	12.0± 0.5
IBS 190 36 min	400°C	51.8100	0.9575	10.7± 1
IBS 190 36 min	350°C	51.7200	0.7470	13.7± 2
IBS 190 24 min	550°C	52.0500	0.8760	11.7± 2
IBS 190 12 min	550°C	52.0400	0.7600	13.5± 2

composition (see figure 2.3.3). The diffraction patterns were fitted using pseudo voigt line profile in order to obtain the grain size by applying Sherrer analysis [15].Results are summarized in Table 3.2.2. It may be seen that apparently the grain size of nanocrystallites is independent of the thickness and the annealing treatment.

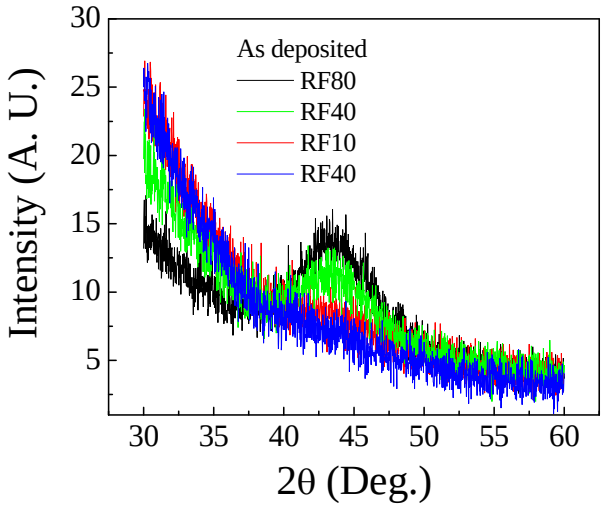

Figure 3.2.4: Representative X-ray diffraction patterns of as deposited RF sputtered thin film samples.

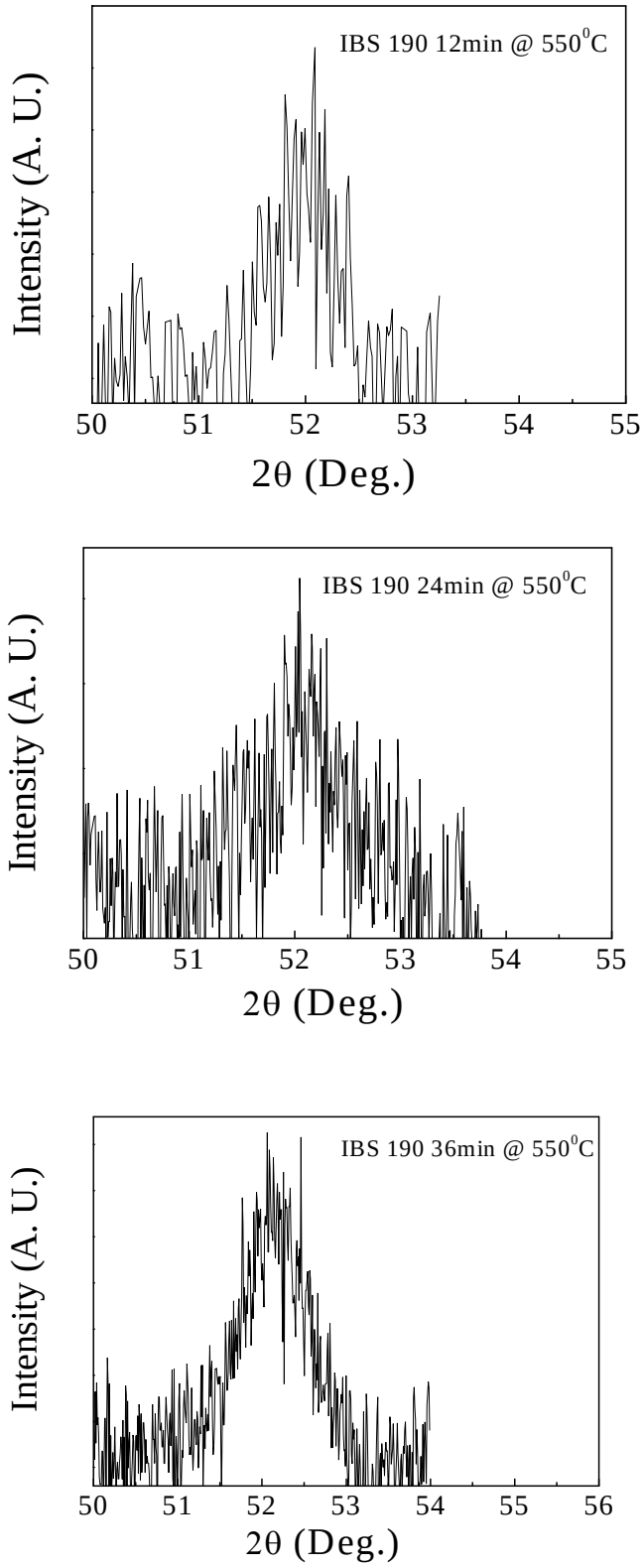

Figure 3.2.5: Representative X-ray diffraction patterns of annealed IBS thin film samples.

3.3 Atomic force microscopy images

3.3.1: Introduction

Several techniques are available for magnifying the microscopic features of a surface. Methods for magnifying surface features originated with magnifying lenses and optical microscopy in the late 18^{th} century. Optical instruments are limited by wavelength of visible light and can resolve objects down to approximately 0.5 microns. During the 20^{th} century, methods for magnification based on electron and ion beams were developed. Operating in vacuum the scanning electron microscope (SEM) can resolve features to the level of approximately 30Å if the specimen's atomic number contrast is high. SEM microscopy often has destructive effects on the sample and it also do not readily yield depth information. Scanning probe microscopy (SPM) is a recent, innovative technology that relies on a mechanical probe for generation of magnified images. A SPM instrument is operable in air, liquid or vacuum and it resolves features in three dimensions down to a fraction of an angstrom. SPM technique resolves a magnified image using data obtained by scanning the sample surface with a sharp, microscopic mechanical probe. Magnification of the vertical surface features of an object, those leaving the horizontal plane and extending in the vertical direction, have historically been measured by a stylus profiler [16]. In 1971 Russell Young [17] demonstrated a non-contact type of stylus profiler. In his profiler Young used the fact that the electron field emission current between a sharp metal probe and a surface is dependent on the probe sample distance for electrically conductive samples. In 1981 researchers at IBM were able to utilize the methods first demonstrated by Young to create the scanning tunneling microscope (STM). Binnig and Rohrer [18]

demonstrated that by controlling the vibrations of an instrument very similar to Young's profiler, it was possible to monitor the electron tunneling current between a sharp probe and a sample. Since electron tunneling is much more sensitive than field emissions, the probe could be used to scan very close to the surface. They were able to see individual silicon atoms on a surface. Although the STM was considered a fundamental advancement for scientific research, it had limited applications, because it worked only on electrically conductive samples. The first Atomic Force Microscope (AFM) was made by meticulously gluing a tiny shard of diamond onto one end of a tiny strip of gold foil. A major advancement in profilers occurred in 1986 when Gerd Binnig, Christoph Gerber and Quate used this cantilever to examine insulating surfaces in order to demonstrate the first ever AFM [19]. A small hook at the end of the cantilever was pressed against the surface while the sample was scanned beneath the tip. The force between tip and sample was measured by tracking the deflection of the cantilever. This was done by monitoring the tunneling current to a second tip positioned above the cantilever. They could delineate lateral features as small as 300 Å. The force microscope emerged in this way. In fact, without the breakthrough in tip manufacture, the AFM probably would have remained a curiosity in many research groups. It was Albrecht, a fresh graduate student, who fabricated the first silicon micro-cantilever and measured the atomic structure of boron nitride [20]. Figure 3.3.1 shows the basic schematic of a typical AFM that uses an optical beam that gets reflected from the mirrored surface on the back side of the cantilever onto a position-sensitive photo-detector. As the tip scans the surface of the sample, moving up and down with the contour of the surface, the laser beam is deflected off the attached cantilever into a dual element photodiode. The photo-detector measures the difference in light intensities

between the upper and lower photo-detectors, and then converts to voltage. Feedback from the photodiode difference signal, through software control from the computer, enables the tip to maintain either a constant force or constant height above the sample. Even a small deflection of the cantilever tilts the reflected beam and thus the position of beam on the photo-detector changes.

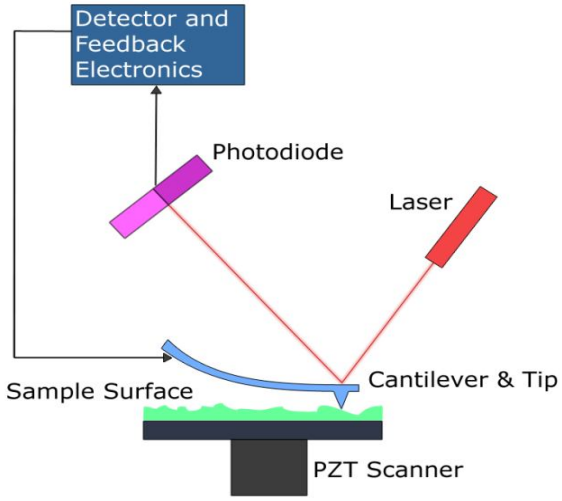

Figure 3.3.1: Schematic of an atomic force microscope

According to the interaction of the tip and the sample surface AFM can be used in two basic modes (1) Contact mode: The contact mode, where the tip scans the sample in close contact with the surface, is the common mode used in the force microscope. The force on the tip is repulsive with a mean value of 10^{-9} N. This force is set by pushing the cantilever against the sample surface with a piezoelectric positioning element. In contact mode AFM the deflection of the cantilever is sensed and compared in a DC feedback amplifier to some desired value of deflection. Problems with contact mode are caused by excessive tracking

forces applied by the probe to the sample. In contact AFM electrostatic and/or surface tension forces from the adsorbed gas layer pull the scanning tip toward the surface. It can damage samples and distort image data. Therefore, contact mode imaging is heavily influenced by frictional and adhesive forces. (2) Non-contact mode: It is used in situations where tip contact might alter the sample in subtle ways. In this mode the tip hovers 50 - 150 Angstrom above the sample surface. Attractive Van-der Waals forces acting between the tip and the sample are detected, and topographic images are constructed by scanning the tip above the surface. AFM offers some practical advantages over its precursors (e.g. STM, SEM, TEM and optical microscopes) as it can be used to analyze both conducting and insulating sample surfaces. AFM also doesn't requires expensive sample preparation (no coating is necessary) as it provides extraordinary topographic contrast direct height measurements and unobscured views of surface features independent of reflectivity differences between materials. AFM offers the advantage that the writing voltage and tip-to-substrate spacing can be controlled independently, whereas with STM the two parameters are integrally linked.

3.3.2: AFM images of as deposited and annealed thin film samples

AFM images of annealed IBS samples were taken using standard AFM apparatus by digital instruments Figure 3.3.2 a, b and c shows the AFM images of the as deposited and annealed ion beam sputtered samples. In figure 3.3.3 variation of average surface roughness with annealing temperature is presented. With the increasing annealing temperature the tendency for the formation of aggregates on the surface increases. This might be due to the

tendency of minimizing the surface energy by increasing the surface area locally. Nanocrystallites are not growing in size considerably with annealing temperature as also is seen through the X-ray diffraction measurements. The change in the surface profile is considerably affected by the extent to which the sample is crystallized. Surface topography also seems to be affected by the thickness as the variation of average roughness with annealing temperature suggests that the thickest sample shows comparatively lower value of surface roughness even after being annealed at higher temperature. Although it may be noted that the amorphous ribbon composition used as target contains Zr and it has a high tendency of getting oxidized. Thus the surface topography is not necessarily represents the effect of crystallization, it may be possible that the oxidation of surface is leading to the overestimation of the dimensions of the surface aggregates which may not correspond at all to the size of nanocrystallites appearing as a result of annealing treatment.

As deposited

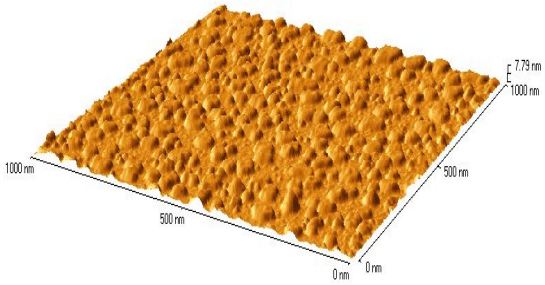

350^0C / 80 min.

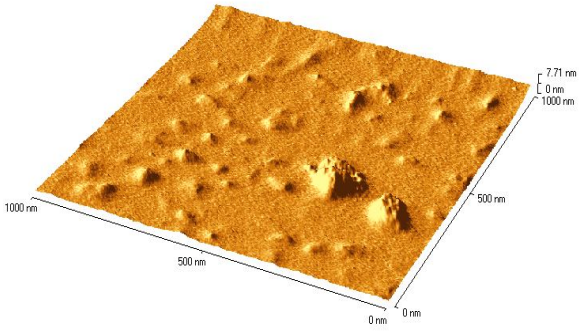

400^0C / 80 min.

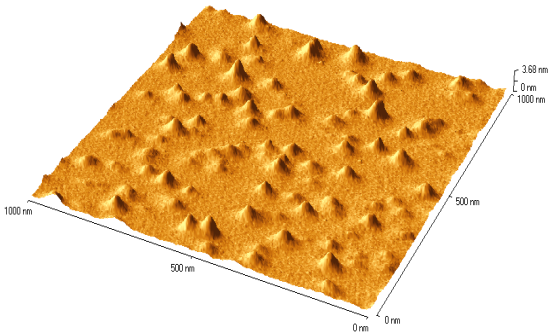

450^0C / 80 min.

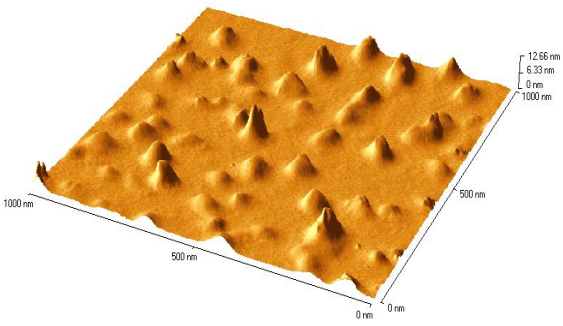

500^0C / 80 min.

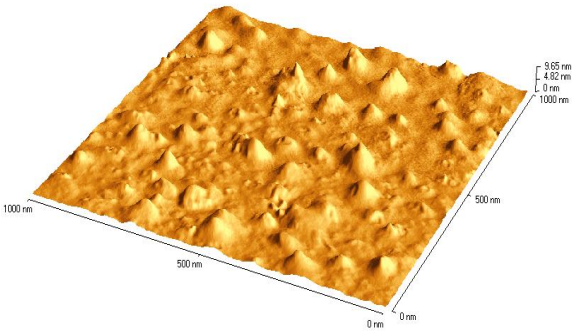

Figure 3.3.2 (a) AFM images of the IBS 190 12 min samples in as deposited state and after annealing at various temperatures for 80 minutes.

As deposited

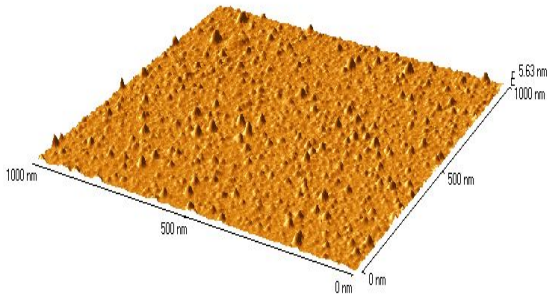

350^0C / 80 min.

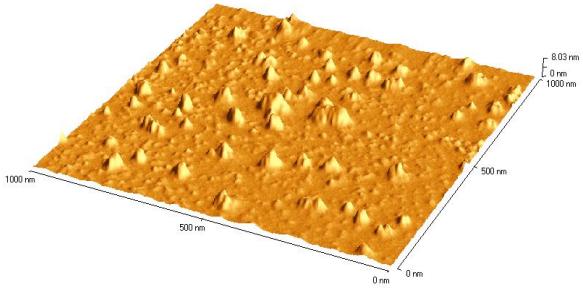

400^0C / 80 min.

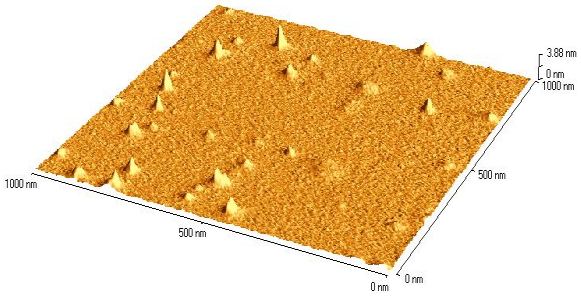

450^0C / 80min.

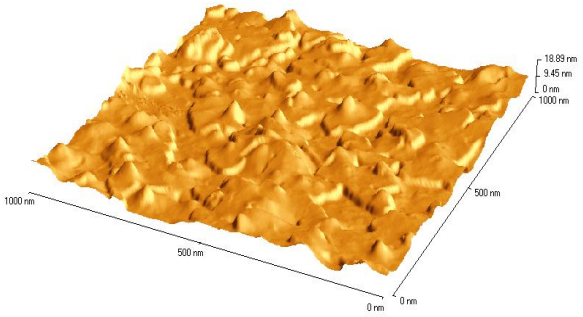

500^0C / 80 min.

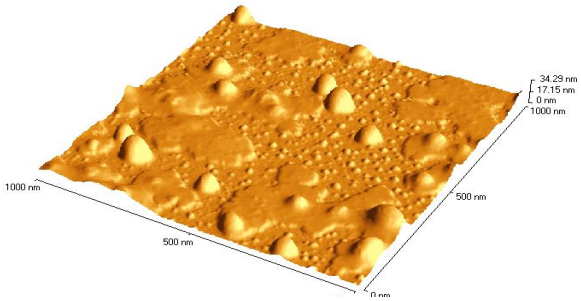

Figure 3.3.2 (b) AFM images of the IBS 190 24 min samples in as deposited state and after annealing at various temperatures for 80 minutes.

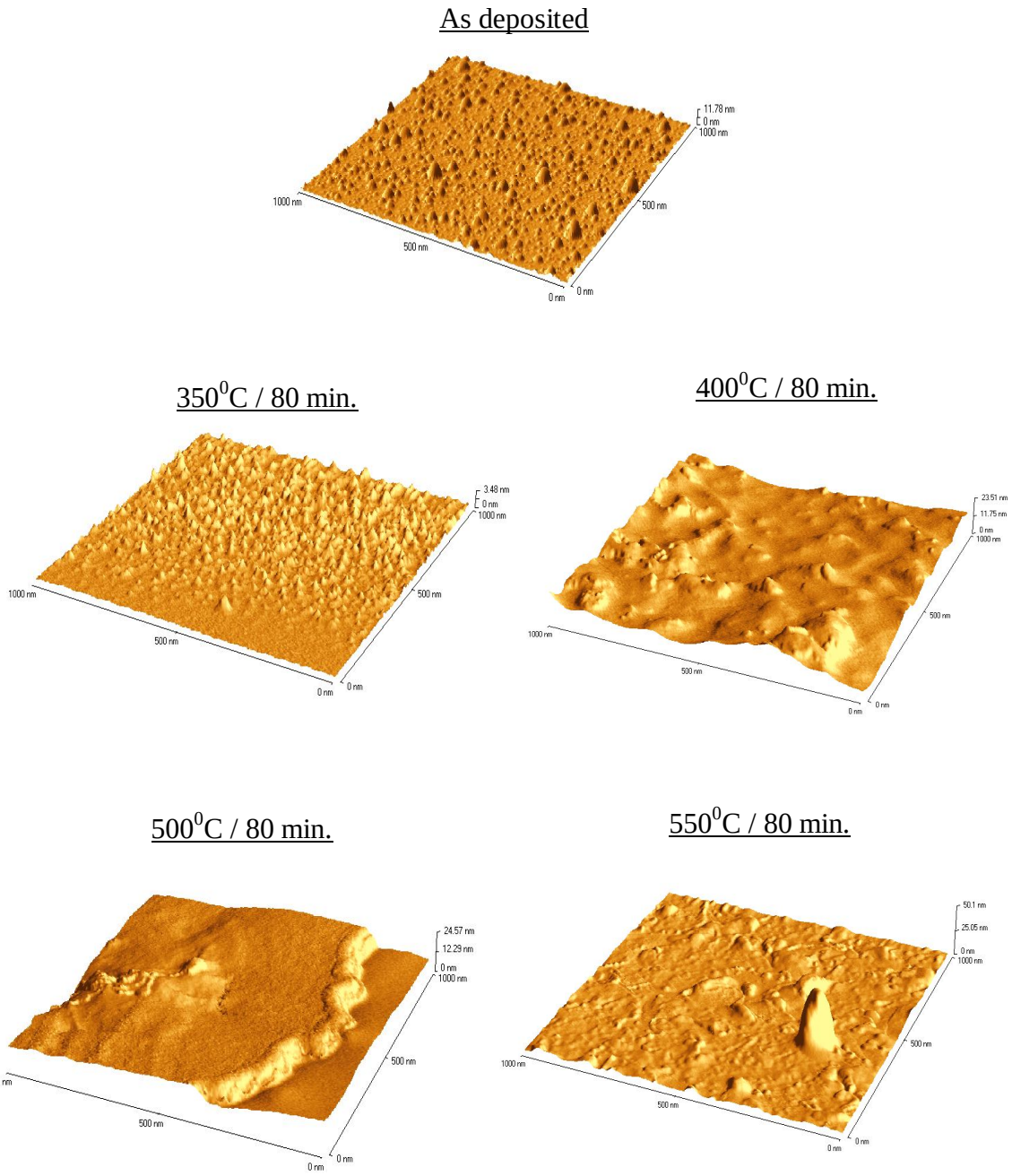

Figure 3.3.2 (c) AFM images of the IBS 190 24 min samples in as deposited state and after annealing at various temperatures for 80 minutes.

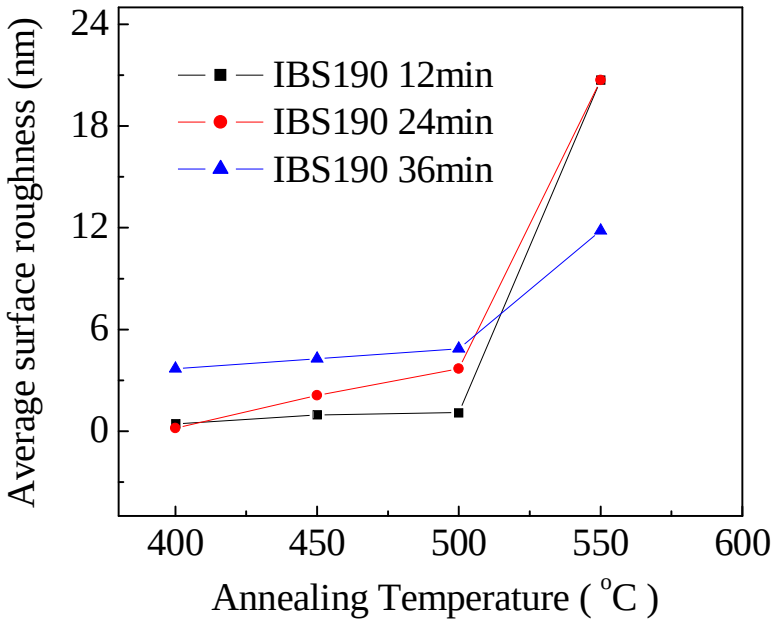

Figure 3.3.3: Annealing temperature dependence of average surface roughness.

Figures 3.3.4 a, b shows representative AFM images, of as deposited thin films samples prepared by RF sputtering, depicting the surface topography (Top and middle panel) and MFM images (lower panel). First slide (a) in the figure 3.3.4 shows the image corresponding to the scanning area of 5 μm × 5 μm and for the image shown in the slide (b) the area of 1000nm × 1000nm was scanned. It seems that all the as deposited samples are crystalline at least at the surface. But as already confirmed by X-ray diffraction measurements that the as deposited samples are amorphous, it may be inferred that the as deposited samples are not fully amorphous but some crystallite like structures are visibly present on the surface of samples. Tendency to form clusters is observed in all the film samples. Some aggregates seem to be exceptionally big, and appear to be in a direction

perpendicular to the film plane but these can also be some artefacts appearing due to some possible presence of dust particles.

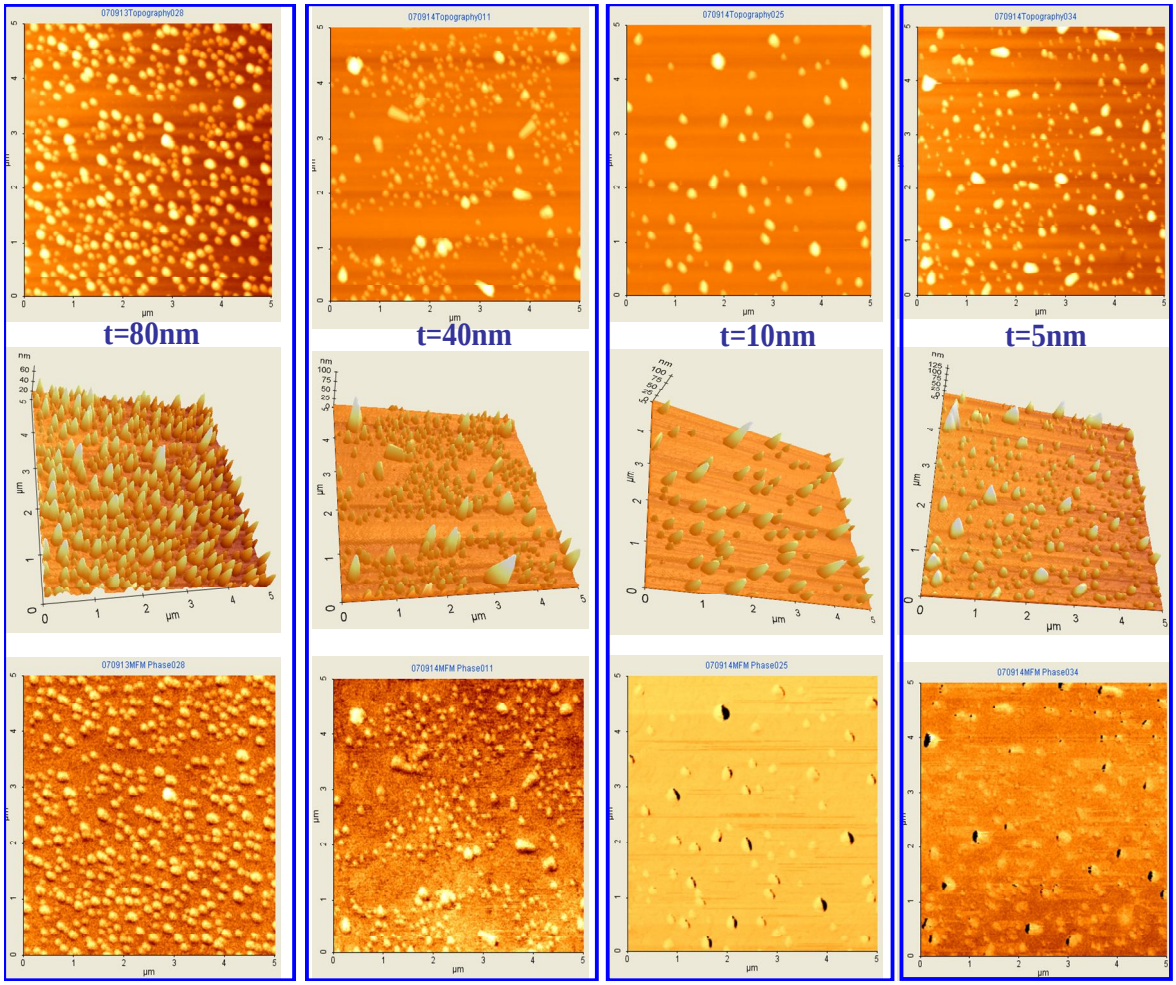

Figure 3.3.4 (a): Forced microscopy images of representative as deposited RF samples with the scanning area of 5 µm × 5 µm.

MFM images do not show a clear contrast because it is sensitive to the perpendicular component of magnetization. It seems that largely the magnetization is lying in the film plane for the samples under investigation. MFM measurements may denote the presence of Bloch walls present if any. But in the case of our thin film samples it seems that shape anisotropy might have induced the formation of Neel walls and magnetization preferably remain in plane of the thin film samples.

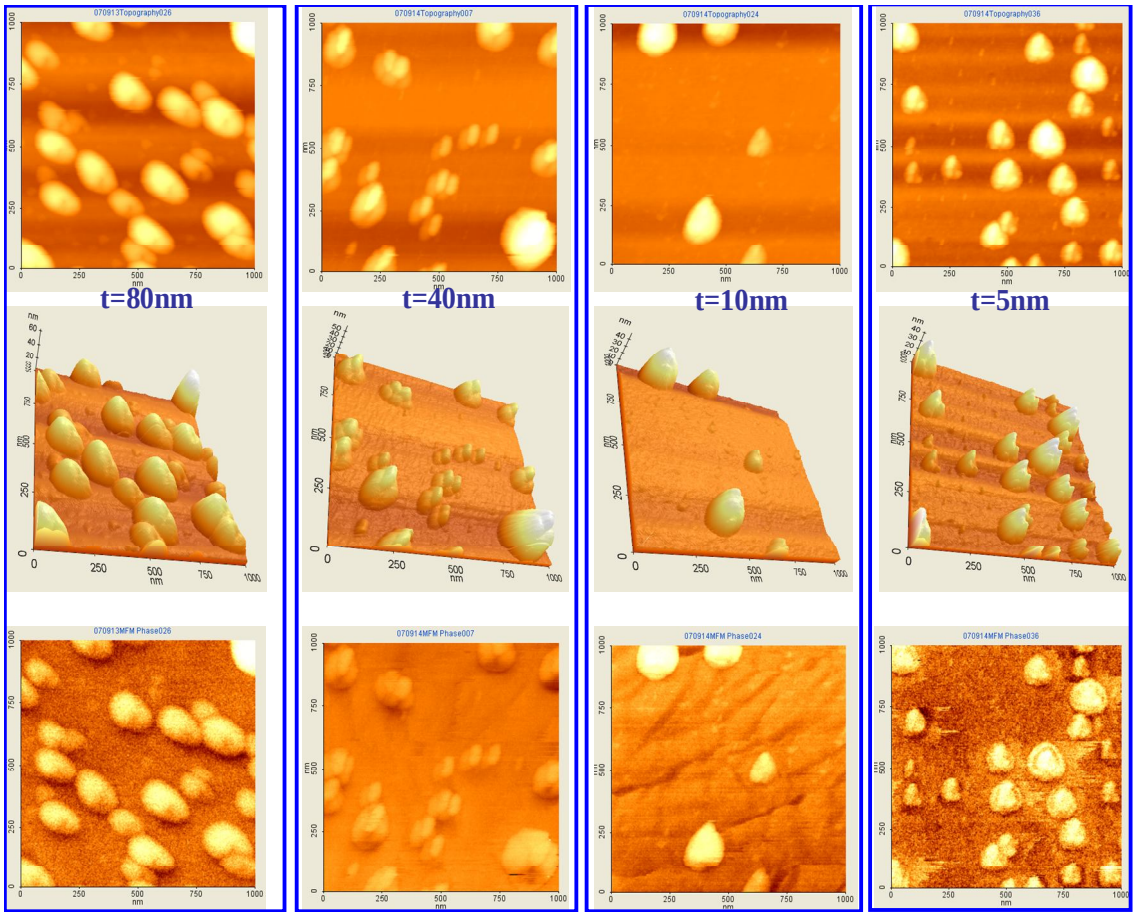

Figure 3.3.4 (b): Forced microscopy images of representative as deposited RF samples with the scanning area of 1000nm × 1000nm.

References:

[1] Handbook of plasma processing technology edited by S. M. Rossnagel, J.Cumuo, W. Westwood, William Andrew publishing/ Noyes Publications (1990).

[2] Thin film processes edited by John L. Vossen and Werner Kern Academic press (1979).

[3] W. R. Grove, "On the electrochemical polarity of gases", Phil. Trans. Royal. Soc. London, B142 (1852) 87.

[4] L. Maissel, Handbook of Thin Film Technology, Chapter 4, McGraw Hill, New York, 1970.

[5] L. G. Parratt, Phys. Rev. 95 (1954) 359.

[6] S. K. Sinha, E. B. Sirota, S. Garoff, H. B. Stanley, Phys. Rev. B38 (1988) 2297.

[7] A. Gibaud, S. Hazra, Current Science, Vol. 78, No.12 (2000) 1467.

[8] B. L. Henke, J. Y. Uejio, H. T. Yamoda, R. E. Tackaberry, Opt. Engg. 25 (1986) 937.

[9] P. Dutta, Current Science, Vol. 78, NO. 12 (2000) 1482

[10] I. K. Robinson, and D. J. Tweet, Rep. Prog. Phys. 55 (1992) 599.

[11] I. Robinson, P. Eng, and E. Schuster, Acta Phys. Pol. A86 (1994) 513.

[12] Robinson, I. K., Acta Crystallo. 54 (1998) 772.

[13] M. Prakash, P. Dutta, J. B. Kettersonand, B. M. Abraham, Chem. Phys. Lett. 111, (1984) 395.

[14] E. I. Demikhov, V. K. Dolganov, and K. P. Meletov, Phys.Rev. E 52 (1995) 1285.

[15] P. Sherrer, Math. Phys. K1.2 (1918) 96.

[16] Gustev Shmalz, Uber Glatte und Ebenheit als physikalisches und physiologishes Problem, Verein Deutscher Ingenieure,(1929) 1461.

[17] R. Young, J. Ward, F. Scire, The Topografiner: An Instrument for Measuring Surface Microtopography, Rev. Sci. Inst., Vol 43, No 7, (1971) 999.

[18] G. Binnig, H. Rohrer, Ch. Gerber, E. Weibel, Surface Studies by Scanning Tunneling Microscopy, Vol. 49, No. 1, (1982) 57.

[19] G. Binnig, C.F. Quate, Ch. Geber, Atomic Force Microscope, Phys. Rev. Letters, Vol. 56, No 9, (1986) 930.

[20] Albrecht, T. R., Quate, C. F., J. Vac. Sci. Technol. A 6(2) (1988) 271.

CHAPTER 4

Investigation of magnetic properties of amorphous and nanocrystalline FeZrNbBCu ribbons

This chapter reports the effect of annealing on the magnetic properties of as cast and nanocrystallized ribbons of nominal composition $Fe_{84}Zr_{3.5}Nb_{3.5}B_8Cu_1$. Ribbons were crystallized by thermal annealing in an inert atmosphere. Magnetic measurements were carried out at room temperature using the standard methods. Dependence of magnetic properties on various micro structural parameters is presented. Information and results obtained by room temperature Giant magneto impedance measurements are also included in order to understand the effect of soft magnetic properties on the magneto transport behaviour of the alloy under investigation. Anisotropy field distribution is determined using an experimental method based on second harmonic response of magnetization. Studies have been carried out in order to better understand the various mechanisms involved that determine the soft magnetic behaviour of this alloy system. Possible limits of applicability of random anisotropy mechanism for soft magnetic nanocrystalline material are also discussed by presenting a grain size and volume fraction dependence of coercive field based on the domain wall pinning.

- ***Determination of soft magnetic properties***
- ***Determination of anisotropy field distribution***
- ***Giant magneto-impedance measurements***
- ***Departure from random anisotropy mechanism***
- ***References***

4.1 Determination of soft magnetic properties

4.1.1 Introduction

There has been demand of a soft magnetic material with high saturation magnetization as well as good soft magnetic properties such as high permeability and low coercivity in order to improve the operational characteristics of electromagnetic devices. Suppression of the effective anisotropy and a lower value of magnetostriction constant are necessary for soft magnetic properties. This can be achieved by employing a proper choice of annealing conditions besides the composition of alloy which also plays an important role. The Fe-rich amorphous and nanocrystalline alloys has been investigated extensively for long from an expectation of high saturation magnetization values. It has been reported that soft magnetic properties of Fe-Si-B amorphous alloys are improved by the formation of mixed structure consisting of amorphous and fine bcc precipitates caused by partial crystallization [1]. Subsequently very good soft magnetic properties were reported for a mostly single bcc phase (FINEMET), with grain size ~ 10nm, obtained by partial crystallization of Fe-Si-B-Nb-Cu amorphous alloys [2]. Fine grains were obtained as a result of interplay between the nucleating and inhibiting elements like Cu and Nb respectively. In FINEMET type of alloys Fe-Si grains are surrounded by an amorphous phase enriched in B and Nb which have high recrystallization temperatures [3, 4]. FINEMET family of alloys exhibit relatively poor mechanical properties because of brittleness. Thermal stability of this family of alloy is also poor as Fe_3B and other grains get recrystallized at higher temperature. It has been interpreted [5-7] that the soft magnetic properties of these nanocrystalline alloys are due to the decrease in apparent anisotropy which is a result of refinement of grain size. Accordingly grain size refinement of iron rich amorphous alloy by crystallization seem to

be very effective in achieving good soft magnetic properties with the high magnetization values. Fe-P-C-Ge-Cu alloys reportedly produced by annealing the melt spun amorphous ribbons are also known to exhibit high permeability [8]. However the saturation flux density values of above discussed family of alloys are substantially lower (~ 1.3 Tesla) than that of conventional Fe based amorphous alloys. The reason being the composition of alloys that are typically based on metal- metalloid amorphous alloys e.g. Fe-Si-B or Fe-P-C along with the other non magnetic additives such as Cu, Nb or Ge etc. Whereas Cu free Fe-M-B (M= Zr, Nb, Hf) alloys nanocrystallized from amorphous state exhibits high saturation magnetization (~ 1.6-1.7 tesla) and high permeability simultaneously. Effective permeability for this family of alloys at 1 kHz is as high as about 30000 [9-12]. The saturation magnetization of these alloys is high due to less concentration of metalloid comparatively. Fe-Zr-B-Cu based NANOPERM family of alloys are characterized by high saturation magnetization and high permeability representing one of the best soft magnetic nanocrystalline material when they are compared on the basis of relative permeability versus saturation induction plot [10-13]. It has been shown that the bcc grain size can be further reduced by a small addition of Cu leading to a further enhancement of permeability [10, 11]. The magnetostriction of Fe-Nb-B and Fe-Nb-B-Cu alloys is positive whereas that of Fe-Zr-B and Fe-Zr-B-Cu alloys is negative around the optimum composition for achieving soft magnetic properties. Reduction of magnetostriction is expected to improve the soft magnetic properties of nanocrystalline alloys further. Attempts have been made to obtain almost zero magnetostrictive alloys by a combined addition of Nb and Zr supported by a controlled addition of B [14, 15]. With only Zr NANOPERM alloys can not be cast in air but addition of Nb enables the casting of alloys in air by applying some Ar jet around

the wheel during the process of melt spinning. Thus apart from reducing the magnetostriction, Nb also makes the alloy preparation relatively easier and cost effective.

4.1.2: Effect of annealing on the soft magnetic properties of $Fe_{84}Zr_{3.5}Nb_{3.5}B_8Cu_1$ ribbons

A computer controlled quasi static hysteresis loop tracer (see appendix A) was used to measure the hysteresis loop of the as cast and thermally annealed $Fe_{84}Zr_{3.5}Nb_{3.5}B_8Cu_1$ ribbons of 7cm length at room temperature in order to determine the coercive field and saturation magnetization. Table 4.1.1 summarizes the annealing temperature dependence of experimentally obtained values of various micro structural parameters and the magnetic properties of ribbon samples. It should be noted that grain size and volume fraction of nanocrystallites increases with annealing temperature. As the volume fraction of crystalline phase increases with annealing temperature, the distance between the nano grains decreases. Volume fraction is defined normally as:

$$V_x = D^3 / (D+ d)^3$$

Where D is the average grain size and d is the average distance between the nanocrystallites. There exists a critical value of the volume fraction that affects the coercivity behaviour. This limiting value of crystalline volume fraction corresponds to the situation when inter granular distance becomes equal to the basic ferromagnetic exchange length (l_{ex}). This results into increased exchange coupling among nanocrystallites. Thus for the limit $d \sim l_{ex}$ the limiting value of V_x comes out to be ~ 5%. In other words this indicates the probable limit after which the coercive field is expected to decrease as a result of stronger exchange coupling that averages out the random anisotropies. Whereas from table 4.1.1 it can be seen that upto V_x ~ 23% the coercive field increases and for higher

crystalline fraction the coercive field decreases. Thus it may be interpreted that the coercive field does not necessarily being governed by the effective exchange coupling which is expected to increase with annealing temperature.

Table 4.1.1: Annealing temperature dependence of structural parameters and coercive field for $Fe_{84}Zr_{3.5}Nb_{3.5}B_8Cu_1$ ribbons.

Annealing Time (in minutes)	**Annealing Temperature (^{O}C)**	V_x **(%) (±2)**	D **(nm) (±1)**	H_C **(A / m) (±1)**
60	470	15.9	7.4	14.7
10	480	16.2	7.6	11.2
60	480	19.5	8.3	15.7
10	490	20.1	8.4	14.4
20	490	21.4	8.7	12
40	490	22.8	9.1	12
60	490	23.2	9.2	18
60	500	27.8	9.4	11.2
60	510	31.2	9.5	13.5
60	520	36.4	9.6	7
60	530	48.6	10.2	5.9

Figure 4.1.1 shows the representative hysteresis loops measured on as cast and annealed samples. The effect of thermal treatment can be seen clearly in terms of the shape of the loops. The annealing temperature dependence of coercive field and saturation magnetization is represented in figure 4.1.2. Obtained moderate values of coercive field suggest that most of the boron is retained in the amorphous matrix and only a small amount of boron is present in the nanocrystalline phase. This is also supported by the XRD measurements as described earlier in chapter 2. It may be noted that the average grain size does not increase substantially after 490^{o}C. This is an indication that the composition of nanocrystalline phase remains independent of the annealing temperature and time for higher annealing temperature. Coercive field initially increases till 490^{o}C and for higher annealing temperature coercive field decreases. Initial increase in coercive field can be ascribed to the grain growth which might induce stresses, as the grain size and lattice parameter increases till 490^{o}C and stabilizes above. Decrease in the coercive field values at higher annealing temperature can be understood within the framework of increased exchange coupling resulted from the increasing volume fraction of nanocrystalline phase. Figure 4.1.3 a, b shows the variation of coercive field with grain size and volume fraction respectively. It should be noted that both grain size and volume fraction of nanocrystallites increases with annealing temperature whereas the coercive field shows decrement for higher annealing temperature. As described earlier in the chapter 1 according to the arguments of random anisotropy model suggested by Herzer [6, 7] coercive field follows sixth power of grain size dependence. Coercive field simultaneously varies as square of the volume fraction of nanograins i.e. apart from constants coercive field varies as:

$$H_c \sim V_x^2 D^6$$

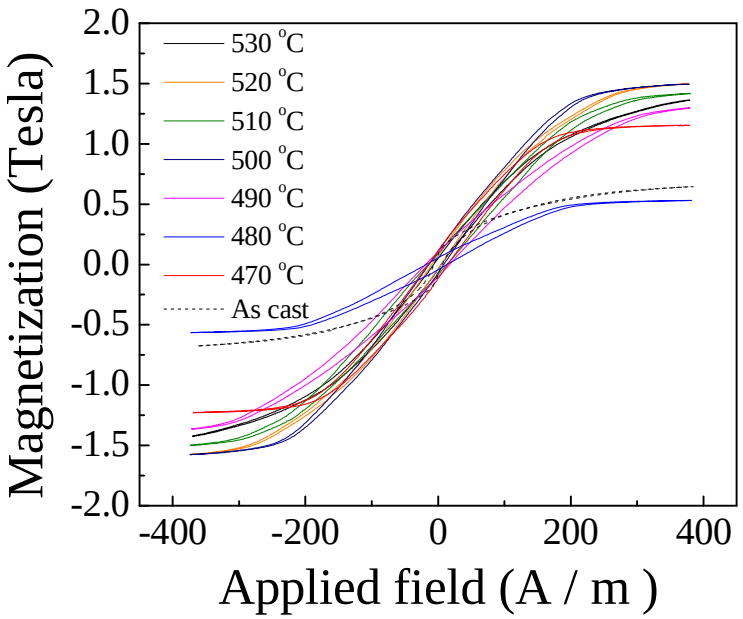

Figure 4.1.1: Representative hysteresis loops showing the effect of thermal annealing treatment carried out for 60 minutes at various temperatures shown.

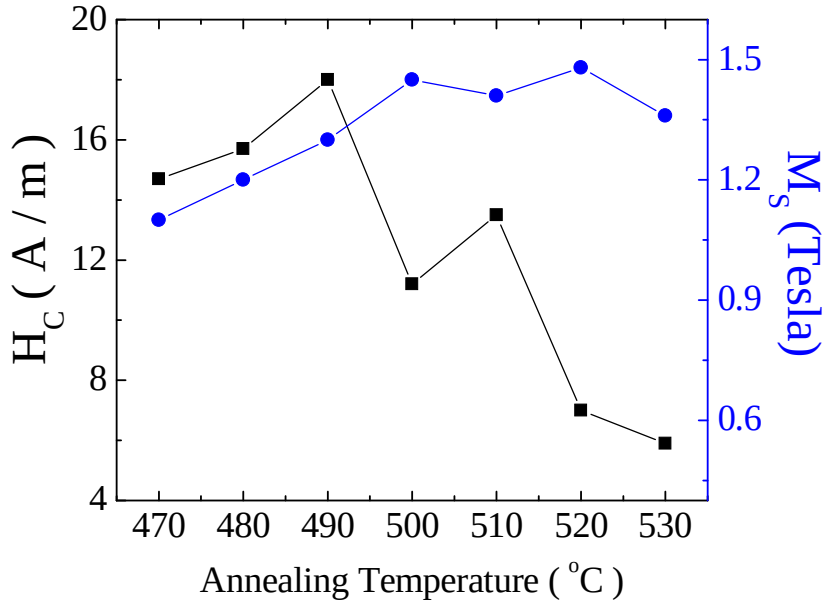

Figure 4.1.2: Annealing temperature dependence of coercive field and saturation magnetization for the samples annealed for 60 minutes at various temperatures.

The ratio of coercive field values (calculated using random anisotropy model) corresponding to the samples with lowest and highest value of crystalline fraction comes out to be ~ 64. This ratio obtained on the basis of experimental observations yields 0.33. Comparing these two ratios obtained on the basis of theory and experiments exhibit huge difference. This suggest that the application of random anisotropy model in our case is will not be helpful in understanding the coercive field behaviour. This also forbids us to interpret the status of the effective anisotropy energy of system determining the magnetization behaviour. As can be seen from the figure 4.1.3 a, b it is quite difficult to have a reasonable fit of this experimental data using a power law. It is however important to remark here that the coercive field has a stronger dependence on volume fraction of nanocrystals in comparison with the grain size dependence. We may say that the system is not following the random anisotropy mechanism as expected because coercive field is increasing first and then decreasing for higher annealing temperatures. This is accompanied by increasing grain size and volume fraction of nanocrystallites that suggests coercive field should increase with annealing temperature if system is following random anisotropy mechanism. So it may be interpreted that the magnetocrystalline anisotropies of nanocrystallites are getting lowered because inter granular phase facilitates the exchange coupling. The alloy under investigation is having very low magnetostrcitive properties and moreover the samples were pre annealed at 350^{o}C in order to get rid of some residual stresses generated during rapid quenching. In order to have a more clear idea about the effective anisotropy we carried out the experimental determination of anisotropy field distribution which will be discussed in the next section of this chapter. Also further in the section 4.4 of this chapter we have discussed a different grain size and volume fraction

dependence of coercive field on the basis of the structural and magnetic studies that were carried out by us on a Fe-Co based alloy in the form of ribbons.

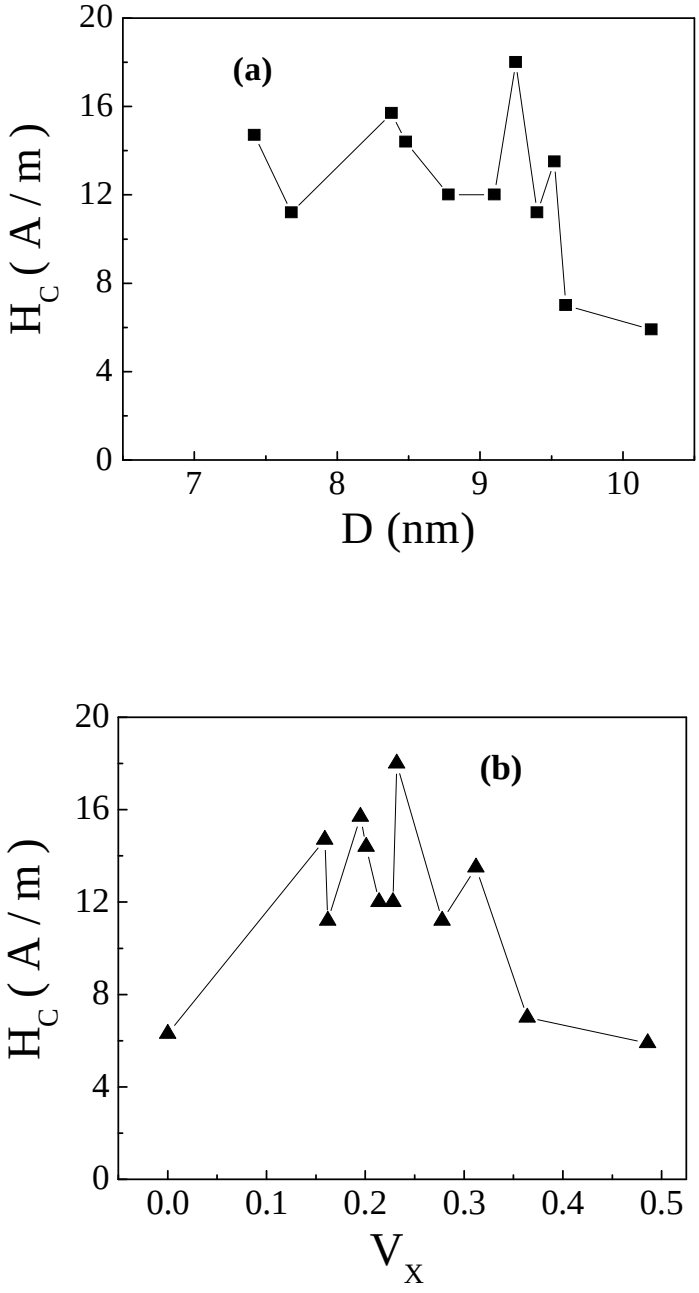

Figure 4.1.3: (a) Grain size and **(b)** Crystalline volume fraction dependence of coercive field for the studied $Fe_{84}Zr_{3.5}Nb_{3.5}B_8Cu_1$ alloy.

4.2 Determination of anisotropy field distribution

4.2.1 Experimental method

A quantitative measure of strength of the magnetic anisotropy is the field required to saturate the magnetization in hard direction which is otherwise not favoured energetically by the system left at its own [16]. Soft magnetic properties of amorphous and nanocrystalline magnetic materials is a result of balance between anisotropy energy, exchange energy and magneto static energy. Micro structural features like grain size, texture, defects, quenched in stresses etc. are important factors that dictate the mechanism whereby magnetization processes take place. The study of connection between soft magnetic property and micro structure is an important factor in understanding the development and applications of soft magnetic materials. In modern magnetic devices magnetic properties are to be tailored suitably in order to enhance the performance at industrial scale. Effective results can be obtained by fine tuning the micro structural aspects that affects magnetization process and govern the mechanisms that give rise to hysteresis and energy dissipation. For instance in power electronics applications special tailoring of hysteresis loop features is required which can be achieved by inducing magnetic anisotropy in a controlled way by means of performing annealing of amorphous alloys under stress or application of magnetic field [17-19]. In other circumstances some other type of anisotropies may be desirable. Understanding the strength and distribution of such anisotropies is required in order to improve the processes to obtain the desired anisotropy. The determination of anisotropy field and its distribution is easier in cases where the anisotropy energy is dominant i.e. a system in which a well defined anisotropy exists. In case of soft magnetic amorphous and nanocrystalline alloys where anisotropy varies

randomly over a length scale determined by the micro structural aspects, there exist a distribution of anisotropies and the anisotropy field determination is not straight forward. As the distribution of anisotropies determines the magnetization curve it is possible to determine the distribution of anisotropies from the magnetization curve. Distribution of anisotropy field can be determined by evaluating the second order derivative of the magnetization curve [20]. This evaluation is based on the assumption of the presence of the magnetic anisotropies which have an easy axis perpendicular to the applied field direction. In such a case the anisotropy energy constant (K) and the anisotropy field (H_k) are related by:

$$K = \frac{1}{2}\mu_o M_s H_k \qquad (4.2.1)$$

Where M_s being the spontaneous magnetization If anisotropy constant or anisotropy field are distributed with a probability P (H_k) then the distribution function is given by:

$$P(H_k) = (-H)\frac{d^2\langle m\rangle}{dH^2} \qquad (4.2.2)$$

Where m is the reduced magnetization ($M(H) / M_s$). Numerical calculation of the second derivative in eq. 4.2.2 ends up as a noisy procedure and several smoothing steps are to be introduced in order to get a reasonable distribution of anisotropy field. We have followed an experimental method [21] that is based on the second harmonic response of magnetization. This method gives the anisotropy field distribution with high resolution (see appendix B for details of theoretical formulations). Figure 4.2.1 presents the scheme of the experimental arrangement for determining the second harmonic component of

magnetization. The sample (S) is surrounded by a pick up coil connected in series with a compensating coil. Helmholtz coil set is used to produce the static magnetic field sourced by a DC power supply. Another solenoid (E), excited by function generator, is used to produce an AC field. A lock in amplifier was used that measures the voltage induced in the pick up coil taking a reference signal whose frequency is double than that of the signal used to generate the alternating field. The static magnetic field was also changed in small steps. An excitation frequency of 10 kHz was employed as decided by number of tests as higher frequency produces strong signal but also cause disturbances due to eddy currents.

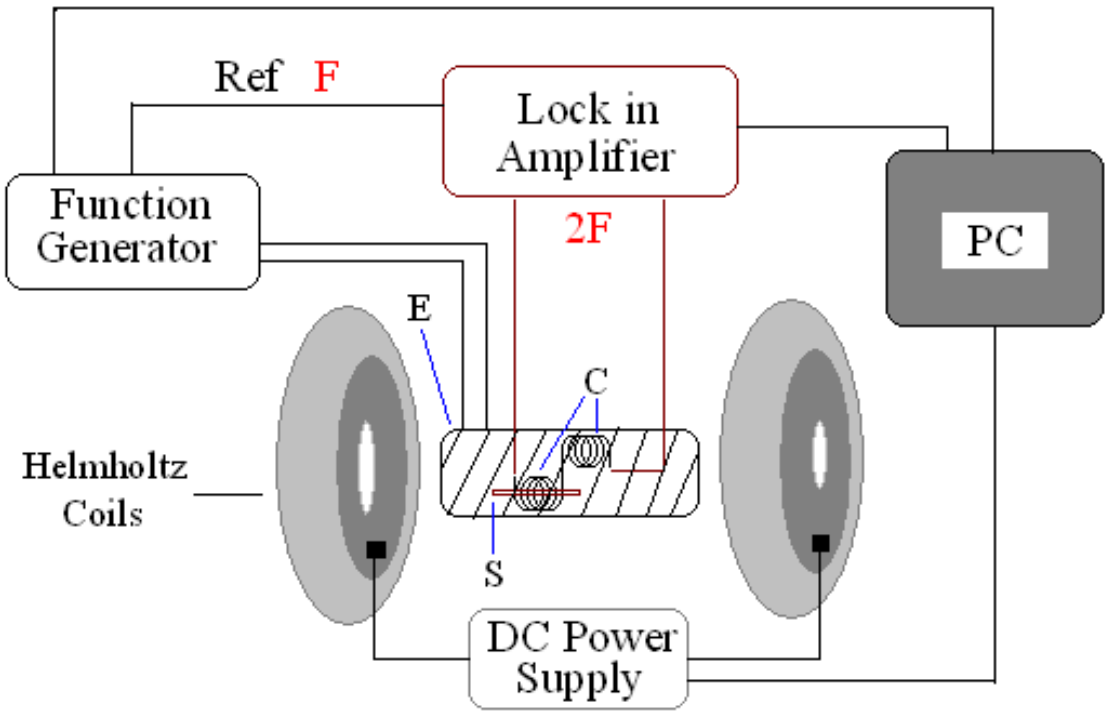

Figure 4.2.1: Experimental arrangement for obtaining anisotropy field distribution from second harmonic response of magnetization.

A direct relationship between the second harmonic coefficient of the magnetization response and anisotropy field is used that facilitates the experimental determination of the distribution of anisotropy field using the experimental arrangement described above. This relationship is given by (see Appendix B):

$$P(H_0) = 2 \frac{H_0}{\mu_0 M_s N S \omega A^2} e_2 \qquad (4.2.3)$$

Where e_2 is the voltage measured corresponding to the second harmonic, N is the number of turns of pick up coil, S is the cross section of the sample, A is the amplitude of small ac field applied, H_0 is the strength of applied static magnetic field, Ms is the saturation magnetization of the sample under investigation and ω is the frequency of applied ac field. From equation 4.2.3 it is clear that the anisotropy field distribution is directly proportional to the amplitude of the second harmonic voltage response. It should be noted that when the applied field approaches the coercive field value the second harmonic voltage goes to a minimum. On the other hand when applied field value approaches the anisotropy field value for the sample being studied, the second harmonic voltage tends towards maximum [5].

4.2.2 Results and discussion

The experimental observations of second harmonic response of magnetization curve as a function of applied static magnetic field for annealed $Fe_{84}Zr_{3.5}Nb_{3.5}B_8Cu_1$ samples are represented in Figure 4.2.2. The anisotropy field value was approached from the higher field side (designated as H_k-up) which is depicted by red curve (symbols + line) and also from lower field side (designated as H_k-down) as depicted by the black curve (symbols + line).

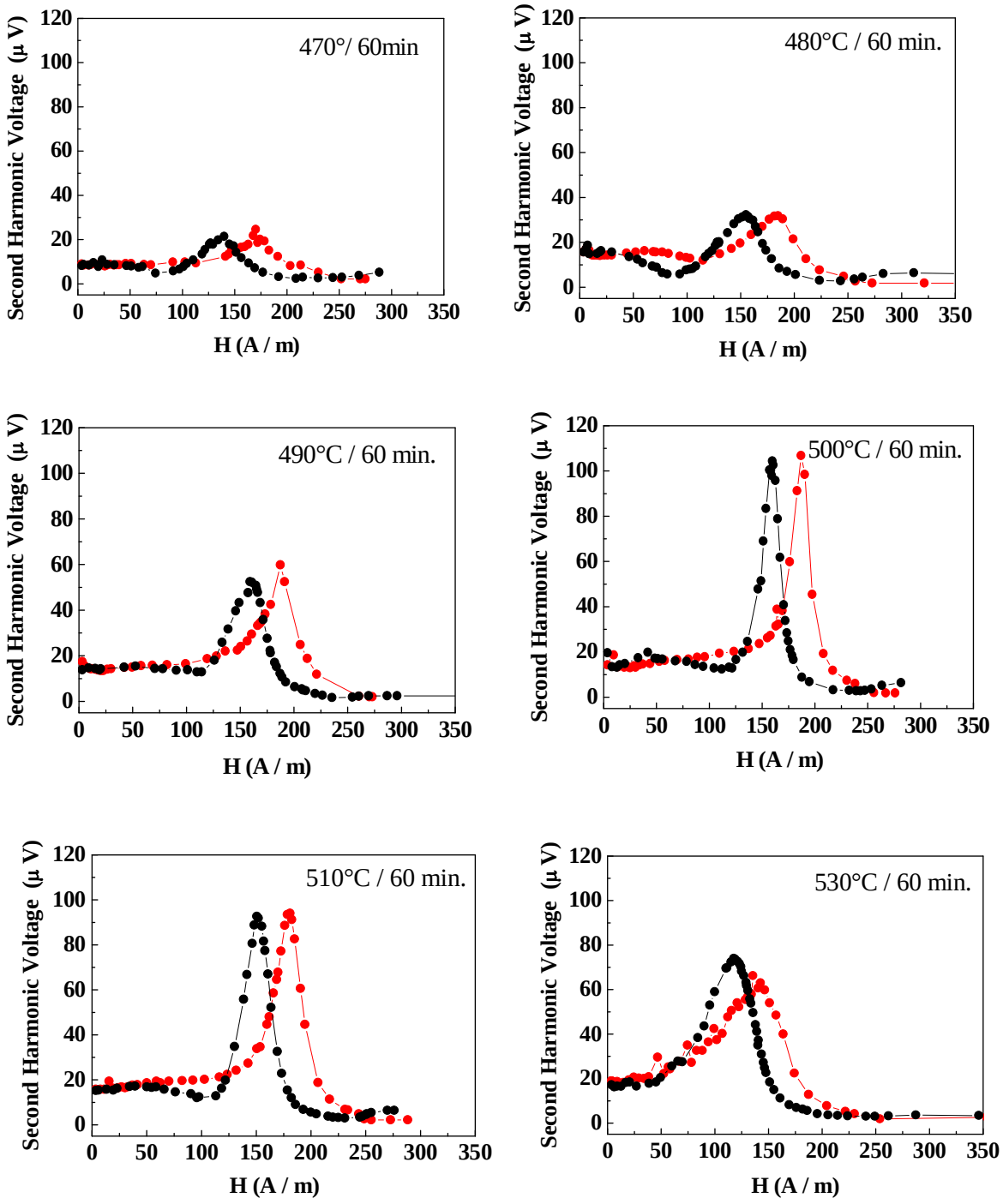

Figure 4.2.2: Representative anisotropy field distributions for $Fe_{84}Zr_{3.5}Nb_{3.5}B_8Cu_1$ ribbons annealed at various temperature for 60 minutes.

Anisotropy field values are represented by the value of the applied field corresponding to which the peak value of the second harmonic voltage is observed. It should be noted that there is a difference in the value of the anisotropy field corresponding to the direction in which the field value is approached. This difference may be either ascribed to the hysteresis behavior of the sample or it may be an effect of change in the coupling between the nanocrystallites which affects the soft magnetic behavior. Figure 4.2.3 depicts the comparison between variation of coercive field (H_c) and anisotropy field values as a function of annealing temperature. Both anisotropy field and coercive field decreases in similar way showing that annealing treatment decreases the effective anisotropy value thereby resulting in the respective decrease in coercivity.

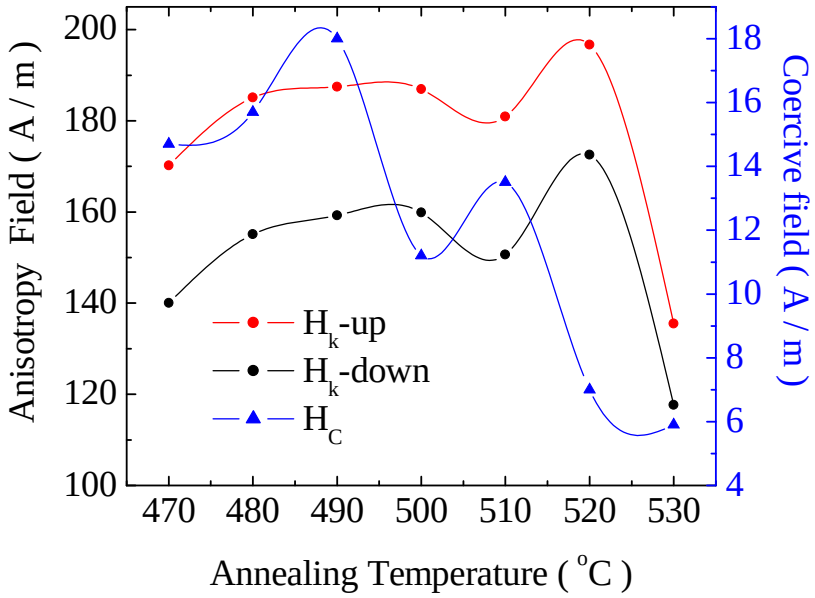

Figure 4.2.3: Annealing temperature dependence of anisotropy field and coercive field for studied $Fe_{84}Zr_{3.5}Nb_{3.5}B_8Cu_1$ alloy system.

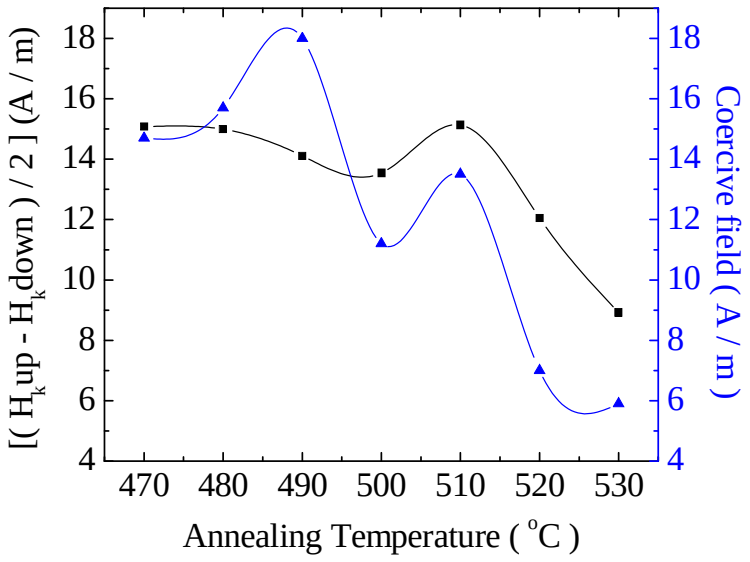

Figure 4.2.4: Variation of ($H_k$up – $H_k$down) / 2 and coercive field with annealing temperature for studied composition.

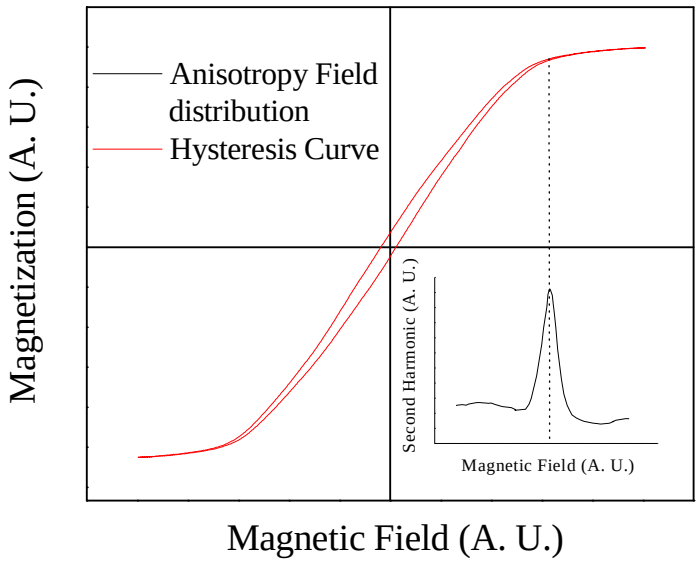

Figure 4.2.5: Representation of hysteresis cycle and corresponding anisotropy field distribution.

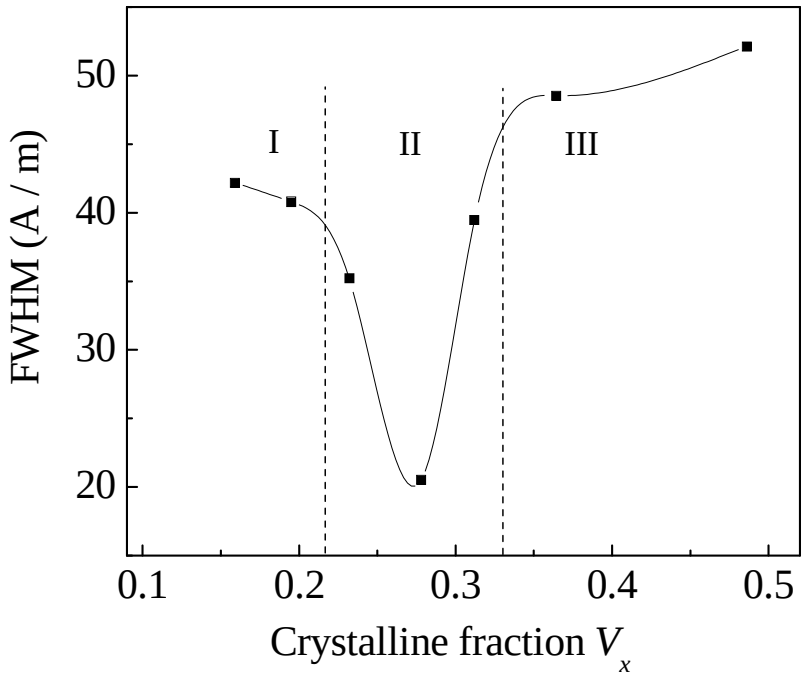

Figure 4.2.6: Variation of the width of the anisotropy field distribution with nanocrystalline volume fraction.

It may be noted that this method of determining the second harmonic response of magnetization can be used as an alternative probe to get an idea of coercive field of the system. Figure 4.2.4 shows the variation of half the difference of the H_k-up and H_k-down values with annealing temperature. It may be seen that the variation of this quantity and coercive field exhibit similar behavior. Also the order of magnitude is quite close. So this difference of the H_k-up and H_k-down values can be quite well identifiable with the effective anisotropy of the system. As shown in figure 4.2.5 the peak of the anisotropy distribution appears where the system is well saturated. It means that the domain walls no more exists and the rotation is the dominant mechanism that leads the magnetization process. As the

determination of anisotropy field distribution is free from drifts as any integration is not involved. It may be said that the anisotropy field thus determined presents the real image of effective anisotropy that governs the magnetization mechanism. As we know that value of anisotropy field is not well defined for the systems in which random anisotropies are present. There exists a distribution of anisotropy field originated possibly because of the presence of the randomly oriented anisotropy axis. As shown in figure 4.2.6, the width of the distribution of anisotropy field (FWHM) value first decreases with increasing crystalline volume fraction as indicated by region I. Further it approaches (region II) a minimum value corresponding to 490^{o}C. The width of the anisotropy field distribution increase further for higher annealing temperatures (as indicated by region III). This can also be observed by inspecting the figure 4.2.2 where representative anisotropy field distributions are shown. This may be explained on the basis of existence of random anisotropies manifested in terms of broad distribution of anisotropy field values. In region I the anisotropy values are dominated by the amorphous phase as the size of the grains are small and also the distance between these grains is large so the random anisotropies corresponding to amorphous phase gets averaged over but quenched in stresses still exists. As the annealing temperature increases the grains behaves more or less like hard particles, i.e. the region II of figure 4.2.6 indicates the presence of single domain particles leading to the hardening of magnetic response. Whereas the region III corresponds to the situation where volume fraction is large enough and the stresses are almost absent. This increases the exchange coupling among nanocrystallites which give rise to the narrowing of the anisotropy distribution as the randomness in the orientations of anisotropy axis is reduced because of increased exchange coupling.

4.3 Giant magnetoimpedance measurements

4.3.1 Introduction

The giant magneto impedance (GMI) effect is referred to huge changes in the impedance of a magnetic material when submitted to simultaneous action of an external longitudinal static magnetic field and a transverse AC field generated by an alternating current of RF frequency or a pulsed field created by a current flowing along the element. It was first reported in 1993 though this effect was known since long but somehow didn't attract any interest [22-24]. Recently, the GMI effect has been studied extensively because of its potential applications in numerous sensor elements. As GMI is sensitive to the external dc magnetic field or applied alternating current and to the applied stress, it became possible to design magnetic field sensors, wireless magnetic field sensors, current sensors and stress sensors. Many industrial and engineering applications of GMI sensors have been proposed and realized to date including computer disk heads, rotary encoders, pinhole detectors, displacement detection sensors, direction sensors for navigation, field sensors, biomedical sensors, car traffic monitoring, antitheft systems [25]. The active magnetic material element used in these sensors is usually in the form of soft thin ribbon, micro-wire or occasionally thin film. The overall effect of the magnetic field application is to induce strong modifications in the effective magnetic permeability of the magnetic element. The field and current distributions within the sample are predominantly decided by the effective permeability of the material. Magnetic permeability in case of soft magnetic materials can exhibit drastic changes even when the applied field is small enough to cause strong variations in the internal fields and electrical current density inside the sample. This

consequently affects the impedance of the material and this effect strongly depends upon the frequency of applied current and the magnetic anisotropy present in the sample.

The giant magneto impedance effect is expressed in terms of the relative change of the impedance (Z) with the applied field (H) as

$$\Delta Z / Z\ (\%) = [Z(H) - Z(Hmax)] / Z(Hmax) \times 100 \qquad \textbf{- (4.3.1)}$$

The complex impedance, $Z = R + j\omega L$ of a magnetic element is given by the ratio V_{ac} / I_{ac}. where I_{ac} is the amplitude of sinusoidal current passing through the conductor and V_{ac} is the voltage measured across the ends of the element. Depending on the frequency of driving alternating current that flows through the sample, the GMI effect can be separated into three different regimes [26]:

- Low Frequency regime (1 – 10 kHz) - In this regime the main role of the alternating current is to generate a circumferential time varying field which generates a longitudinal electric field whose value at the surface determines the inductive voltage across the sample. Thus at relatively lower frequencies the field dependence of impedance is attributed to its inductance which is proportional to the circumferential permeability.
- Moderate frequency regime (10 kHz – 1GHz) - Over the moderate scale of few MHz the drastic changes in the impedance of samples is interpreted in terms of classical skin effect in a magnetic conductor with scalar magnetic permeability. This is basically a consequence of the change in the penetration depth of alternating current in the presence of external static magnetic field. Applied current effectively flows in an outer part of the cross section of the magnetic element. The penetration depth which gives a measure of this effect is expressed as:

- $\delta = (2\,\rho / \omega\mu_o\,\mu_t)^{1/2}$ **- (4.3.2)**

  Where ρ is electrical resistivity, μ_t is the relative transverse permeability. As the transverse permeability varies by orders of magnitudes by applying longitudinal DC magnetic field, the penetration depth also varies resulting in huge impedance changes.

- High frequency regime (~ few GHz)- In order to understand the experimental results in this regime several quasi static models were suggested [27] that did not consider the dynamic effects related to the rapid motion of the magnetization. At higher frequencies magnetization rotation dominates the magnetization process. Several models including the effect of circumferential or helical anisotropy and exchange effects have been suggested that supports the observation of ferromagnetic resonance and anti resonance in magnetic materials using GMI effect [28].

4.3.2 Effect of annealing on magneto transport properties of $Fe_{84}Zr_{3.5}Nb_{3.5}Cu_8B_1$ ribbons

Nanoperm alloys are particularly important because of their high saturation magnetization (above 1.5 T) and low magnetostriction [13, 29], owing to the higher content of Fe with respect to Finemet-type alloys and to the small amounts of Zr and B in the nanograins [13]. Although Fe-based alloys were supposed to have lower giant magneto-impedance (GMI) responses than Co-based systems because of the lack of transverse anisotropy, these systems have displayed not negligible GMI values when being in the nanocrystalline state. This fact has been related to their excellent soft magnetic properties depending on low-

grain dimension and low-magnetostriction [30] that promote high permeability values. Rather weak giant magneto-impedance response is usually given by materials in the amorphous phase, but the giant magneto impedance effects strengthens when nanocrystallization leads to the best soft magnetic properties [31], and then disappears when the crystallites start growing too much in size. Giant magneto-impedance has been measured (see appendix C) on as-quenched and annealed $Fe_{84}Zr_{3.5}Nb_{3.5}B_8Cu_1$ samples by means of the 4-contacts technique with an Agilent 4294 A impedance meter, for exciting current frequencies in the range 100 kHz -30 MHz and under a static longitudinal magnetic field up to H_{max} = 40 kA/m using set of Helmholtz coils. On all studied samples, GMI decreases on increasing the exciting current frequency, displaying maximum values at 100 kHz and vanishingly small values at 30 MHz. Representative Case is depicted in figure. 4.3.1, that shows GMI curves for the sample annealed at 490 °C for 60 minutes at selected frequencies. Only the portion of the curves at applied fields less than 3000 A/m is shown. The peak values of the GMI ratio are reported in Table 4.3.1.

Table 4.3.1 GMI ratio at selected frequencies for the sample annealed at 490 °C for 60 minutes.

Frequency (MHz)	**GMI $_{max}$ (%)**
0.1	5.34
0.5	3.54
1.0	2.59
2.0	1.72
5.0	1.01
10.0	0.87
20.0	0.44
30.0	0.35

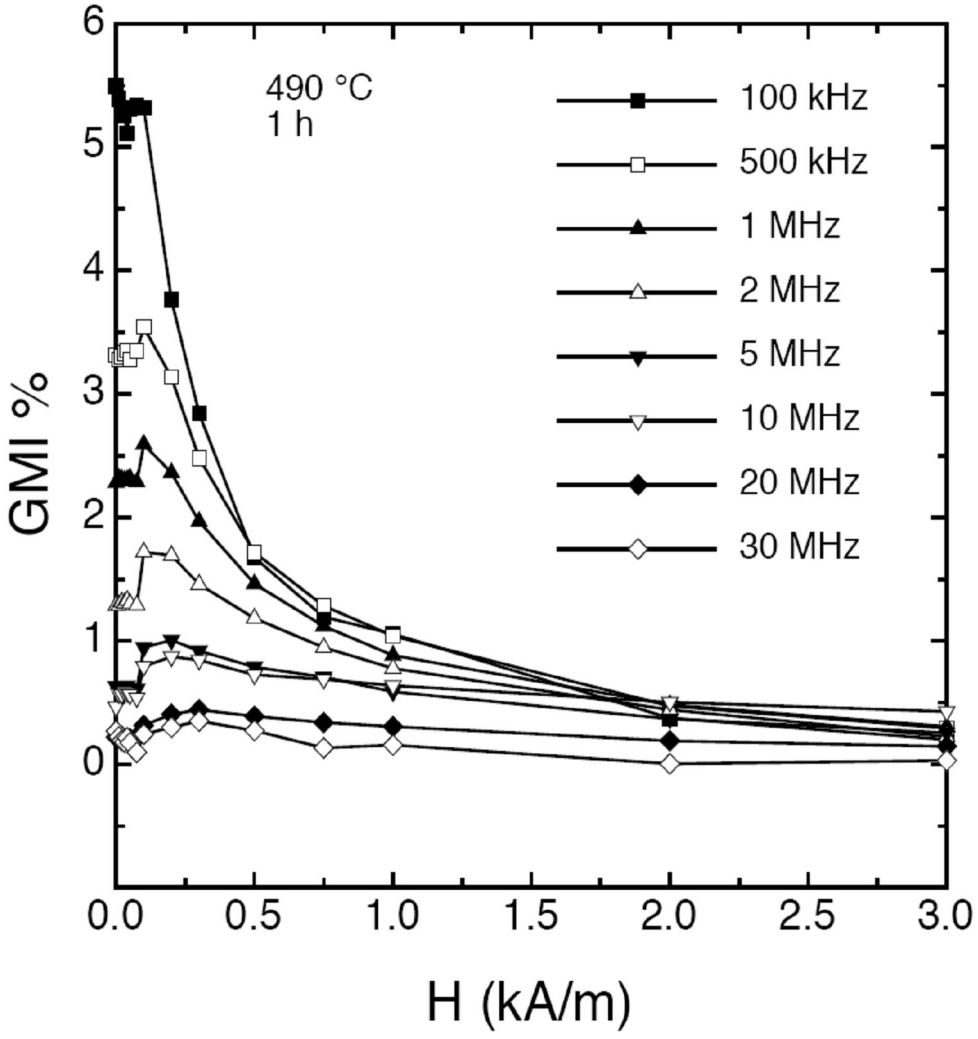

Figure 4.3.1: GMI curves at selected frequencies for the $Fe_{84}Zr_{3.5}Nb_{3.5}B_8Cu_1$ sample annealed at 490 °C for 60 minutes.

This behaviour is consistent with the results obtained on similar alloys [32] that show that a quick decrease of magnetic permeability on increasing frequency is to be expected, with values close to that of air at frequencies above 1 MHz. Thermal treatments affect the GMI response at all frequencies, as shown in figure 4.3.2, that reports the maximum GMI values measured at a frequency of 100 kHz on all as-cast and annealed samples, as a function of annealing temperature (T_a).

The sample annealed at 490 °C for 1 h displays a remarkable increase of its GMI response with respect to the as-cast specimen. Higher annealing temperatures first reduce the magneto impedance ratio, than increase it again towards values approaching 6% for the sample with the largest crystalline fraction and crystallites size. This is the sample that is characterized by the softest magnetic properties (lowest H_c values, as shown in figure 4.1.2), thus confirming that in nanocrystalline materials the best magneto impedance response is achieved when the soft magnetic properties of the alloy are improved. Annealing time affects both the crystalline volume fraction and crystallites size (see Table 4.1.1), and consequently the GMI response is also influenced, as reported in figure 4.3.3 for the sample annealed at 490 °C. As expected, longer annealing times induce larger V_x and D values that in turn cause a progressive increase of the magneto impedance response of the material.

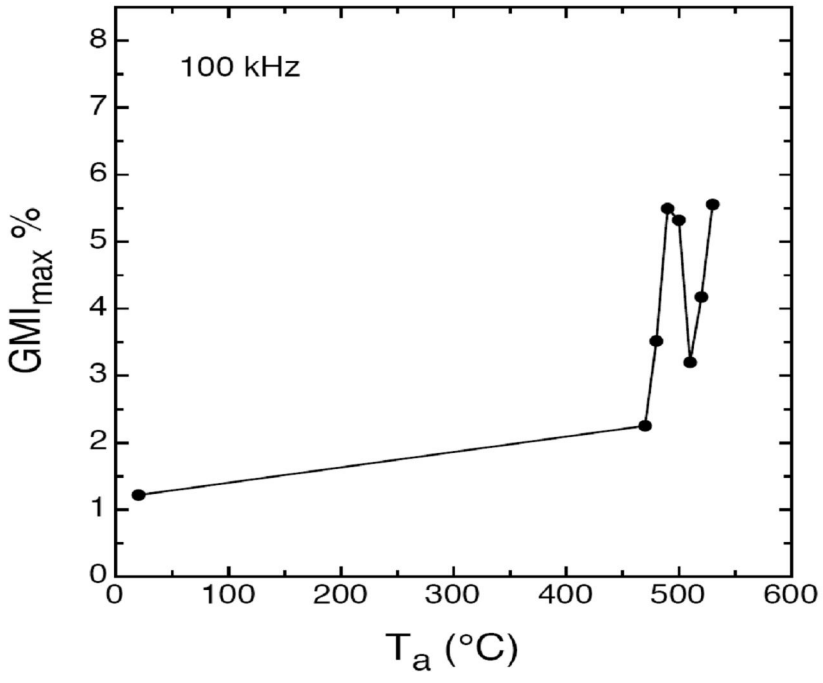

Figure 4.3.2: Maximum GMI response at 100 kHz as a function of annealing temperature.

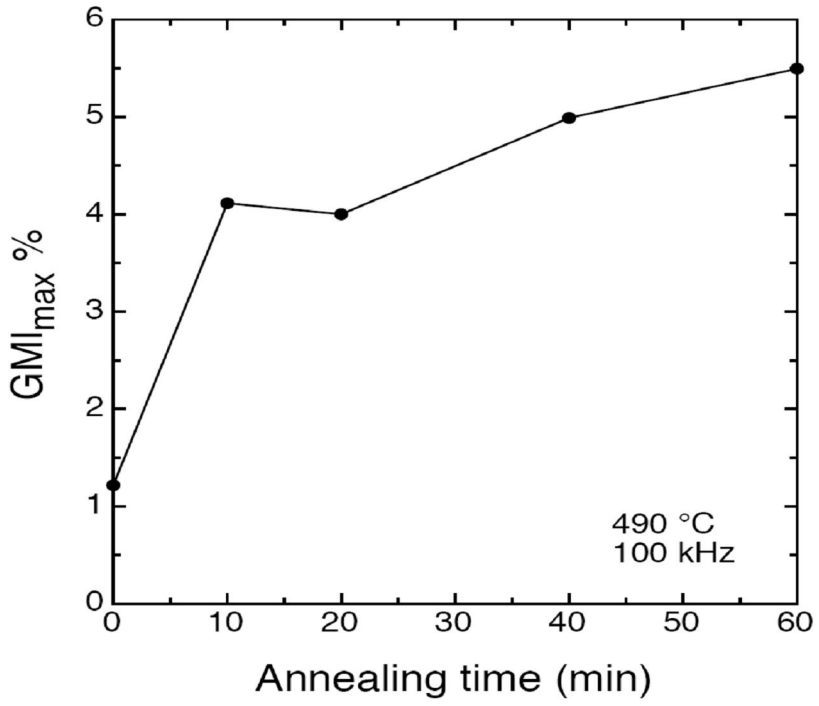

Figure 4.3.3: Maximum GMI response at 100 kHz as a function of annealing time for the sample annealed at 490 °C.

4.4 Departure from random anisotropy mechanism

4.4.1 Introduction

The coercivity of variety of soft magnetic nanocrystalline materials is governed by the spatial fluctuation amplitude of the magnetic anisotropy energy when the domain wall displacement pre dominates the magnetization process. As described in the earlier chapters also that this magneto crystalline anisotropy randomly fluctuates over a scale much smaller than the domain wall width and is therefore gets averaged out by the virtue of exchange interaction. In general we may say that the soft magnetic behaviour of amorphous and nanocrystalline materials can be understood by introducing a correlation length which can be identified with the ferromagnetic exchange length over which the magnetic moments are coupled via exchange interaction. Disorder in the structure gives rise to randomness in the interaction of magnetic moments. The randomness in the exchange interaction does not qualitatively affect the magnetic behaviour whereas random anisotropy influences the magnetic properties strongly. Even for amorphous materials random anisotropy does not cancel out completely, rather there exists a balance between anisotropy and exchange forces. The origin of soft magnetic behaviour in these materials is based on the averaging of random anisotropies over respective correlation length scales through magnetically coupled regions. In this section we have presented a comparison between the two limiting approaches that describe the hysteresis behaviour of soft magnetic nanocrystalline materials. This comparison is based upon the structural and magnetic investigations of $Fe_{84}Zr_{3.5}Nb_{3.5}B_8Cu_1$ (also reported in section 4.1) and $Fe_{58}Co_{25}Nb_7Cu_1B_9$ alloy that has been carried out. This is an attempt to reach to a grain size and volume fraction dependence of coercive field that well describes the magnetic behavior observed for the alloy

composition that we have investigated in the form of amorphous ribbons (~20 μm thick and 10 mm wide). The amorphous ribbons of nominal composition $Fe_{58}Co_{25}Nb_7Cu_1B_9$ were also studied after annealing between 370 to 430 ^oC for 30 min. in flowing argon to obtain various stages of partial crystallization. The first crystallization peak temperature (T_{x1}) for the studied alloy was 443 ^0C, determined using differential scanning calorimetery (DSC) measurements at the heating rate of 5 ^0C/min. X-ray diffraction measurements on as-cast and thermally annealed samples were performed using Cu-K_α radiation. XRD patterns were analyzed by fitting a crystalline and amorphous component using pseudo-Voigt line profile to obtain average grain size *D*, and crystalline volume fraction V_x. Hysteresis loops were recorded at 37 Hz using a computer controlled set-up in order to obtain coercive field (H_c). Saturation induction (~ 1.28 Tesla) was determined by Vibrating Sample Magnetometer with H_{max} = 700 kA/m.

4.4.2 Results and discussion

Figure 4.4.1 sketches the two situations explaining the two approaches that we have tried to apply in order to understand the deviation from the random anisotropy mechanism that was originally proposed by Herzer (RAM approach) to describe the soft magnetic properties of optimally crystallized alloys. Néel's approach is based on the motion of domain wall (DW approach) through amorphous medium containing small crystallites. As shown in figure 4.4.1 (b**)** the volume fraction of nanocrystals is low enough. The potential energy of domain wall is considered as random function of the position of domain wall and as a consequence of which, the random fluctuations in the energy of domain wall gets averaged over the scale defined by the thickness of domain wall (L_N) itself [33]. On the other hand Herzer approach (RAM approach) is based on the softening of magnetic behaviour originated because of

averaging of random magneto crystalline anisotropies over a length scale (L_R) governed by nanocrystalline phase that is greater than the average grain size *D* [6, 7].

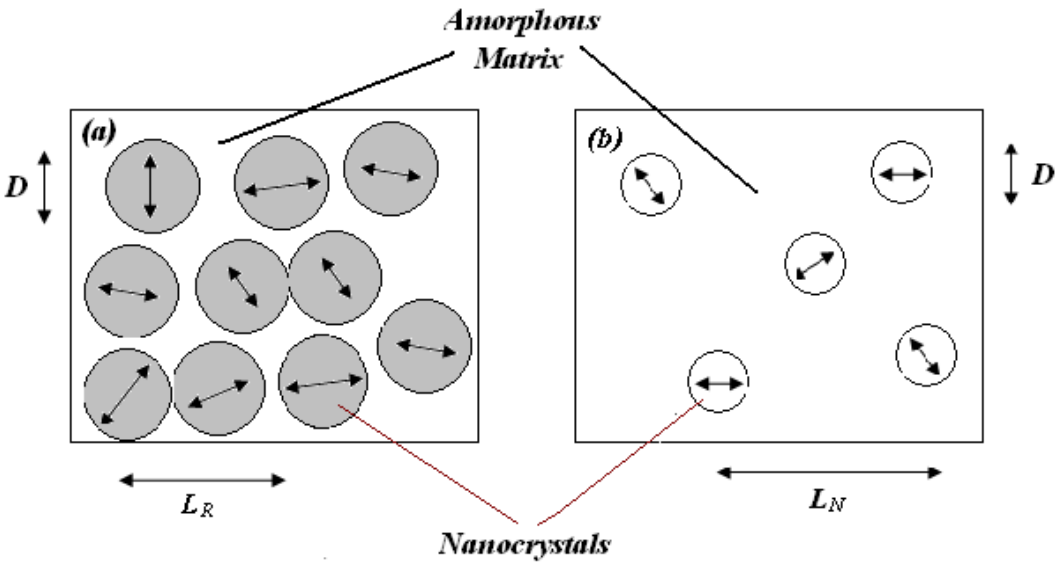

Figure 4.4.1: Schematic of the situations in case of **(a)** RAM approach **(b)** DW approach

In RAM approach inter granular phase is assumed to be magnetic that allows the exchange interaction among the nanograins present within the volume defined by the correlation length scale mentioned above. As shown in figure 4.4.1 let us consider that the volume fraction of the nanocrystalline phase is $V_x = n D^3$, where *n* is number of spherical crystallite (of average size *D*) per unit volume. In the DW approach (figure 4.4.1b) volume fraction is considered low enough such that nanocrystals are too far apart to be exchange coupled and consequently the length scale that dominates the magnetization process is no more dictated by the parameters of crystalline phase. These nanocrystallites behave like single domain particles with their easy axis oriented at random so that the anisotropy energy of the

nanocrystals (in the present alloy system, bcc Fe-Co phase) contained within the domain wall is responsible for the opposition to domain wall motion. The variation in the energy of domain wall as a result of presence of nanocrystallite depends upon the magnetization orientation when anisotropy energy has following dependence on the direction cosines of magnetization; $E = D^3 K_1 (\alpha_1^2 \alpha_2^2 + \alpha_2^2 \alpha_3^2 + \alpha_3^2 \alpha_1^2)$. The anisotropy energy can vary from 0 (easy axis) to $D^3 K_1 / 3$ (hard axis), thus its value fluctuates by $\pm D^3 K_1 / 6$ about an average value [34]. The random orientations of easy axes of the nanocrystallites are independent. Thus the fluctuations in the energy of domain wall of area S and width L_N is given by $\sim N^{1/2} D^3 K_1 / 6$ where N is the number of grains contained within the domain wall $\sim n S L_N$ .When the domain wall moves by a distance equal to its width under the influence of the applied magnetic field, the typical force that hinders the domain wall movement is proportional to the fluctuations of the domain wall energy and to the characteristics length scale (domain wall width) over which these fluctuations take place. This pinning force can be overcome by the force exerted by the applied magnetic field. Equating the above two forces yields the following volume fraction and grain size dependence of coercive field;

$$H_C = (V_x^{1/2}) (K_1 / 12 \mu_0 M_S) (D / L_N)^{3/2} \qquad \textbf{(4.4.1)}$$

Where L_N is the bulk domain wall thickness governed by amorphous phase typically ~ μm, K_1 is the anisotropy energy constant of crystalline phase. On the other hand in the RAM approach (figure 4.4.1a) proposed for optimally annealed systems the volume fraction is sufficiently high so that the nanocrystals are almost in contact and the random magneto-crystalline anisotropies averaged out over a length scale that is larger than the grain size. This spatial scale (L_R) is determined mainly by the properties of crystalline phase as $\sim (A / K_1)^{1/2}$. Consequently the effective anisotropy scales as $\sim K_1 / N^{1/2}$, where N is the number

of nanograins present within the exchange coupled volume. As a result apart from a proportionality factor the coercive field is given by:

$$H_C \sim (V_x^{\,2})\,(K_1 / \mu_0 M_S)\,(D / L_R)^{\,6} \qquad \textbf{(4.4.2)}$$

It can be seen that the grain size dependence of coercive field suggested by equation (4.4.1) is weaker as compared to D^6 dependence [6, 7, and 35] in equation (4.4.2). Beside the random anisotropies, presence of induced uniaxial anisotropy has been reportedly [36] responsible to lower the exponent of D from 6 to 3. Moreover low values of crystalline volume fraction and an implicit dependence on the length of inter granular region are also very important factors that affect the correlation length determining the magnetic properties.

Table 4.4.1 depicts experimentally obtained values of V_x, D, and H_c for $Fe_{84}Zr_{3.5}Nb_{3.5}B_8Cu_1$ ribbons. It also shows the values of coercive field calculated on the basis of RAM and DW approach. It may be noted that with increasing volume fraction and grain size experimentally obtained value of coercive field does not increases continuously. Whereas coercive field values obtained on the basis of RAM and DW approach increases with V_x and D. Comparison of the coercive field values suggests that the magnetic behavior of $Fe_{84}Zr_{3.5}Nb_{3.5}B_8Cu_1$ alloy system can not be explained on the basis of random anisotropy mechanism. On the other hand DW approach also does not yield a reasonable explanation of the same. Consequently we have also studied Fe-Co based alloy just in order to see which of the two approaches describes well the magnetic behavior. Table 4.4.2 depicts experimentally obtained values of V_x, D, and H_c along with the values of coercive field calculated on the basis of RAM approach for $Fe_{58}Co_{25}Nb_7Cu_1B_9$ ribbons. It may be inferred that the addition of cobalt and the partially crystallizing annealing conditions modifies the

resulting nanocrystalline structure which in-turn affects the soft magnetic properties [37, 38] of studied composition when compared to the optimally annealed cobalt free composition [6, 7]. It may be noted that addition of cobalt enhances the curie temperature of resulting nanocrystalline material which makes it more suitable to work at high temperatures [39].

Table 4.4.1: Volume fraction and grain size dependence of coercive field (H_c) values for $Fe_{84}Zr_{3.5}Nb_{3.5}B_8Cu_1$ ribbons obtained experimentally and those obtained using equations 4.4.1 (DW approach) and 4.4.2 (RAM approach).

V_x (%) (±2)	D (nm) (±1)	H_c (A/m) Experimental	H_c (A/m) RAM	H_c (A/m) DW
15.9	7.4	14.7	4.7	0.7252
16.2	7.6	11.2	5.8	0.7619
19.5	8.3	15.7	13.9	0.9540
20.1	8.4	14.4	15.9	0.9861
21.4	8.7	12	22.3	1.0725
22.8	9.1	12	33.2	1.1842
23.2	9.2	18	36.7	1.2143
27.8	9.4	11.2	59.8	1.3729
31.2	9.5	13.5	80.4	1.477
36.4	9.6	7	116.5	1.6213
48.6	10.2	5.9	298.8	2.0518

Table 4.4.2: Annealing temperature dependence of volume fraction of nanocrystalline phase V_x, average grain size D and coercive field (H_c) values for $Fe_{58}Co_{25}Nb_7Cu_1B_9$ alloy obtained experimentally and the ones obtained using equation 4.4.2.

Ann. Temp	V_x **(%) (±2)**	D **(nm) (±2)**	H_c **(A/m) Experimental**	H_c **(A/m) RAM**
370 ^oC	8	12	26.5	11.66
390 ^oC	10	12	20.4	18.23
410 ^oC	16	16	28	262.14
430 ^oC	28	18	37.6	1627

In practice the contributions of magnetoelastic or annealing induced anisotropies to the magnetization process always complicate the treatment and interpretations of the intrinsic physical processes that are responsible for the magnetic behaviour of nanocrystalline materials. Fe based alloys in the form of ribbons have been reported to exhibit large Barkhausen effect due to evident presence of axial domains arising because of the positive magnetostrictive constant whereas cobalt based alloys have been reported to have transversal domain pattern because of negative magnetostrictive coupling [40]. Consequently the addition of cobalt in Fe based alloys results in low magnetostrictive material which remain a key feature that enhance soft magnetic properties. Increase of annealing temperature enhances the relative volume of developing nanograins which eventually alters the corresponding Co content in the bcc Fe-Co nanograins and hence also affects the stability of the studied composition against crystallization. Figure 4.4.2 a and b

shows the variation of coercive field with grain size and volume fraction respectively, based on the values of coercive field obtained experimentally and on those calculated using DW approach by equation 4.4.1. The coercive field value for the sample annealed at 390^{o}C is less than that observed for the sample annealed at 370 ^{o}C. This can be due to the structural relaxation initiated by the rearrangement of local disorders caused by the fact that the onset of crystallization results in the loss of Fe and Co from the amorphous matrix. It is worth noting that with increase of annealing temperature the volume fraction of crystalline phase also increases (the average grain size increases only slightly), but as expected for this range of the size of crystallites, it does not likely result in magnetic softening due to random anisotropy averaging [6, 35]. It is also possible that self magnetic field of domains may also induce uniaxial anisotropy during annealing or cooling. For bcc Fe-Co crystalline phase, taking $A = 2 \times 10^{-11}$ J m^{-1} and $K_1 = 5 \times 10^{4}$ J m^{-3}, the exchange length comes out to be ~ 20 nm which is of the same order of magnitude of the average grain size. It should however be noted that for Fe-Co system K_1 varies rather weakly with small Co content in ordered Fe-Co alloy. Table 4.4.2 depicts the coercive field values obtained on the basis of RAM approach. Comparison between the these values of coercive field determined experimentally and calculated using RAM approach suggests that the random anisotropy mechanism is not governing the coercive field behaviour as expected on the basis of aforesaid correlation length determined by crystalline phase. This can be attributed to the fact that for the alloy under investigation, the inter-granular distance d [41] for the samples annealed at various temperatures is 13.21, 11.27, 15.16 and 9.10 nm respectively and it is comparable to the average grain size D leading to a situation where the nano-grains are not effectively exchange coupled as it happens when the crystalline fraction approaches unity.

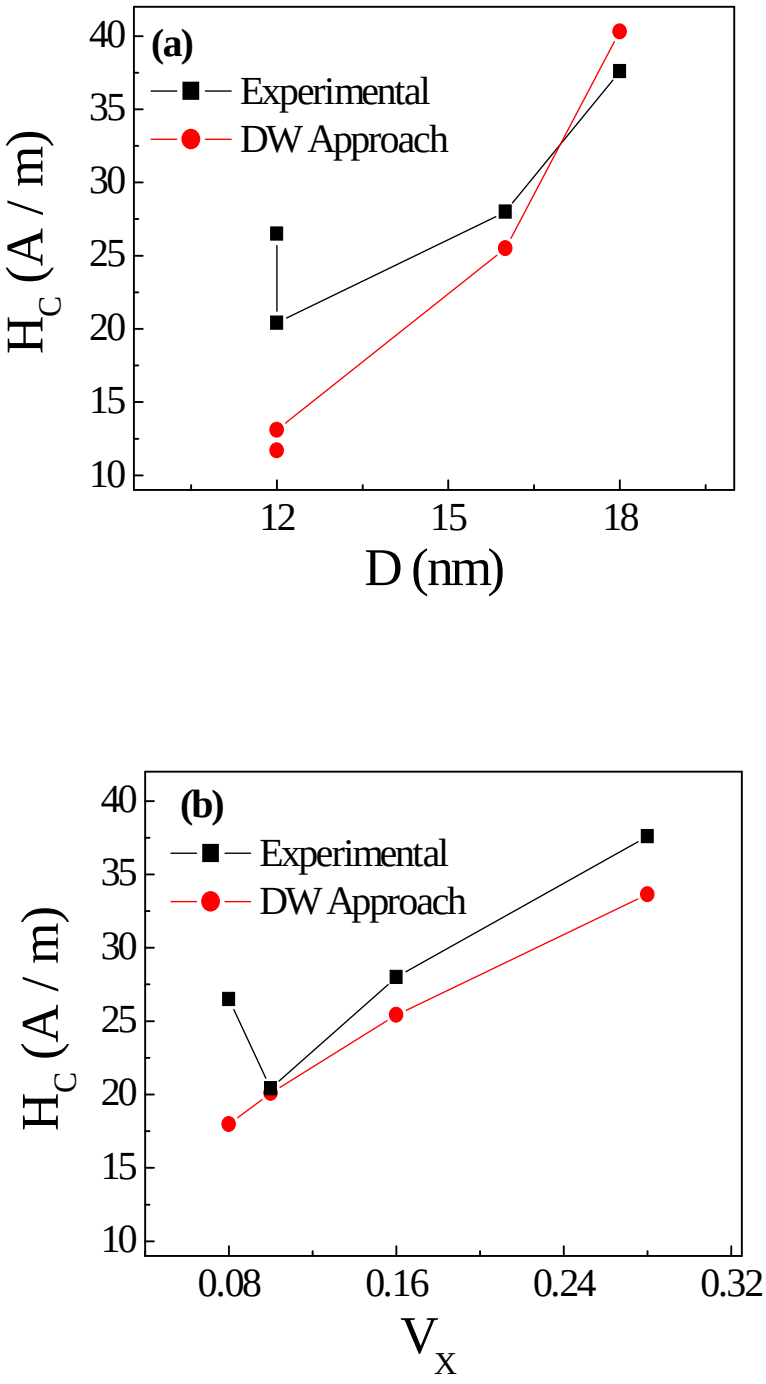

Figure 4.4.2: Variation of coercive field with (a) grains size and (b) Volume fraction of nanocrystalline phase for $Fe_{58}Co_{25}Nb_7Cu_1B_9$ alloy system.

In earlier studies it has also been reported that the microstructure affects the hysteresis properties in such a way that the measured coercive field follows a fourth power dependence of mean grain size, which is a consequence of the domain wall pinning by nanograins and some separate magnetization mechanisms are supposed to be associated with the amorphous and crystalline phase [42]. In the present case the correlation length is mainly controlled by amorphous phase (72%-92%) and nanocrystals are only contributing to the fluctuations in domain wall energy thereby acting as pinning centres. It may be inferred on the basis of structural and magnetic investigations [43] of partially crystallized samples of $Fe_{58}Co_{25}Nb_7Cu_1B_9$ alloy that the magneto-crystalline anisotropies are not randomly averaging out over the length scale determined by nanocrystalline phase. Magnetic behaviour is rather governed by the correlation length scale that is determined by the amorphous phase and magnetic properties seem to have a less strong dependence on average grain size with respect to the one expected in the framework of RAM approach where the correlation length is governed by the nanocrystalline phase. Results based on DW approach shows a good agreement with the experimental observations. Limits of applicability of the two approaches seem to be dependent strongly upon the extent of crystallization that considerably influences the fact that which phase is regulating the magnetic correlation length leading the magnetization process.

References:

[1] R. Hasegawa, G. E. Fish and V. R. V. Rammanan: proc. 4th Int. Conf. Rapidly quenched Materials, Sendai 1981, eds. T. Masumoto and K. Suzuki (The Japan Institute of Metals, Sendai (1982) 929.

[2] Y. Yoshizawa, S. Oguma and K. Yamauchi, J. Appl. Phys. 64 (1988) 6044.

[3] K. Hiraga, O. Kohmoto, Mater. Trans. JIM 11(1991) 868.

[4] K. Hono, K. Hiraga, Q. Wang, A. Inoue, T. Sakurai, Acta. Metll. Mater. 40 (1992) 2137.

[5] H. Hoffman, J. Appl. Phys. 35 (1964) 1790.

[6] G. Herzer, IEEE Trans. Mag. 25(1989) 3327.

[7] G. Herzer, IEEE Trans. Mag. 26 (1990) 1397.

[8] Y. Fuji, H. Fujita, A. Seki, T. Tomida, J. Appl. Phys. 70 (1991) 6241.

[9] K. Suzuki, N. Kataoka, A. Inoue, A. Makino, T. Masumoto, Mater. Trans. JIM 31 (1990) 743.

[10] K. Suzuki, A. Makino, N. Kataoka, A. Inoue, T. Masumoto, Mater. Trans. JIM 32 (1991) 93.

[11] K. Suzuki, A. Makino, A. Inoue, T. Masumoto, J. Appl. Phys. 70 (1991) 6232.

[12] A. Makino, A. Inoue, T. Masumoto, Nanostruct. Mater. 6 (1995) 985.

[13] A. Makino, T. Hatanai, Y. Naitoh, T. Bitoh, A. Inoue, T. Masumoto, IEEE Trans. Mag. 33 (1997) 1397.

[14] A. Makino, T. Hatanai, S. Yoshida, N. Hasegawa, A. Inoue, T. Masumoto, Sci. Rep. RITU A42 (1996) 121.

[15] A. Makino, T. Bitoh, A. Inoue, T. Masumoto, J. Appl. Phys. 81 (1997) 2736.

[16] R. C. O'Handley, Soft Magnetic Materials, Principles and Applications, Wiley - Interscience publications p.180.

[17] F. E. Luborsky, J. J. Becker, and R. O. McCary, IEEE Trans. Magn. MAC-11, (1975) 1644.

[18] O. V. Nielsen and H. J. V. Nielsen, J. Magn. Magn. Mater. 22 (1980) 21.

[19] M. Vazquez, E. Ascasibar, A. Hemando, and 0. V. Nielsen, J. Magn. Magn. Mater. 66 (1987) 37.

[20] J. M. Barandiaran, M. Vbzquez, A. Hernando, J. Gonzalez, and G.Rivero, IEEE Trans. Magn. MAG-25 (1989) 3330.

[21] A. Garcia, J. M. Barandiaran, G. Herzer, J. Appl. Phys. 71 (6) (1992) 3047.

[22] M. Kzminski, H. K. Lachowicz, J. Magn. Mag. Mater. 267 (2003) 35.

[23] K. Mohri, Mater. Sci. Eng. A185 (1994) 141.

[24] E.P. Harrison G. L. Turney, H. Rowe, H. Gollop, Proc. Roy. Soc. 157 (1937) 651.

[25] M. H. Phan, H. X. Peng, Progress in Material Science 53 (2008) 323.

[26] M. Knobel, K. P. Pirota, J. Magn. Mag. Mater. 242-245 (2002) 33.

[27] F. L. A. Machado, S. M. Rezende, J. Appl. Phys. 79 (1996) 6558.

[28] Britel et al. Appl. Phys. Lett. 77 (2000) 2737.

[29] A. Makino, T. Bitoh, A. Kojima, A. Inoue, and T. Masumoto, J. Appl. Phys. 87 (2000) 7100.

[30] M. Knobel, M. L. Sanchez, C. Gomez-Polo, M. Vazquez, P. Marin, and A. Hernando, J. Appl. Phys. 79 (1996) 1646.

[31] C. Appino, C. Beatrice, M. Coïsson, P. Tiberto, and F. Vinai, J. Magn. Magn. Mater. 226–230 (2001) 1476.

[32] W. Quin, Y. F. Zhang, Y. W. Du, F. Xu, Y. J. Wu, M. Zhao and F. Ma,
J. Magn. Magn. Mater. 270 (2004) 174.

[33] J.L Néel, Cah. Phys. 12 (1942) 1**,** 13(1943) 18.

[34] J. L. Porteseil, O. Geoffroy J. Magn. Magn. Mater. 140-144 (1995) 1855.

[35] G. Herzer, Scr. Mater. 33 (1995) 1741.

[36] K. Suzuki, G. Herzer, J. M. Cadogan, J. Magn. Magn. Mater. 171-181 (1998) 949.

[37] C. Gomez-Polo, P. Marin, L. Pascual, A. Hernando, M. Vázquez, Phys. Rev. B65 (2001) 24433.

[38] Zs. Gercsi, S. N. Kane, J. M. Greneche, L. K. Varga, F. Mazaleyrat, Phys. Stat. Sol. (C) 1 (2004) 3607.

[39] C. Gomez-Polo, J. I. Pérez_Landazabal, V. Recarte, J. Campo, P. Marin, M. Lopéz, A. Hernando and M. Vazquez, Phys. Rev. B 66 (2002) 12401.

[40] M. Knobel, M. Vazquez, L. Kraus, in 'Handbook of magnetic materials' edited by K. H. J. Buschow, Vol. 15 (Elsevier Science B.V. Amsterdam (2003) chapter 5.

[41] A. Hernando, M. Vàzquez, T. Kulik, C. Prados, Phy.Rev.B 51 (1995) 3581.

[42] V. Basso, G. Bertotti, P. Duhaj, E. Ferrara, V. Haslar, L. Kraus, J. Pokorny, K. Zaveta J.Magn. Magn. Mater. 157-158-144 (1996) 217.

[43] S. S. Modak, S. N. Kane, F. Mazaleyrat, M. Lo Bue and L. K. Varga
Presented in Joint European Magnetic Symposia (JEMS'08), September 14 – 19, 2008, Dublin, Ireland.

CHAPTER 5

Investigation of magnetic properties of FeZrNbBCu thin films

This chapter presents the complementary studies that were carried out on FeZrNbBCu thin films produced by ion beam sputtering in order to better understand the effect of preparation conditions on the structure and magnetic properties. The magnetic properties of as deposited and nanocrystallized thin films are reported. Thin film samples were prepared by ion beam sputtering on silicon substrate by using target made by ribbons of nominal composition $Fe_{84}Zr_{3.5}Nb_{3.5}B_8Cu_1$. Information on anisotropy field values obtained by room temperature ferromagnetic resonance measurements on as deposited samples produced by ion beam sputtering is also included in this chapter. Further this chapter reports the thickness and annealing treatment dependence of magnetic properties of thin film samples prepared by RF sputtering on glass substrate using target made up of amorphous ribbons of nominal composition $Fe_{84}Zr_{3.5}Nb_{3.5}B_8Cu_1$. All thin film samples were crystallized by thermal annealing in vacuum. Temperature dependent magnetization measurements were done using vibration sample magnetometer. Magnetic measurements were carried out on as deposited and annealed samples at room temperature using the alternating field gradient magnetometer.

- ***Introduction***
- ***Magnetic properties of ion beam sputtered FeZrNbBCu thin films***
- ***Magnetic properties of RF sputtered FeZrNbBCu thin films***
- ***References***

5.1 Introduction

Continuous interest in new ferromagnetic thin film material spurs the development of the increased areal density of hard disk data storage systems and the data transfer rate in magnetic recording systems over the past decade. Recent advances in magnetic film based memory devices hold great promise for fast, high density magnetic random access memory (MRAM) devices. The switching speed of the magnetic elements for these applications is limited, in part, by the magnetic damping in the thin film materials. An understanding of the damping mechanisms and control parameters remains one of the key challenges in the push to achieve faster switching speeds. Data storage system requires high density media along with sensitive read heads and high moment write heads. High moment soft under-layers are also important from view point of magnetic flux concentration in perpendicular recording systems and that is why the soft magnetic response of thin films is to be widely studied at all frequencies of applicative importance. Amorphous Fe-M-C (M= Zr, Hf, Nb, or Ta) thin films produced by annealing vapour deposition exhibited good soft magnetic properties [1]. Recently Fe-based soft magnetic thin films have been of interest as high density recording head materials that requires high saturation magnetization and high permeability at high frequencies. On the other hand electronic industry is in great need of improved alloys that can be used as thin film inductors for smaller passive components that can operate at higher frequencies and temperatures as well. Specifically these alloys should posses high permeability, high saturation magnetization and low coercivity. Soft magnetic properties of Fe based films have attracted a lot of interest because these are useful in fabrication of sensors, magnetic head cores, transformers and soft magnetic under layers in recording media [2-6]. Among amorphous Fe-based compositions obtained in the form of

ribbons by rapid solidification, a key role has been played by the FINEMET-type compositions displaying excellent soft magnetic properties in the nanocrystalline state [7,8] whereas Fe-Zr-B-Cu based NANOPERM family of alloys were characterized by high saturation magnetization and high permeability. This alloy family represents one of the best soft magnetic nanocrystalline materials on the basis of relative permeability versus saturation induction plot [9-12]. The soft magnetic properties in above mentioned family of alloys in the form of amorphous and nanocrystalline ribbons have been extensively studied from view point of applications and fundamental interests. This motivated the investigation of equivalent compositon in the form of thin films. Studies have shown that amorphous thin films of FINEMET composition exhibit very different magnetic behaviour as compared to rapidly quenched amorphous ribbons [13, 14]. In metallic glasses, preparation conditions such as melt temperature, quenching rate, etc., affect their structural and magnetic properties [15, 16]. Various studies have been reported in order to explain the effect of preparation conditions, post processing treatments on the structure and magnetic properties of FINEMET thin films [17, 18]. In particular case of ion beam sputtering the energy of the ion beam used for sputtering plays an important role in determining the structure of the thin film, which in turn will affect its magnetic properties. As the kinetic energy of the sputtered atoms is expected to depend on the energy of the bombarding ions, the sputtered ions will reach the substrate with different energies, and consequently the concentration of the defects in the thin film prepared with different ion energies is expected to be different [18]. We have recently carried out studies on magnetic properties and relaxation in amorphous $Fe_{73.9}Nb_{3.1}Cu_{0.9}Si_{13.2}B_{8.9}$ thin films produced by ion beam sputtering method [19]. FeNbCuSiB thin films were produced by ion beam sputtering on glass substrates starting

from a target made of amorphous ribbons of nominal composition $Fe_{73.9}Nb_{3.1}Cu_{0.9}Si_{13.2}B_{8.9}$. Ar^+ ions with energies of 500 and 1000eV have been used for sputtering the target and producing the samples designated as F500 and F1000, respectively. Sputtering rates of 1.0 and 2.6 nm/min were achieved for samples F500 and F1000, respectively; deposition time has been adjusted to have a comparable thickness on the two samples: 45.2 nm for F500 and 38.6 nm for F1000.

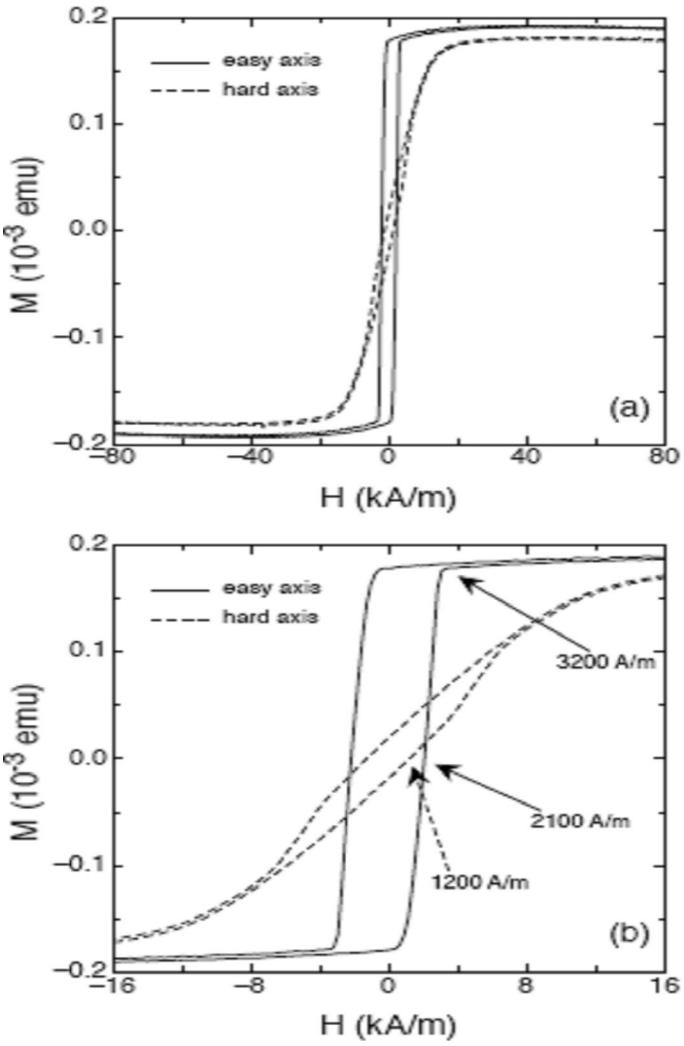

Figure 5.1.1: (a) Hysteresis loops on the F500 sample along the easy and hard magnetization axes. **(b)** Magnification of the loops shown in **(a).**

Both samples displayed uniaxial anisotropy. Magnetic hysteresis loops measured along the easy and hard axes at room temperature by means of an alternating gradient field magnetometer AGFM are reported for sample F500 and F1000 in Figure 5.1.1 and 5.1.2 respectively. The hysteresis curve displays a rather rectangular shape when measured along the easy axis, indicating a uniaxial anisotropy. In both configurations a detectable hysteresis is observed, as clearly shown in an enlargement of the same hysteresis curve

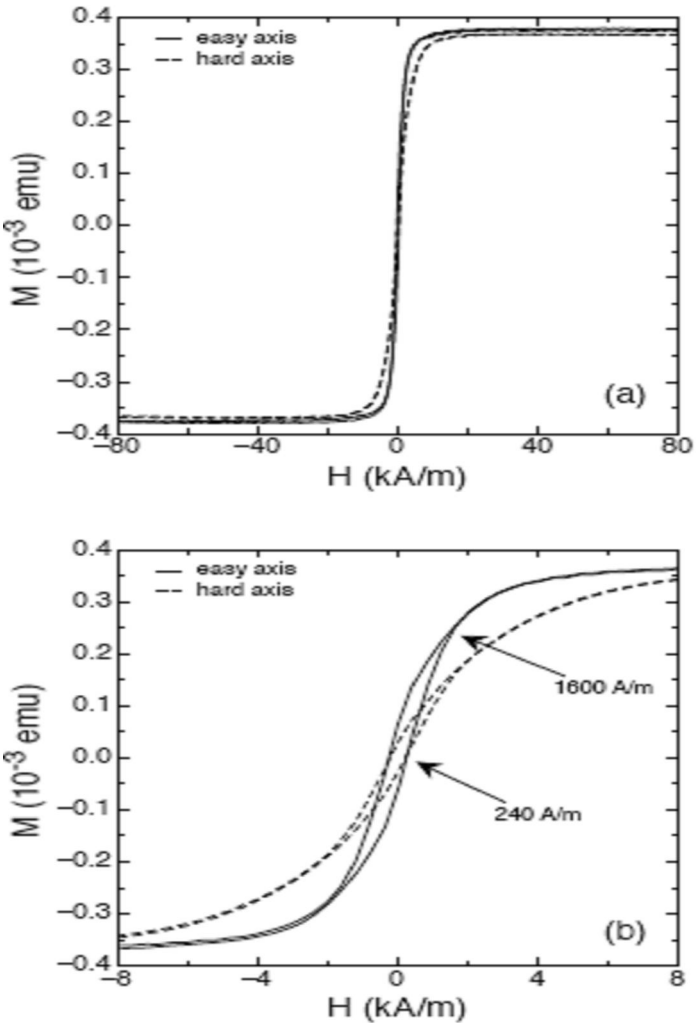

Figure 5.1.2: (a) Hysteresis loops on the F1000 sample along the easy and hard magnetization axes. **(b)** Magnification of the loops shown in **(a).**

The angular dependences of the coercive field for the two studied samples as obtained by the hysteresis loops measured at different angles by the VSM are reported in figure 5.1.3. Sample F500 clearly displays a uniaxial magnetic anisotropy, conversely a more complex behavior is observed for sample F1000. The presence of such anisotropy, indicating a preferential direction, is unexpected due to the amorphous state of both samples; however it has been previously detected in as-prepared samples [18].

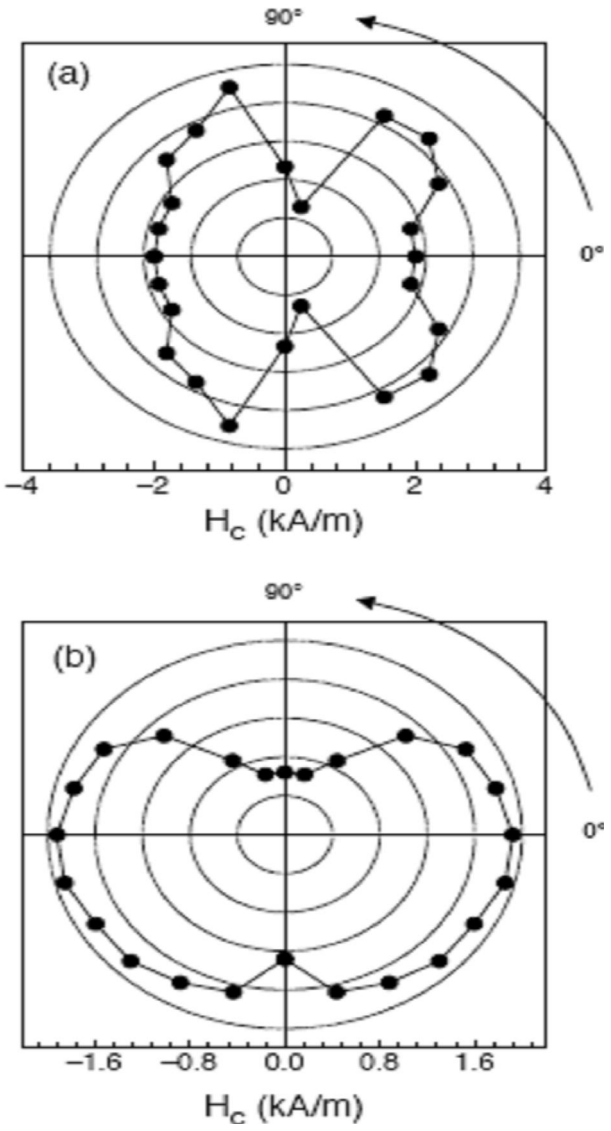

Figure 5.1.3: Polar plots of the coercive field for in-plane hysteresis loops measured at different applied field directions for **(a)** sample F500 **(b)** sample F1000.

Representative magnetization relaxation curves measured for the two samples are depicted in figure 5.1.4. The experimental data was fitted using stretched exponential curve. In both cases relaxation times turn out to be of the order of few tens of seconds. As expected relaxation time is seen to increase while approaching the coercive field value that indicates the uniaxial anisotropy value [19].

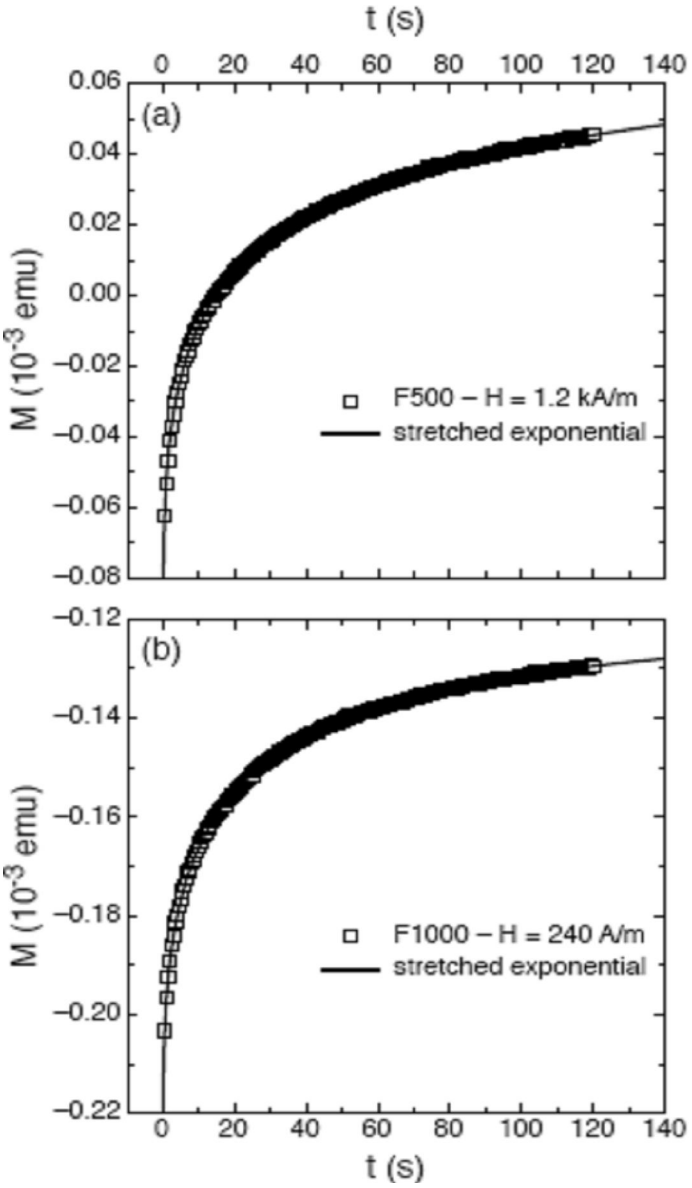

Figure 5.1.4: Stretched exponential fitting of the magnetization relaxation curve of **(a)** Sample F500 (b) Sample F1000

5.2 Magnetic properties of ion beam sputtered FeZrNbBCu thin films

5.2.1 Effect of annealing treatment on magnetic properties

Studies on magnetic properties of NANOPERM thin films can be useful as these can be potential candidates for the applications where high saturation magnetization is one of the major requirements. As described earlier in chapter 3 that thin film samples were prepared by ion beam sputtering on a silicon substrate using a target made by amorphous ribbons of nominal composition $Fe_{84}Nb_{3.5}Zr_{3.5}B_8Cu_1$. Samples were subjected to furnace annealing in vacuum (~ 4×10^{-4} mbar) at 200, 250, 300, 350, 400, 450, 500 and 550^o C for 80 minutes respectively in order to crystallize them. Magnetic hysteresis loops were measured on (1) IBS 190 12 min (2) IBS 190 24 min (3) IBS 190 36 min thin film samples using alternating gradient field magnetometer (AGFM, see appendix D) in as-prepared as well as annealed state by applying field in plane of the film along two orthogonal directions. Figure 5.2.1 shows the hysteresis loops measured on all the three samples in as deposited state. It can be seen that the loops displays a quite rectangular shape when measured along easy axis. This may be taken as an indication of presence of uniaxial anisotropy in the samples. In both the directions a detectable coercive field can be observed. Angular dependence of coercive field measured for three as deposited samples is depicted in figure 5.2.2. These measurements were obtained by the hysteresis loops measured by applying magnetic field in plane of the film samples at different angles using vibrating sample magnetometer (VSM, see appendix E). This supports the notion of presence of anisotropy in the samples. This may be ascribed to many factors including the quenched in stresses during deposition.

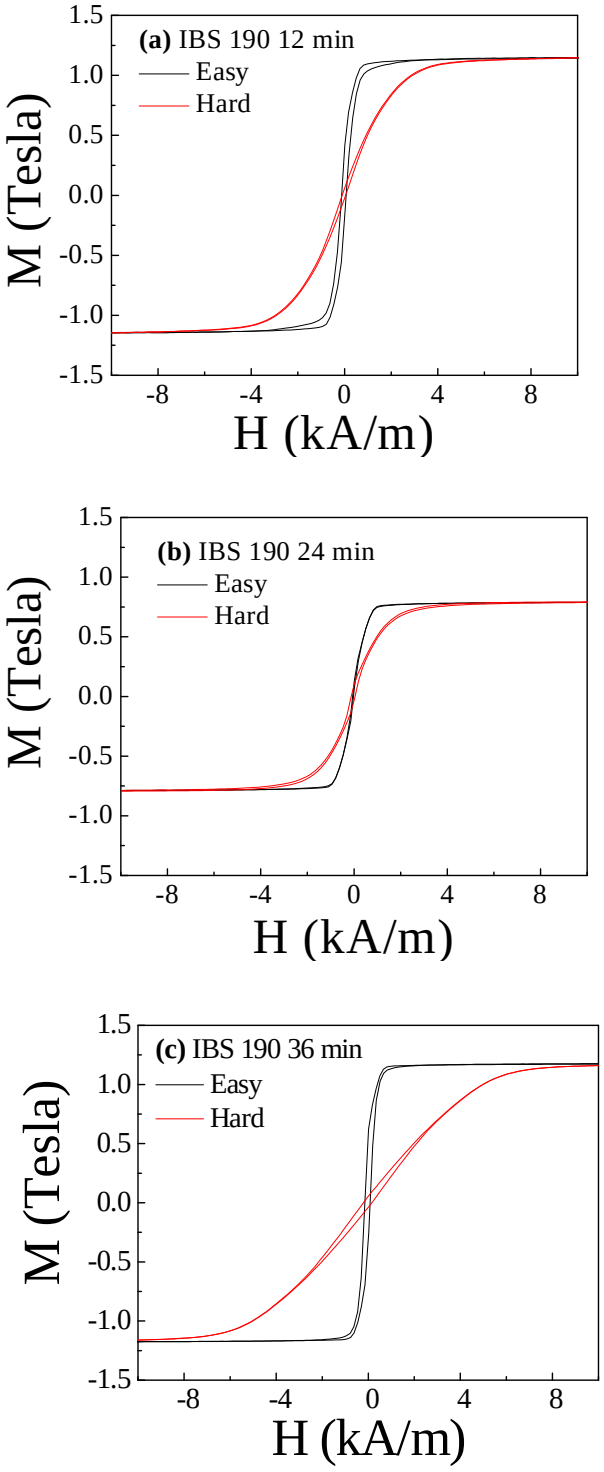

Figure 5.2.1: Hysteresis curves along two orthogonal directions for as deposited IBS samples

Substrate plays an important role in determining the preferential direction of magnetization. Silicon substrate is not amorphous and this can be a possible source of anisotropy. However it may be noted that as pointed out in our earlier studies that anisotropy is present despite of the amorphous nature of substrate material [18, 19]. It may be possible that the anisotropy is induced in a direction specifically relative to the direction of incident ion beam during deposition. Angular dependence of the ratio of remnance to saturation magnetization as obtained by VSM measurements is presented in figure 5.2.3 a, b, c respectively for the samples in as deposited state. The observed angular dependence suggests that all the three samples in as deposited state possess uniaxial anisotropy.

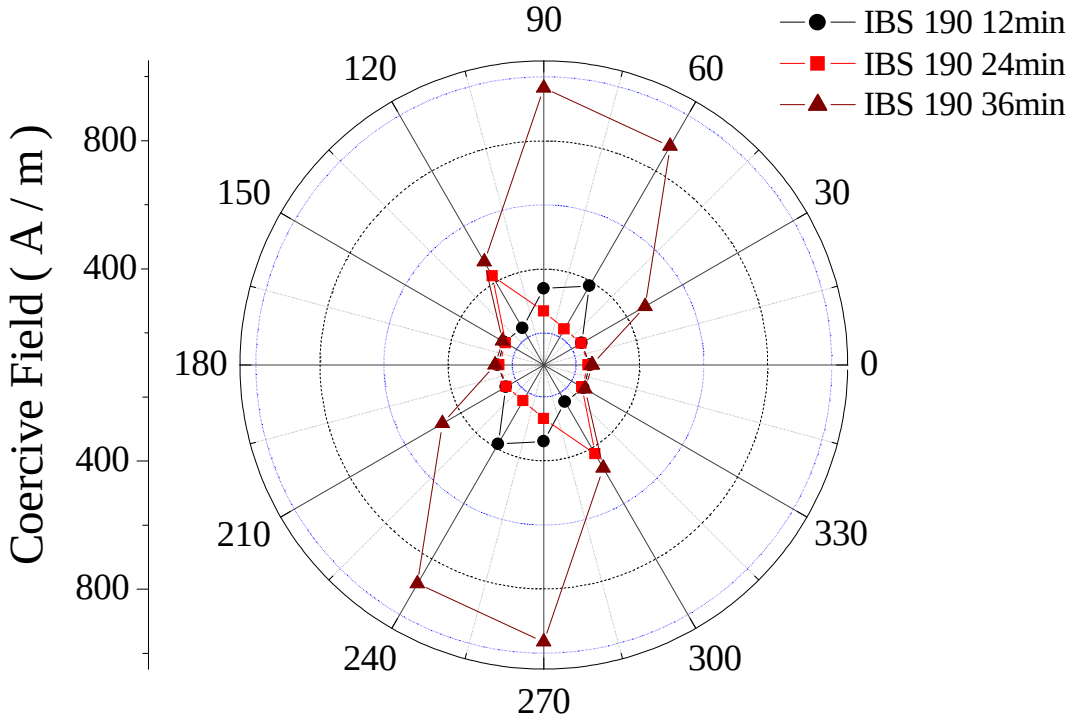

Figure 5.2.2: Angular dependence of coercive field for as deposited IBS 190 samples.

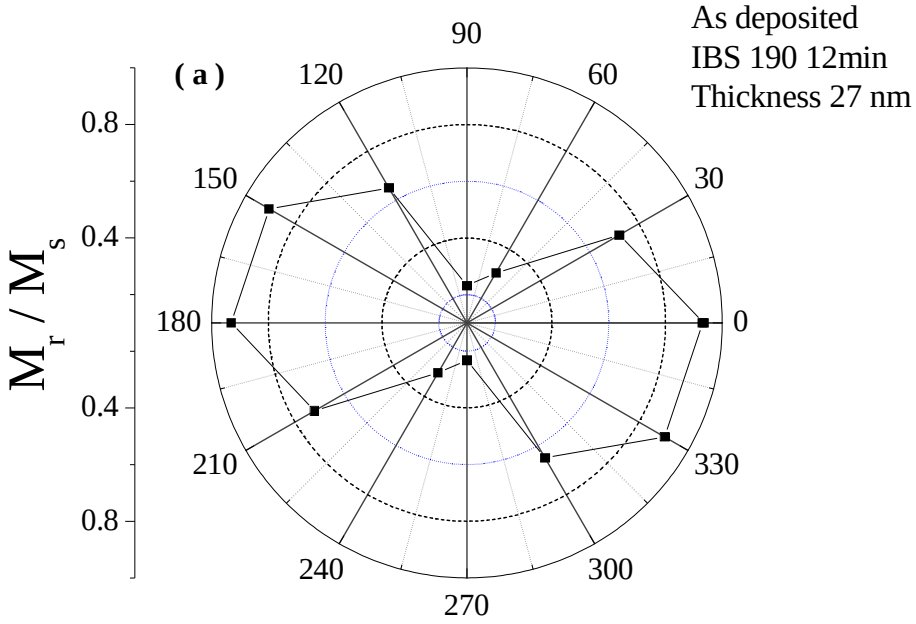

Figure 5.2.3 (a) Azimuthal angle dependence of reduced magnetization for as deposited IBS 190 12 min sample.

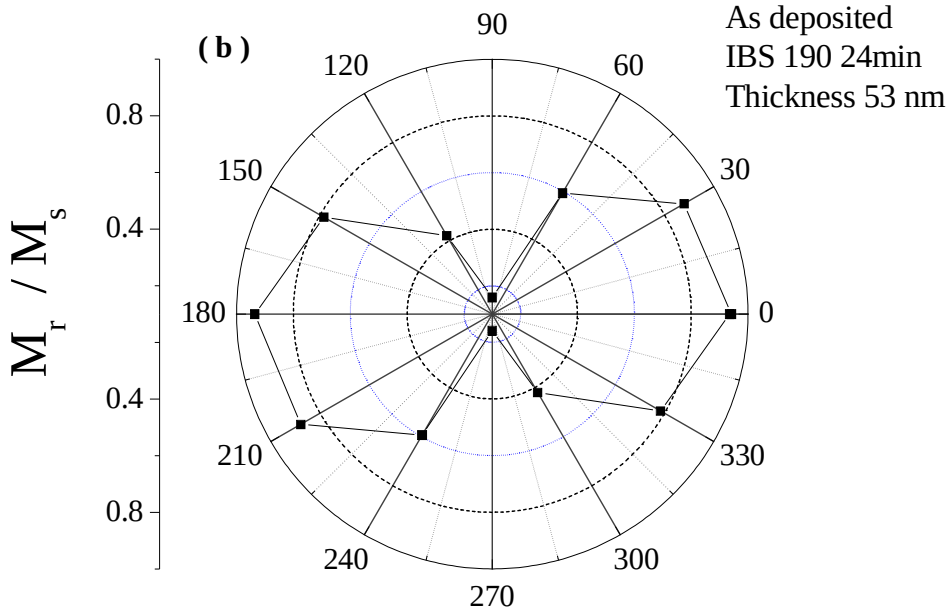

Figure 5.2.3: (b) Azimuthal angle dependence of reduced magnetization for as deposited IBS 190 24 min sample.

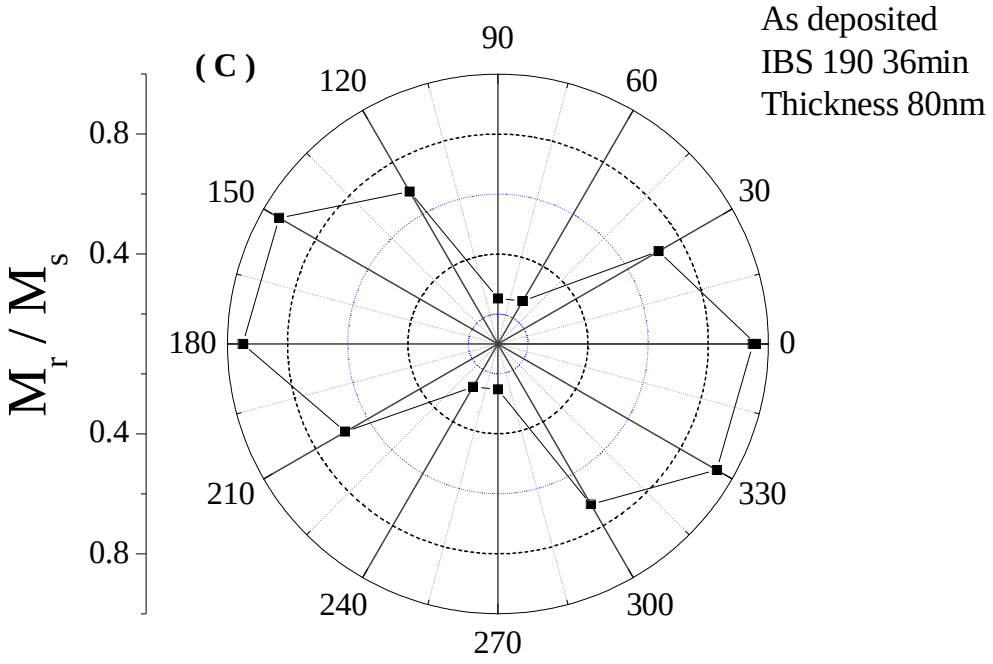

Figure 5.2.3: (c) Azimuthal angle dependence of reduced magnetization for as deposited IBS 190 36 min sample.

It may be said that the thin films samples in as deposited state can be identified with a system exhibiting the characteristics of Stoner Wohlfarth particle. The behavior as suggested by the polar plots is attributable to the existence of single domain state. It may also be noted that the easy axis of samples is tilted with respect to the direction of applied field and this is may be due to the orientation of samples was such that the easy axis was not exactly parallel to the applied field direction. The possible source of observed anisotropic behavior may be ascribed to the possible presence of some stray magnetic field present at the substrate during deposition. Quenched in internal stresses may also get coupled in order to give rise to a preferential orientation of magnetization in plane of the thin film samples [20]. It is also possible that variety of all such causes, may even act simultaneously. It is likely that quenched-in stresses during deposition may be a result of

magnetostrictive interactions induced by an external stress that can make certain magnetic directions energetically favored. Some chemical short-range ordering or inhomogeneity of the film thickness related to the ion beam direction may also be responsible for the observed presence of anisotropy [21]. Moreover it is difficult to say as to which one of the cause is the most probably responsible for the observed anisotropy in these films. It is important to remark that in principle shape anisotropy also plays a role. In the case of prisms, only approximate expressions for the demagnetizing coefficients are available [22] whereas our samples are approximately squares. However as in case of our samples, when thickness and lateral dimensions differ by many orders of magnitude, the demagnetizing fields in plane of samples are negligible with respect to the applied magnetic field. For this reason, the observed magnetic anisotropy of our samples cannot be ascribed to their square shape. Variation of coercive field along the easy direction of magnetization as a function of annealing temperature is included in the figure 5.2.4. Coercivity of the sample of thickness 80 nm shows a steady increase with annealing temperature. Coercivity for the three samples does exhibit smaller values for lower annealing temperatures Hysteresis curves of representative samples annealed at 550^{o}C for 80 minutes are presented in the figure 5.2.5. It may be interpreted that the annealing treatment seems to remove the anisotropy that was observed in as deposited samples. Annealing seems to increase the magnetic hardness. Coercive field as observed for annealed samples is greater than the anisotropy fields observed for as deposited samples and this might be a reason that the anisotropy no longer exists in annealed state. It may also be noted that the hysteresis curves measured along two orthogonal directions are no longer exhibiting difference in the shapes. The loop shape is approaching almost square corresponding to the samples in annealed state. This square

shape of loops may be considered as an indication of simultaneous increase of permeability in the region near to the coercive field and decrease in anisotropy. From figure 5.2.4 it may be noted that the coercive field for the least thick sample (IBS 190 12 min) is minimum at the highest annealing temperature. However for higher annealing temperatures coercivity increases sharply. As reported earlier in the chapter 3 (Table 3.2.2) that the grain size is independent of thickness and annealing treatment. So dependence of coercivity on grain size is not at all strong. This can be ascribed to the structural relaxation and the relaxation of quenched in stresses. Whereas it can be observed from atomic force microscopy images (see figure 3.3.3) that the surface roughness does increase with annealing temperature. Surface roughness increases because the amount of crystallites is expected to increase with temperature that form aggregates.

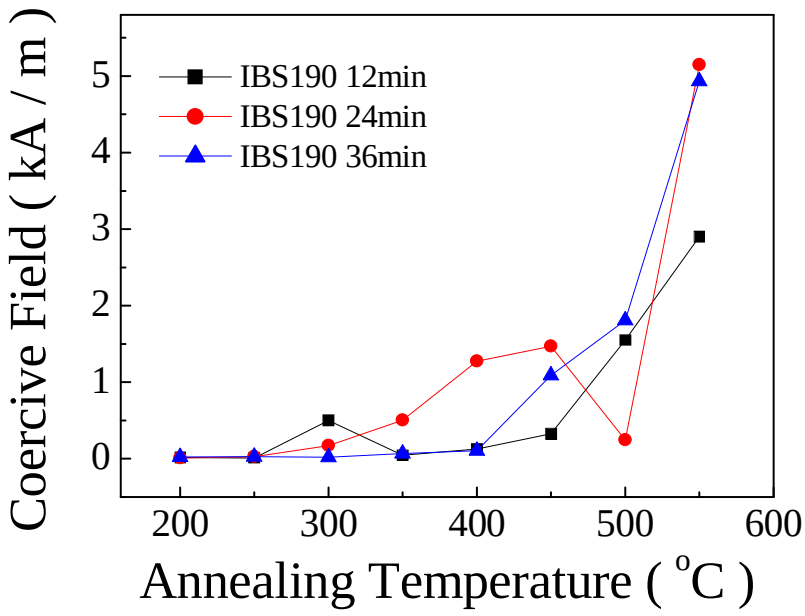

Figure 5.2.4: Annealing temperature dependence of coercive field for IBS 190 samples annealed at various temperatures for 80 minutes.

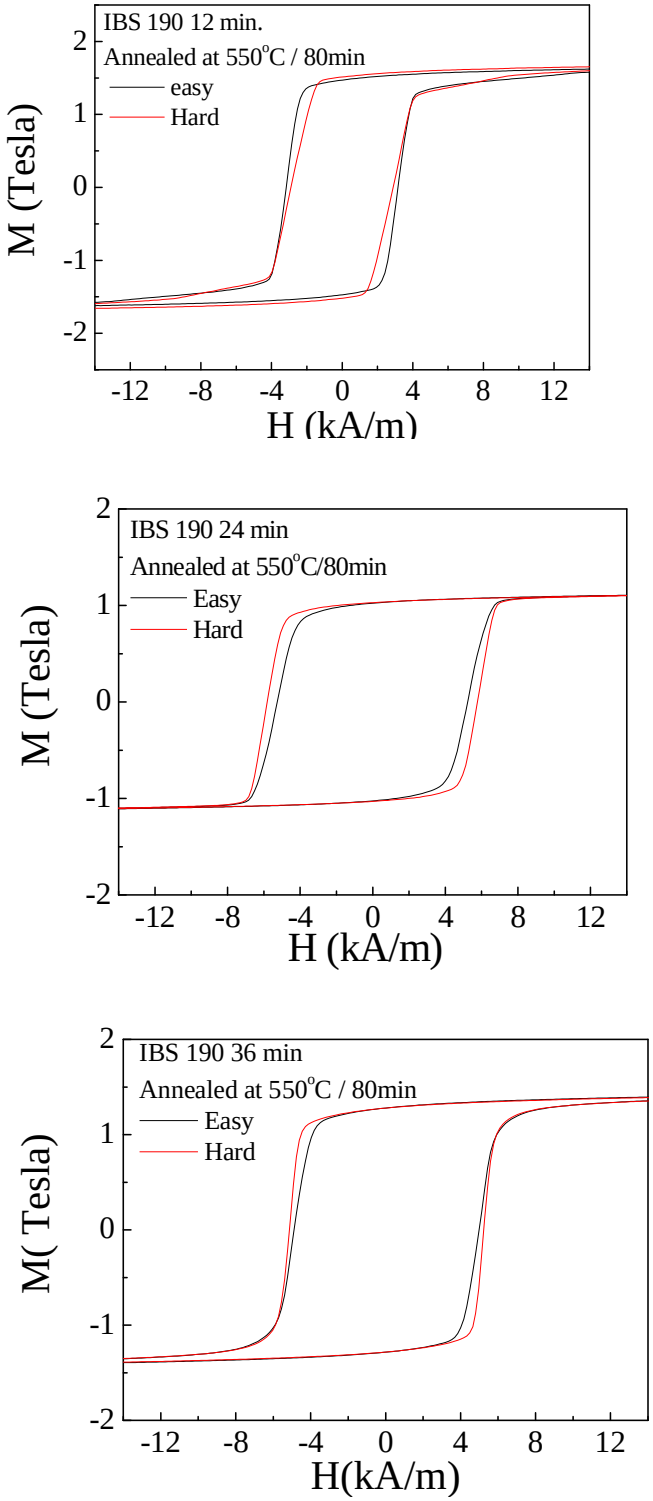

Figure 5.2.5: Representative hysteresis loops along two orthogonal directions for IBS 190 samples annealed at 550°C for 80 minutes.

It may be possible that these aggregates on the surface of thin film samples are acting as pinning centers and thereby hindering the domain wall motion, resulting in increasing value of coercive field. The coercivity behavior for the thin film samples is quite different than that is exhibited by bulk ribbon samples annealed at temperatures above 500^{o}C. It may be possible that the film thickness is either comparable or greater than the ferromagnetic exchange length corresponding to the crystalline state (~ 20 nm). This eventually decreases the number of exchange coupled grains which results in an effective increase of magnetocrystalline anisotropy. Figure 5.2.6 shows the variation of saturation magnetization for IBS 190 samples with annealing temperature. The value of saturation magnetization almost remains constant except small increase towards higher annealing temperature which may be considered as a sign of increasing permeability. The increase in permeability is also manifested in terms of the shape of the hysteresis curves measured on annealed samples. Saturation magnetization varies quite far for the least thick sample but it may be attributed to the contribution from the error in thickness and surface area measurements. The thickness of the samples IBS 190 24 min sample is might be overestimated as the magnetization value in annealed state is comparatively smaller to the other two samples. Large variations in the value of saturation magnetization for the least thick samples can be observed. It may be attributable to the inhomogenous deposition during sputtering. This sample might have large fluctuations in the thickness during deposition and also the interface effects are stronger as the thickness is comparatively smaller. Even the thickness of oxide layer may affect the magnetization response strongly in the case of IBS 190 12 min sample. Similarly surface area of the samples were determined on the basis of the reflectivity and the least thick sample may be comparatively transparent which gives rise to

large fluctuations in the magnetization values scaled on the basis of volume of the sample. Moreover the saturation magnetization does not vary strongly with annealing temperature exhibiting an average value about 1.4 T for IBS 190 12 min and IBS 190 24 min samples. This value is quite similar to the one observed for the bulk composition. This also may be considered as an indication that the composition of nanocrystalline phase in thin film samples is same as that of bulk composition.

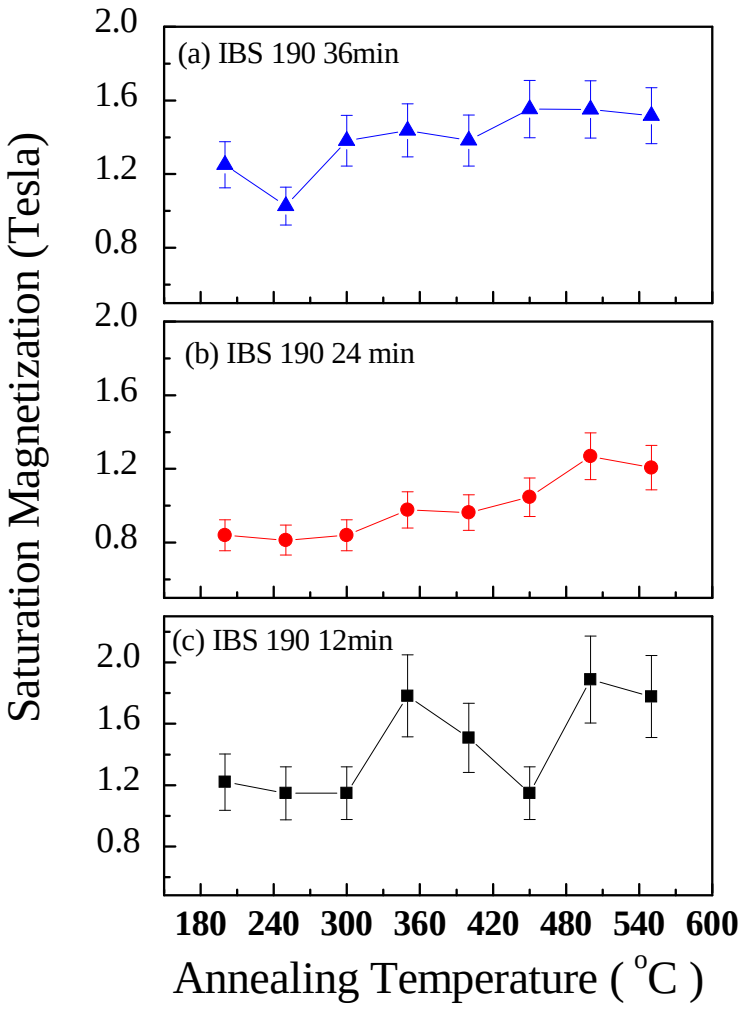

Figure 5.2.6: Annealing temperature dependence of saturation magnetization for IBS 190 samples annealed at various temperatures for 80 minutes.

5.2.2 Ferromagnetic resonance measurements

(a) Introduction

Ferromagnetic resonance (FMR) absorption is the analog of paramagnetic and nuclear resonance absorption. This effect was originally found by Griffiths [23-25]. Further confirmatory studies were reported by Yager and Bozorth through a typical experimental arrangement where they used a thin sheet or foil of the ferromagnetic specimen as one wall of a rectangular cavity terminating a wave guide fed by a microwave generator [26]. Applied microwave field was constant in direction in the plane of wall. A static magnetic field was also applied in the plane of the wall but in a direction perpendicular to the microwave field. It was observed that the energy loss in the cavity goes through a maximum with increasing static magnetic field. The resonance condition for plane surface was given as: $\nu_0 = \gamma (B H)^{1/2}$, where ν_0 is the frequency of applied microwave field at resonance, γ the magneto-mechanical ratio for an electron spin, H is strength of applied static magnetic field and B is the magnetic induction in the specimen [24]. Ferromagnetic resonance (see appendix F) absorption is a phenomenon that is widely used in studying ferromagnetic thin films because of their high applicative importance. FMR is extremely informative method to study magnetic thin films because parameters of FMR depend mostly on the properties of the thin film which have various physical origins. However comprehensive characterization of ferromagnetic materials encompasses study of various kinds of anisotropy, phase transitions with respect to magnetic field, domain wall motion etc [27]. Magnetic anisotropy evaluation is a task of extreme importance for most thin film applications. For example the development of a perpendicular anisotropy is of great interest for data storage devices [28]. In particular, from view point of the high frequency

performance of soft magnetic thin films has become more important due to the continued need to increase the storage density in magnetic disk drives. Moreover, as it is possible to control a well defined anisotropy in soft magnetic thin films, FMR studies on such media become more relevant from both application and fundamental view point [29, 30]. FMR studies allow the investigation of the anisotropy field distributions in magnetic materials and magnetization reversal and damping processes that can be useful for the conception of the devices like microwave tuners, absorbers or inductors based on such materials [31].

(b) Anisotropy field determination using Ferromagnetic resonance measurements on as deposited samples

The ferromagnetic resonance effect has been studied by measuring the spectra at different applied magnetic fields on ion beam sputtered samples (3mm× 3mm) in as deposited state using vector network analyzer ferromagnetic resonance technique. Schematic of the experimental arrangement is presented in figure 5.2.7. The vector network analyser FMR technique allows for operation over a wide range of frequency and yields FMR parameters from standard microwave *S*-parameter measurements versus frequency and field. As shown in figure 5.2.7 FMR has been measured by placing the samples face down on a micro strip line that is connected to vector network analyzer. This micro strip line is basically serving the purpose of a coplanar waveguide (CPW) excitation structure that provides the microwave drive. This is indicated as center conductor across which the thin film sample is positioned. The static magnetic field is provided by a set of Helmholtz coils. The static field was applied in the plane of the film and perpendicular to the microwave field. The setup was then used to obtain the standard microwave *S* parameters as a function of frequency at

a fixed field for the CPW line with the sample in place. A reference state is defined by saturating the thin film sample by applying a saturating filed in the plane of the film. For each value of applied static magnetic field the ration of transmission parameter (S) corresponding to applied field and to reference state is calculated. Absorption peaks were then detected in order to estimate the resonance frequencies at different applied static field. Data were collected for each sample with a maximum applied static magnetic field of 40 kA / m. Depending on the film thickness and applied field value ferromagnetic spectra can display one or more absorption peaks indicating the occurrence of ferromagnetic resonance. The peak value shifts towards higher frequency values as the applied field is increased. In order to understand the origin of the occurrence of FMR for the studied specimens the frequency corresponding to which absorption peak occurs is plotted as a function of applied magnetic field for the three as deposited sample in figure 5.2.8.

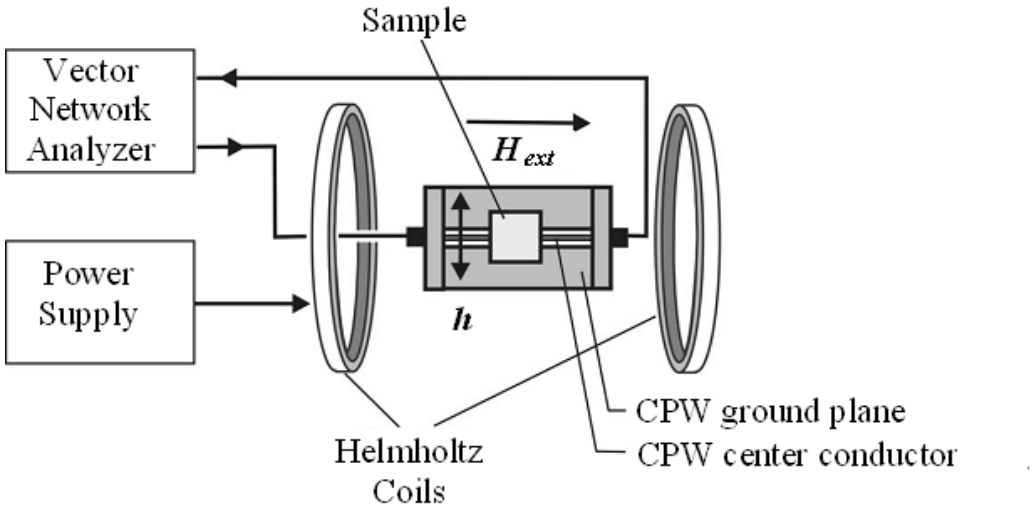

Figure 5.2.7: Schematic diagram of the vector network analyzer ferromagnetic resonance spectrometer. The sample is placed on the coplanar waveguide (CPW) structure, as indicated. The mutually perpendicular static applied field H_{ext} and the microwave field h are in the plane of the film sample.

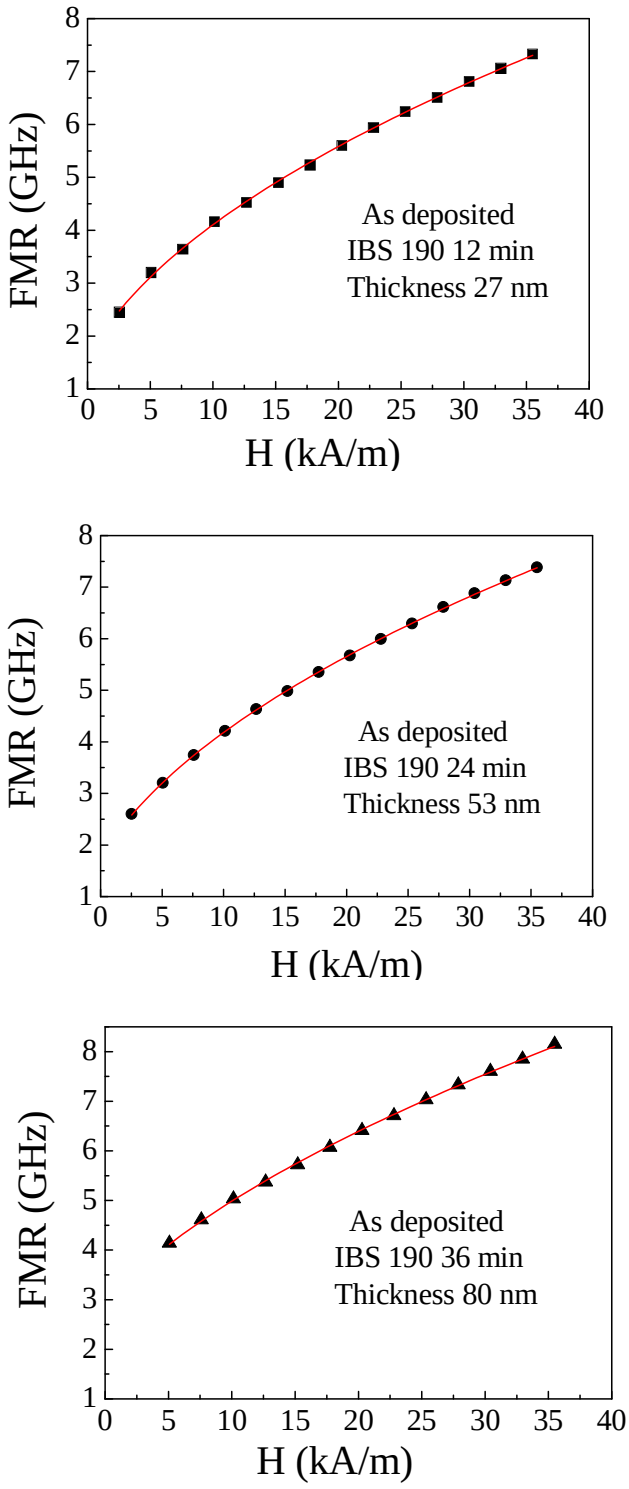

Figure 5.2.8: Field dependence of the FMR frequency for as deposited IBS 190 samples (symbols) and Fit according to equation 5.2.1 (red line).

According to Kittel theory of ferromagnetic resonance the field dependence of the FMR frequency in thin film systems is given by [24, 25]:

$$f = \frac{\gamma \mu_0}{2\pi} \sqrt{(H + H_k - N M_s) M_s} \qquad \textbf{(5.2.1)}$$

Where γ is the gyro magnetic factor (~ 1.76×10^{11} Hz / T), H is the applied magnetic field, H_k is the magnetic anisotropy field, N is the demagnetizing factor along the direction of applied magnetic field and M_s is the saturation magnetization of the sample. However it should be noted here that in the case of our samples where thickness and lateral dimensions differ by many orders of magnitude the demagnetizing fields in plane calculated using approximate expressions available [22] are negligible with respect to the applied magnetic field. The best fit procedure using equation 5.2.1 was performed with M_s and H_k being considered as free parameters. It can be seen in figure 5.2.8 this fitting (red solid line) procedure is able to reproduce the experimental data quite consistently for the thin films of three different thicknesses under investigation. The values of M_s and H_k obtained by fitting the experimental data are represented in Table 5.2.1 which also depicts the corresponding values that were obtained from the measured hysteresis loops on as deposited samples. The two sets of values shows a good agreement indicating that meaningful values of M_s and H_k are obtained that reproduces the experimental data. This indicates that the magnetization is lying in plane of the films and the anisotropy increases with thickness.

Table 5.2.1: M_s and H_k values obtained by experimental data and fit using Kittel's formula.

Sample	***Thickness***	***Ms* (T) (Fitting)**	***Ms* (T) (loops)**	**H_k (kA/m) (Fitting)**	**H_k (kA/m) (loops)**
IBS 190 12 min	27 nm	1.15	0.9922	1.744	1.910
IBS 190 24 min	53 nm	1.16	0.8479	2.060	2.388
IBS 190 36 min	80 nm	1.29	1.3293	5.514	5.970

5.3 Magnetic properties of RF sputtered FeZrNbBCu thin films

Thin film samples produced by RF sputtering as described in chapter 3 earlier were investigated using VSM and AGFM. Samples of dimensions 3mm× 3mm were studied in as deposited state first which were amorphous as also confirmed by X-ray diffraction measurements. These samples were then annealed in furnace at various temperatures for 60 minutes under vacuum in order to obtain nanocrystallized samples. As deposited samples were studied using VSM in order to observe the magnetization behavior as function of temperature. Magnetization versus temperature observations was registered in order to be able to have an idea of crystallization behavior of samples.

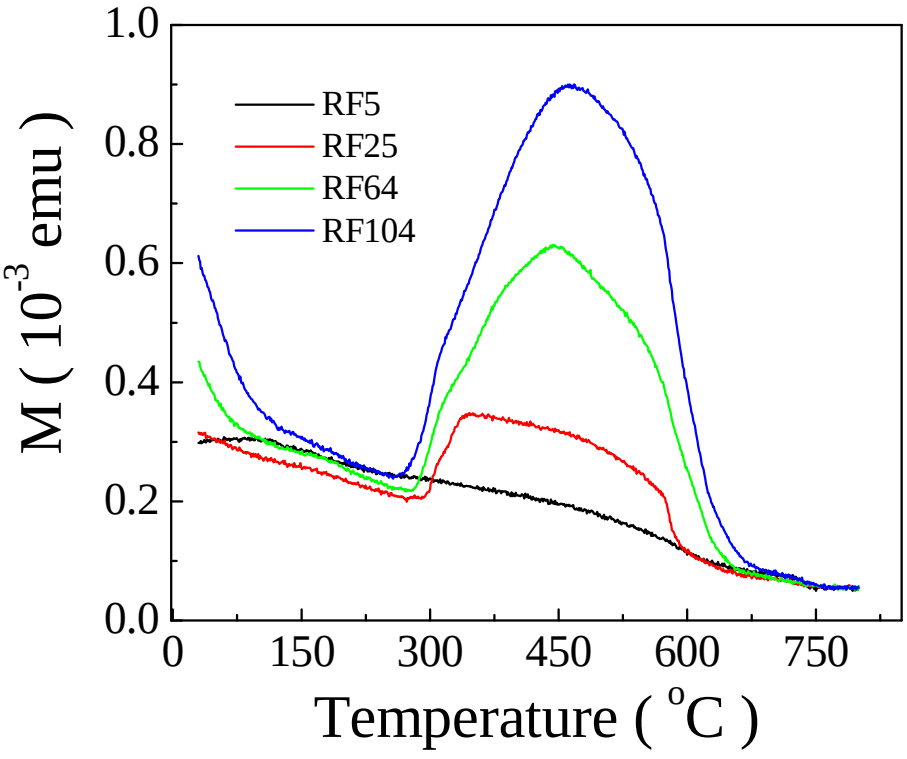

Figure 5.3.1 Magnetization versus temperature behaviour for the thin film samples of thickness 5, 25, 64 and 104 nm prepared using RF sputtering.

Figure 5.3.1 presents the magnetization as a function of temperature for representative samples with thickness 5, 25, 64 and 104 nm. It may be seen that the curie temperature of amorphous phase (~ 90^{o}C) is just above the Curie temperature observed for the bulk ribbons (~ 70^{o}C) which were used to sputter these thin film samples. It may also be observed that the value of magnetization for all samples peak around 460^{o}C. This indicates that the peak crystallization occurs within a range of temperature around 460^{o}C. This value of peak crystallization temperature is less than that was observed in case of bulk amorphous ribbons of same composition. This also indicates that the thin films are thermally less stable as compared to the bulk composition in form of amorphous ribbons. It may also be noted that the curie temperature of crystalline phase is varying with the thickness of sample e. g for the 5 nm thick sample the curie temperature is about 150^{o}C less than that for the thickest sample (104 nm). In order to see whether the samples possess some preferred direction of magnetization orientation or not AGFM was used to measure the magnetization versus applied magnetic field behavior of as deposited samples. Figure 5.3.2 shows the representative hysteresis loops measured on the thinnest and the thickest sample from the set. The loops were measured by applying a magnetic field in the plane of the thin film samples along two mutually perpendicular directions as indicated. It may be inferred from the figure 5.3.2 that the samples are not exhibiting any anisotropy. The magnetization variation with applied field along two mutually orthogonal directions is quite similar which suggests that the thin film samples prepared by RF sputtering are free from anisotropic behavior. We have used the glass substrate for the deposition of these thin film samples so amorphous and hence the isotropic nature of the samples was expected. However it should be noted that in one of our earlier studies [19] thin film samples prepared by using glass

substrate exhibited anisotropic behavior in as deposited state. On the basis of hysteresis measurements done using AGFM the variation of coercive field and saturation magnetization of as deposited samples with thickness is shown in figure 5.3.3 a and b respectively.

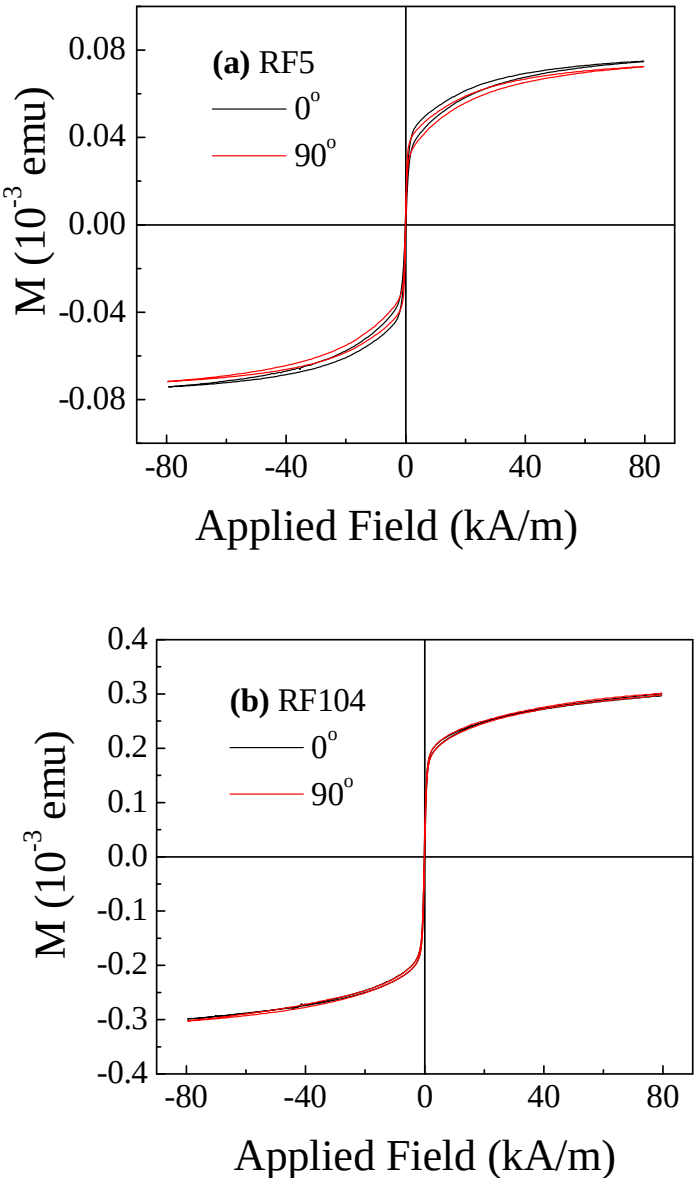

Figure 5.3.2: Representative hysteresis curves for as deposited samples prepared by RF sputtering with thickness **(a)** 5 nm **(b)** 104 nm.

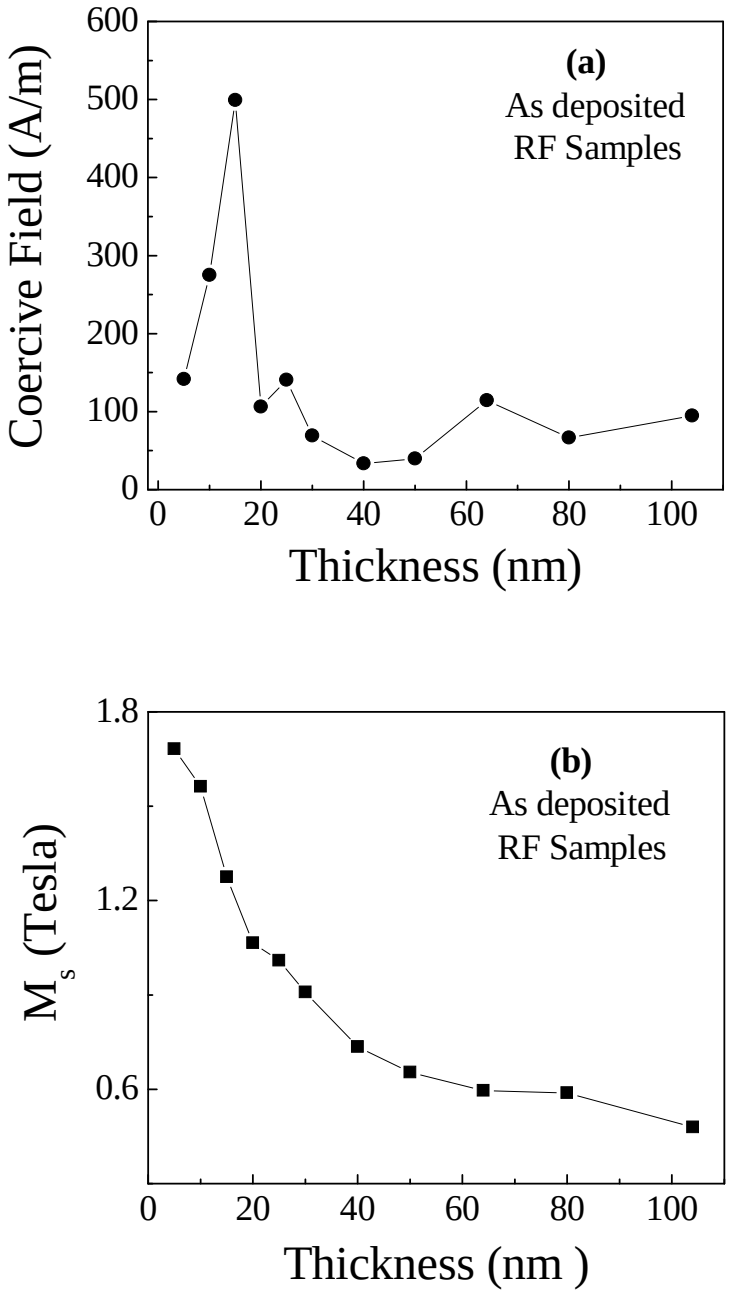

Figure 5.3.3: Variation of **(a)** coercive field **(b)** saturation magnetization as a function of thickness of as deposited samples prepared by RF sputtering.

Sample of thickness 15 nm shows the highest value of coercivity whereas the minimum value of coercive field is exhibited by the sample of thickness 40 nm. The initial increase in coercivity with thickness up to 15 nm may be ascribed to the possibility of appearance of some granular structures during deposition which may act as pinning centers. It may be inferred that the as deposited samples are not fully amorphous and there is also a possibility of inhomogeneous deposition that give rise to a rough surface. As compared to the as deposited samples prepared by ion beam sputtering method, RF sputtered thin film samples are expected to exhibit higher degree of roughness on surface.

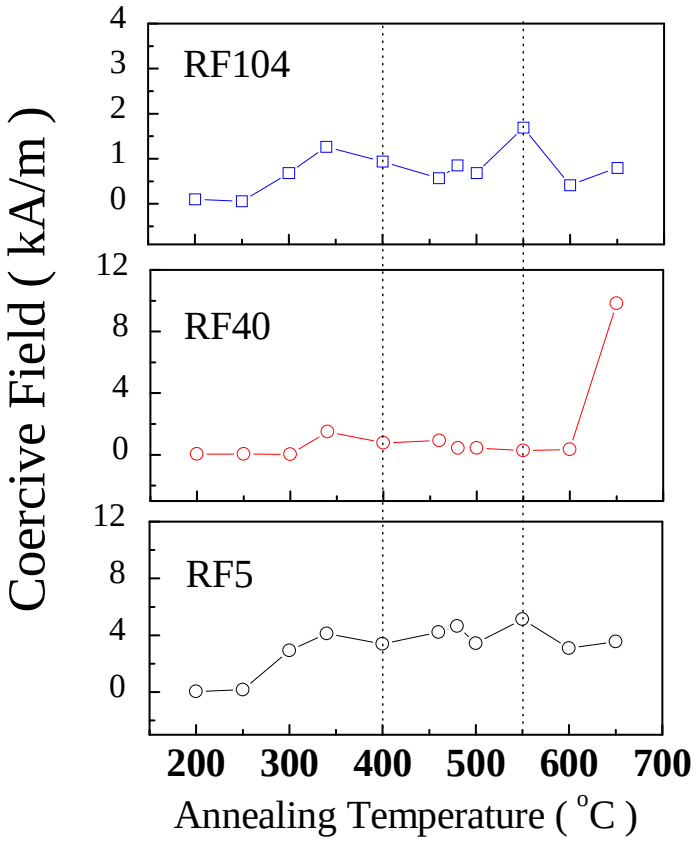

Figure 5.3.4: Annealing temperature dependence of coercive field for the annealed samples of thickness 5, 40 and 104 nm.

As shown in figure 5.3.4 the coercive field varies quite similarly for the samples indicated between the annealing temperatures of 400 to 550^{o}C except for the sample of thickness 40 nm which exhibited a sharp increase in coercive field values when annealed at temperatures higher than 600^{o}C i.e. the Curie temperature of crystalline phase approaches. This might weaken the magnetic coupling among nanocrystallites. Variation of saturation magnetization with annealing temperature for the samples of thickness 5, 40 and 104 nm is shown in figure 5.3.5. Effectively the saturation magnetization increases with annealing temperature till 600^{o}C which indicates the increase in the amount of crystalline phase that is precipitating out.

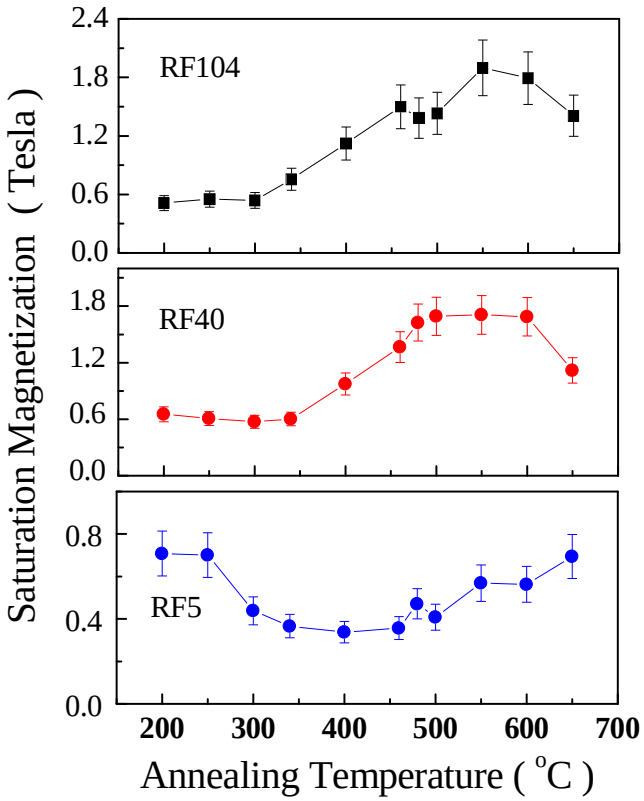

Figure 5.3.5: Variation of saturation magnetization with annealing temperature for samples of thickness 5, 40 and 104 nm.

Although a decrease in magnetization for thinnest sample between the 300 to 450°C is observed. Apart form the error introduced in the determination of the thickness and the surface area of the sample, this decrease might be due to the much smaller thickness so that the sample is not getting optimally crystallized as compared to thicker samples. On the other hand the peculiar coercivity behviour of the sample of thickness 15 nm can be seen as a function of annealing treatment in figure 5.3.6. It also depicts the coercive field variation for samples of thickness 25 and 64 nm. The variation of coercive field for the sample RF25 is quite similar to that of the sample RF40.

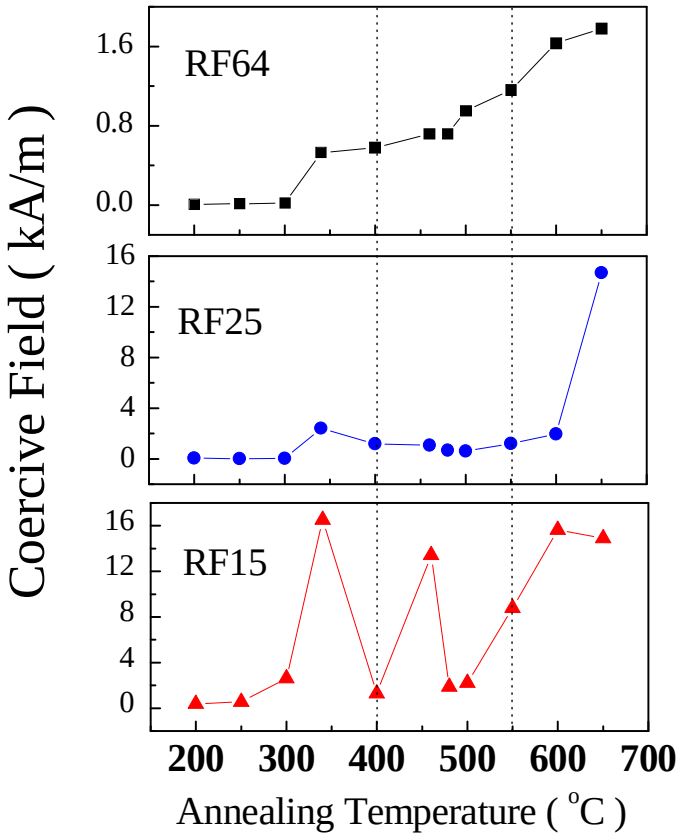

Figure 5.3.6: Annealing temperature dependence of coercive field for the annealed samples of thickness 15, 25 and 64 nm.

Both these samples show a sharp increase in coercivity for annealing temperatures higher than 550°C. Whereas for the sample RF64 coercive field increases steadily with annealing temperature. It is quite interesting to note the variation of saturation magnetization of the sample of thickness 15 nm, as shown in figure 5.3.7, is qualitatively very similar to that of the RF5 sample. Figure 5.3.7 also depicts that for RF64 sample saturation magnetization value increases steadily, whereas there is decrease in the value of saturation magnetization is exhibited eventually in case of other sample above the annealing temperature of 550°C.

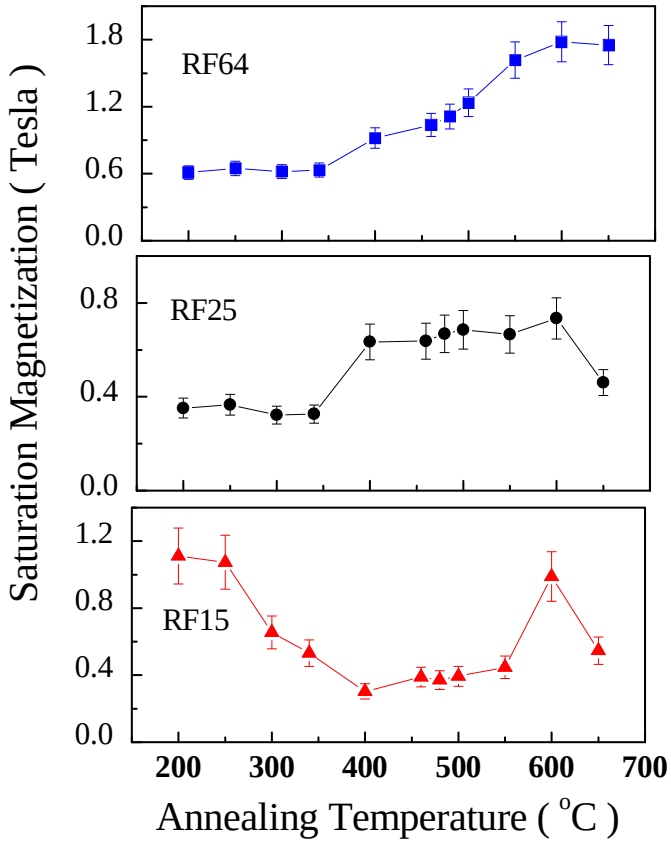

Figure 5.3.7: Variation of saturation magnetization with annealing temperature for samples of thickness 15, 25 and 64 nm.

References:

[1] N. Hasegawa, M. Saito, J. Magn. Soc. Japan 14 (1990) 313.

[2] K. Yamaguchi, S. Ohnuma, T. Imagawa, J. Toriu, H. Matsuki, IEEE Trans. Magn. 29 (1993) 2232.

[3] K. H. Kim, Y. H Kim, J. Kim, S. H. Han, H. J. Kim, J. Appl. Phys. 87 (2000) 5248.

[4] Okumara et al. J. Appl. Phys. 93 (2003) 6528.

[5] P. Sharma, H. Kimura, A. Inoue, J. Appl. Phys. 100 (2006) 083902-1.

[6] S. D. Yoon et al. J. Appl. Phys. 103, (2008) 063917-1.

[7] G. Herzer, IEEE Trans. Magn. 25 (1989) 3327.

[8] M. Yamaguchi *et al.*, J. Appl. Phys. 85 (1999) 7919.

[9] K. Suzuki, A. Makino, N. Kataoka, A. Inoue, T. Masumoto, Mater. Trans. JIM 32 (1991) 93.

[10] K. Suzuki, A. Makino, A. Inoue, T. Masumoto, J. Appl. Phys. 70 (1991) 6232.

[11] A. Makino, A. Inoue, T. Masumoto, Nanostruct. Mater. 6 (1995) 985.

[12] A. Makino, T. Hatanai, Y. Naitoh, T. Bitoh, A. Inoue, T. Masumoto, IEEE Trans. Mag. 33 (1997) 1397.

[13] G. Peto, I. Szabo, E. Kisdi-Koszo, E. Zsoldos, L. Guczi, P. Kollar, 140-144 (1995) 425.

[14] A. Neuweiler, H. Kronmuller, J. Magn. Magn. Matr. 177-181 (1998) 1269.

[15] R. Grossinger and H. Sassik, J. Magn. Magn. Mater. 41(1984) 107.

[16] S. N. Kane, N. Bhagat, A. Gupta, and L. K. Varga, J. Magn. Magn. Mater.167(1997) 241.

[17]M. V. Sedova et al. J. Non-Crystalline Solids 287 (2001) 104.

[18] P. Sharma and A. Gupta, J. Magn. Magn. Mater. 288 (2005) 347.

[19] F. Celegato, M. Coïsson, A. Magni, P. Tiberto, and F. Vinai, S. N. Kane, S. S. Modak, A. Gupta, P. Sharma, J. Appl. Phys. 102, (2007) 043916-1.

[20] M. R. J. Gibbs, P. T. Squire, A. Hayes, J. H. Vincent, J. Appl. Phys. 64 (1988) 5419.

[21] Y. Suzuki, J. Haimovich, T. Egami, Phys. Rev. B 35 (1987) 2162.

[22] A. Aharoni, J. Appl. Phys. 83 (1998) 3432.

[23] J H. E. Griffiths, Nature 158 (1946) 670.

[24] C. Kittel, Phys. Rev. 71 (1947) 270.

[25] C. Kittle, Phys. Rev. 73 (1948) 155.

[26] W. A. Yager, R. M. Bozorth, Phys. Rev. 72 (1947) 80.

[27] B. Lax, K. J. Button, Microwave ferrites and ferrimagnetics, McGraw-Hill, N. Y. (1962).

[28] S. Khizroev, D. Litvinov, Perpendicular Magnetic Recording, Kluwer Academic, Dordrecht (2004).

[29] C.B. Craus, A.R. Chezan, D.O. Boerma, L. Niesen, J. Phys.: Cond. Matter 16 (2004), 9227-9241.

[30] J.M. Barandiaran, A. Garc´ıa-Arribas, D. de Cos, J. Appl. Phys. 99 (2006), 103904.

[31] G.V. Kurlyandskaya, S.M. Bhagat, C. Luna, M. Vazquez, J. Appl. Phys. 99 (2006), 104308.

Conclusions

The first half of the presented work considered the structural, magnetic and magneto-transport properties of amorphous and nanocrystalline ribbons of nominal composition $Fe_{84}Nb_{3.5}Zr_{3.5}B_8Cu_1$. Investigation of the evolution of nanocrystallization was performed thermally by using differential scanning calorimetry, thermo-gravimetric analysis and micro-structurally by X-ray diffraction technique (XRD) and Mössbauer spectroscopy measurements. Information on magnetic properties was obtained by quasi static hysteresis measurements done using single sheet testing technique. Complementary information on anisotropy field distribution is obtained by recording the second harmonic response of magnetization. Both XRD and Mössbauer measurements reveal that nanocrystallization starts after annealing of the specimen at 470^{o}C exhibiting the formation of Fe-rich phase with the presence of small amount of boron in the crystalline phase and the residual amorphous matrix. Grain diameter of the nanocrystalline phase ranges between 7 to 10 nm while volume fraction ranges between 15 to 48 %. With increasing annealing temperature, the increase of volume fraction is faster as compared to the growth of the nanograins. Variation of grain size and lattice constant with annealing temperature suggest that the microstructural composition is independent of annealing temperature as well as the duration of annealing after 490^{o}C. For annealing temperatures higher than 490^{o}C only crystalline volume fraction increases considerably. The annealing time and temperature seem to affect the extent of the crystallization more which eventually affects the coercive field considerably. The lowest value of coercive field 6 Am^{-1} is obtained after annealing the sample at 530^{o}C for 1 hour (corresponding saturation magnetization value is 1.4 T), attributed to the increased exchange coupling between the nanograins. Variation of coercive

field with grain size and volume fraction does not indicate any reasonable power law dependence except that the coercive field varies more strongly with crystalline volume fraction as compared to that with average grain size.

The anisotropy field distributions studies on $Fe_{84}Nb_{3.5}Zr_{3.5}B_8Cu_1$ ribbons indicated a systematic variation of anisotropy field with annealing temperature. Anisotropy field decreases quite smoothly with annealing temperature and the origin of the observed anisotropy field behavior may be attributed to the presence of annealing induced anisotropies beside the random magneto-crystalline anisotropies. Direct measurement of effective anisotropy and hence the anisotropy field is not straightforward but as the peak corresponding to anisotropy field were quite clearly defined which indicates the utility and efficiency of the experimental method followed in this work.

$Fe_{84}Zr_{3.5}Nb_{3.5}B_8Cu_1$ ribbons were also characterized by magneto-transport properties that can be tailored by choosing the proper annealing temperature or time. Samples annealed at temperatures around 490°C display significant variations of both coercivity and giant magneto impedance (GMI) response. For all samples enhanced GMI effect, below 30 MHz, is observable for the state when a considerable amount of exchange coupled nanocrystallites are developed in the amorphous matrix.

Grain size and volume fraction dependence of coercive field based on the Neel's theory of domain wall pinning is presented. This described well the magnetic behavior of studied $Fe_{58}Co_{25}Nb_7Cu_1B_9$ nanocrystalline alloy in the form of ribbons. On the basis of the good agreement obtained between experiment and the approach based on domain wall pinning process, it is inferred that the magneto-crystalline anisotropies are not randomly averaging out over the length scale determined by nanocrystalline phase. Rather the amorphous phase

determines correlation length scale that governed the observed magnetic behavior. It may be said that the magnetic properties seem to have a less strong dependence on the average grain size with($D^{3/2}$dependence) respect to the one expected on the basis of arguments proposed in the framework of random anisotropy mechanism (D^6 dependence) for nanocrystalline alloys.

The next set of studies was carried out in order to obtain information of structure and magnetic properties of thin films prepared by using $Fe_{84}Zr_{3.5}Nb_{3.5}B_8Cu_1$ amorphous alloy. Thin film samples were prepared by ion beam sputtering method and RF sputtering method by using target made by amorphous ribbons of nominal composition $Fe_{84}Zr_{3.5}Nb_{3.5}B_8Cu_1$. Thin film samples were annealed in vacuum furnace in order to induce crystallization. Micro structural studies on as deposited and annealed thin film samples were done using X-ray reflectivity, Grazing angle X-ray diffraction and atomic (magnetic) force microscopy technique. Vibration sample magnetometer and alternating gradient field magnetometer were used to study the temperature dependent and applied field dependent magnetization behavior of thin film samples respectively. Crystallization and Curie temperature of the thin films are comparable to those of the amorphous ribbons used as targets for the sputtering process, indicating that the composition of the resulting thin films is comparable to that of the ribbons. All thin film samples were characterized by an in plane magnetization. The ion beam sputtered thin film samples were identified with an in plane uniaxial anisotropy in as deposited state that may be ascribed to the preparation technique and the coupling of quenched in internal stresses. However annealing treatment removes the observed anisotropy. The effect of the annealing on the films depends on the sample's thickness. Surface roughness in case of thinner film annealed at higher temperature is

higher than that of thicker films. Thickness seems to affect coercive field and magnetization behavior more in as deposited state. Higher coercive fields develop more or less for all samples upon crystallization. Ferromagnetic resonance studies on ion beam sputtered were carried out in as deposited state in order to investigate the variation of ferromagnetic resonance frequency as a function of applied magnetic field. Experimental data has been correctly reproduced by Kittel's theory of ferromagnetic resonance. A reasonable agreement among the values of saturation magnetization and anisotropy field has been obtained.

Future work

(1) In order to obtain the experimental evidence of the effect of the presence of random magneto-crystalline anisotropy and annealing induced uniform anisotropies magnetization behavior will be observed at elevated temperatures. It is expected that the contributions of random magneto crystalline anisotropies will increase with increasing working temperature because the averaging will be less effective as a result of reduced exchange interaction at higher temperatures.

(2) The ribbon samples of the studied alloy will be submitted to transverse field annealing in order to induce anisotropy and the effect on the transverse permeability then will be measured by performing the giant magneto impedance measurements.

(3) Magneto optical Kerr effect studies are planned in order to have a detailed knowledge of domain structure of the thin film samples studied by us. Relaxation measurements will also give an idea about the magnetization behavior that can account further for the magnetic behavior of the studied thin film system. Variation of strength of in

plane uniaxial anisotropy with temperature will be monitored by temperature evolution of ferromagnetic resonance.

(4) Films of higher thicknesses will be studied in order to elaborate the thickness dependence of coercive field.

Appendix A

Experimental arrangement of hysteresis loop tracer

The samples in the as cast state were in ribbon form and after being annealed it was difficult to make samples in the form of toroid core. So the investigations of hysteresis properties were carried out on single ribbon samples using single sheet tester technique as depicted in the schematic diagram presented below.

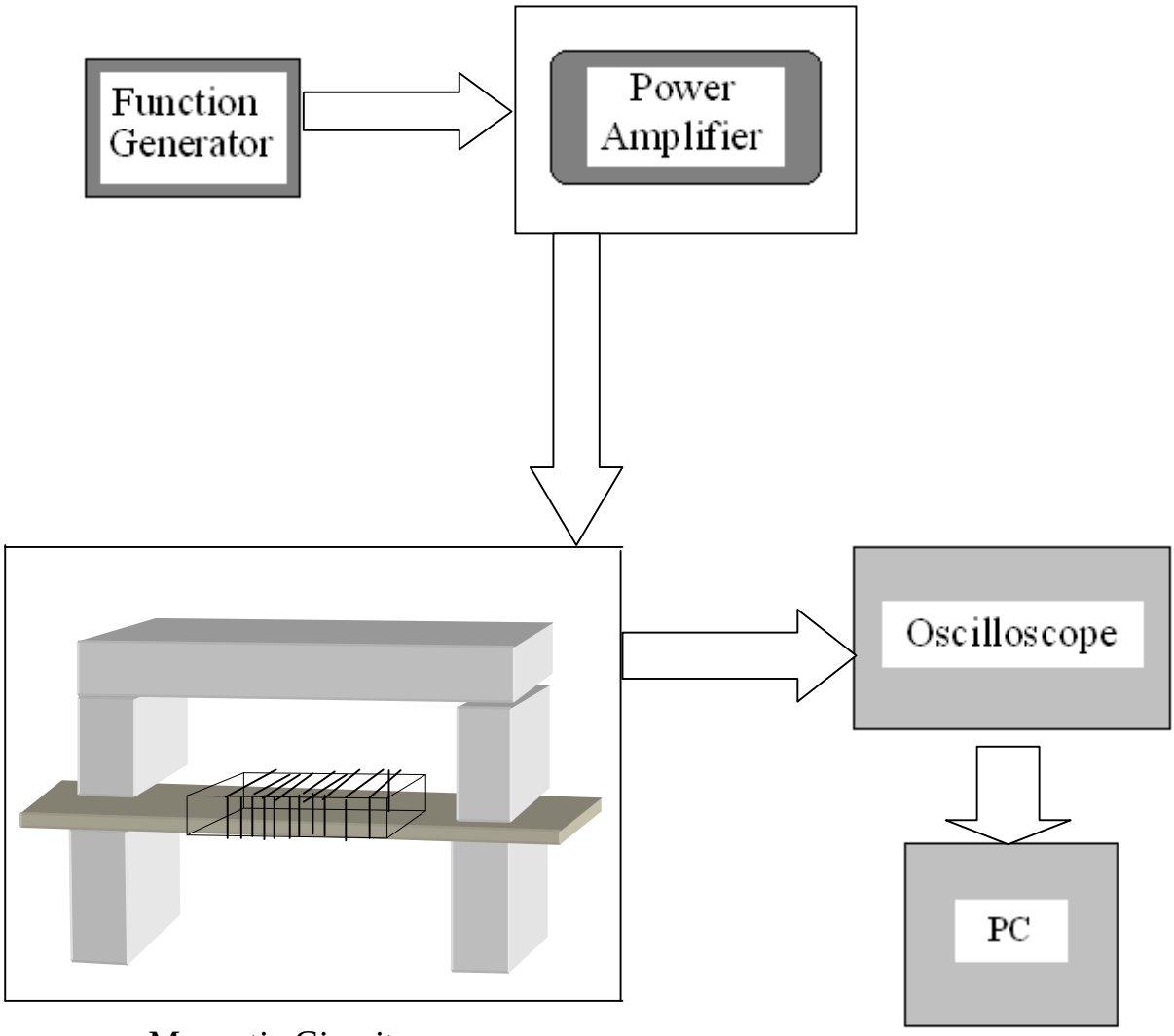

Magnetic Circuit

Appendix B

Second harmonic response of magnetization

It is possible to get information about anisotropy field distribution from the magnetization curve as the distribution of magnetic anisotropies determines the magnetization behavior in amorphous and nanocrystalline alloys. Suppose a soft magnetic alloy having an easy axis perpendicular to the direction of the field and whose anisotropy field is H_k. The magnetization curve is given by:

$$M\ (H,H_k) = M_s \frac{H}{H_k} \qquad if\ 0 \leq H \leq H_k \tag{B.1}$$

$$or\ = M_s \qquad if\ 0 \leq H \leq \infty$$

If a small ac field of amplitude *A* superimposed to a dc field of strength *Ho* acts on the sample, higher-order harmonics develop when

$$H_0 - A < H_k < H_0 + A \tag{B.2}$$

Above situation corresponds to the case where the anisotropy axis is well defined and hence there is single anisotropy field but when a distribution of anisotropy fields exists the magnetization is given by:

$$M\ (H) = M_s \int_0^H P\ (H_k)\, dH_k + M_s H \int_H^\infty \frac{P(H_k)}{H_k}\, dH_k \tag{B.3}$$

If the magnetic field acting on the sample is $H(t) = Ho + A\cos\omega t$, apart from some constant terms eq. (B.3) gives the following time dependent magnetization-

$$M(t) = M_s \int_{H_0}^{H_0 + A\cos\omega t} P(H_k)\, dH_k - M_s H_o \int_{H_0}^{H_0 + A\cos\omega t} \frac{P(H_k)}{H_k}\, dH_k + M_s A\cos\omega t \int_{H_0 + A\cos\omega t}^{\infty} \frac{P(H_k)}{H_k}\, dH_k \qquad (B.4)$$

$M(t)$ is an even, periodic function whose second-harmonic coefficient can be expressed as:

$$a_2(t) = \frac{2\omega}{\pi} M_s \int_0^{\frac{\pi}{\omega}} \left\{ \int_{H_0}^{H_0 + A\cos\omega t} P(H_k) \left(1 - \frac{H_0}{H_k}\right) dH_k + A\cos\omega t \int_{H_0 + A\cos\omega t}^{\infty} \frac{P(H_k)}{H_k}\, dH_k \right\} \cos 2\omega t \qquad (B.5)$$

Partial integration of above equation leads to

$$a_2(t) = -\frac{2\omega}{3\pi} A^2 M_s \int_0^{\frac{\pi}{\omega}} \frac{P(H_0 + A\cos\omega t)}{H_0 + A\cos\omega t} \sin^4 \omega t\, dt \qquad (B.6)$$

If the amplitude of applied static field is much larger than that of the alternating field i.e.

$$H_0 \gg A$$

Then within the above limit second harmonic coefficient given by equation B.6 can be approximated to give

$$|a_2| = \frac{1}{4} M_s A^2 \frac{P(H_0)}{H_0} \qquad (B.7)$$

Above Equation indicates a direct relationship between the second-harmonic coefficient and the anisotropy field distribution $P(H_k)$, which allows the experimental determination of the later. To see the exact relationship between the measured second harmonic voltage and the anisotropy field distribution let us consider that the magnetization can be expressed as:

$$M(t) = M_0 + a_1 \cos\omega t + a_2 \cos 2\omega t + \cdots$$

The flux through the search coil can be expressed as:

$$\emptyset = \mu_0 M(t) N S$$

Where N is the number of turns of pick up coil and S is the cross section of sample.

The induced voltage in the pick up coil will have following temporal dependence:

$$\varepsilon = -\frac{d\emptyset}{dt} = e_1 \sin\omega t + e_2 \sin 2\omega t + \cdots$$

Then, the second-harmonic component is given by;

$$e_2 = 2\mu_0 N S \omega a_2 \qquad (B.8)$$

Then using Eq. (B.7) in the equation above one gets the expression that allows the determination of anisotropy field distribution directly from the measure voltage corresponding to the second harmonic component of magnetization.

$$P(H_0) = 2 \frac{H_0}{\mu_0 M_s N S \omega A^2} e_2$$

Appendix C

Schematic of the experimental arrangement for Giant Magneto Impedance measurement

Giant magneto-impedance (GMI) defined as: $\Delta Z/Z\ (\%) = [Z(H) - Z(H_{max})]/Z(H_{max})\times 100)$ has been studied on as-quenched and annealed samples by means of the 4-contacts technique with an Agilent 4294 A impedance meter, for exciting current frequencies in the range 100 kHz $\leq f \leq$ 30 MHz and under a static longitudinal magnetic field up to H_{max} = 40 kA/m.

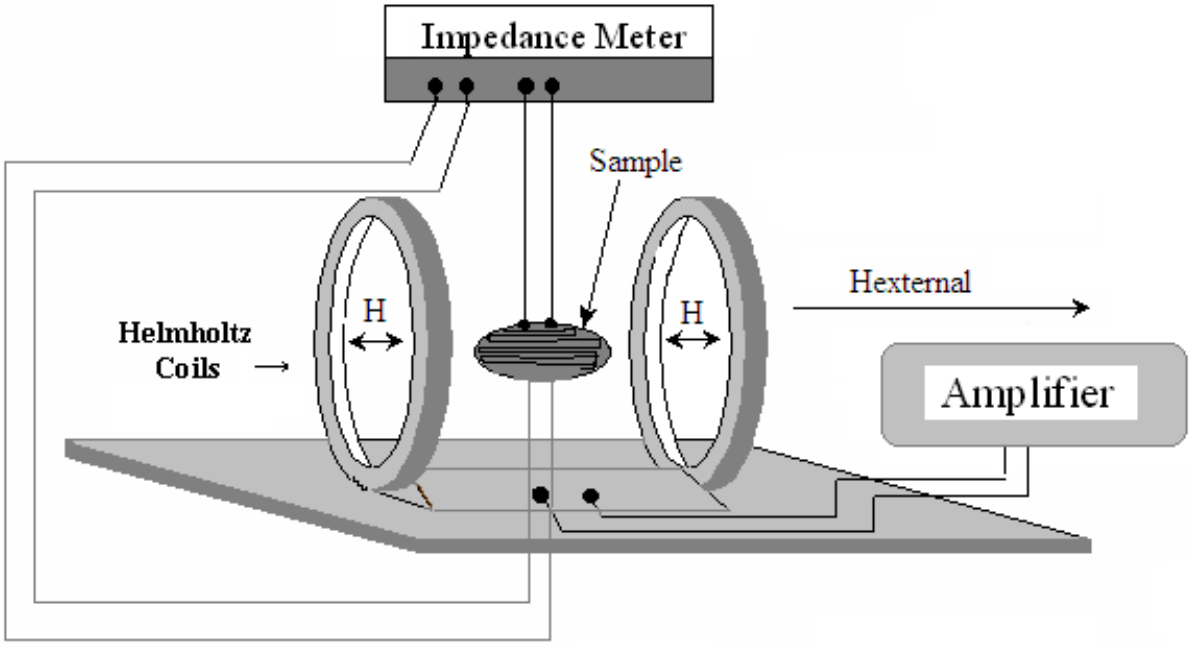

Appendix D

Alternating Gradient Field Magnetometer (AGFM)

Many methods have been devised for the measurement of magnetic moments. They can be divided into two categories: (a) Force techniques which measure the force exerted on a magnetized sample in a magnetic field gradient. The main instrument that is based on this method is the Alternating Gradient Field Magnetometer (AGFM). (b) Inductive techniques that measures the voltage induced by a changing flux. Vibration sample magnetometer is the main instrument that belongs to this category and has been discussed in appendix E. Alternating gradient field magnetometer (AGFM) has enjoyed significant acceptance in present-day magnetic metrology because of its high sensitivity, but great caution must be exercised in its use to avoid large errors in the measurement results. In an AGFM, the sample is mounted to a piezoelectric transducer which oscillates when the sample is subjected to an alternating magnetic field gradient superimposed on the DC field of an electromagnet, as shown schematically in Figure D.1. The object of the AC gradient coils is to produce a homogenous, well-defined alternating field gradient at an accurately controlled frequency. The AGM has a noise floor of 10^{-8} emu compared with 10^{-6} emu for the VSM. However, this factor of 100 is rather not that straightforward in most cases due to the sample size that can be investigated. Although the difference in the signal to noise ratio between VSM and AGFM is usually small but AGFM has significantly superior signal to noise ratio when one wants to measure a very small area sample, which also has very small thickness (1 to 3 nm) and very small magnetization. The measured moment with AGFM, is very sensitive to sample placement due to the gradient field. When measuring low

coercivity samples (~100 Oe or smaller) it is necessary to reduce the magnitude of the gradient field in order to maintain accuracy.

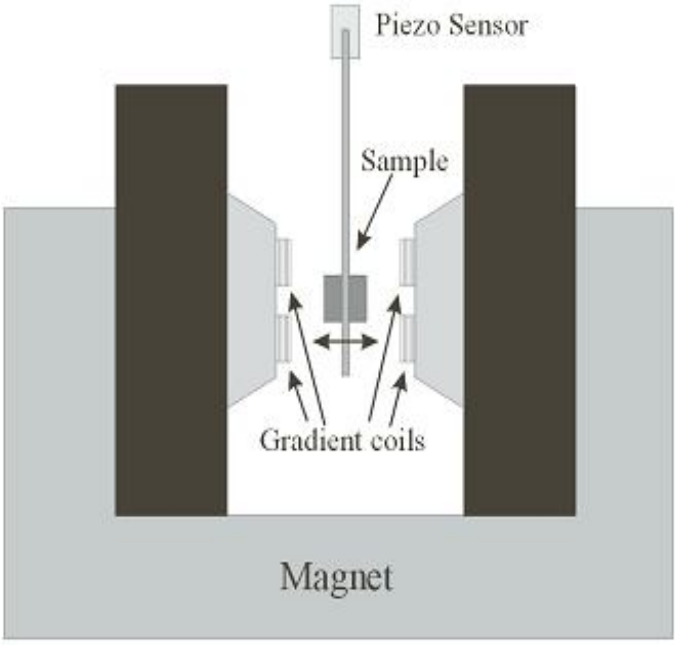

Figure D.1: Schematic of alternating gradient field magnetometer.

The measurements reported in this thesis were carried out using the Princeton measurements corporation model 2900 MicroMag^{TM} alternating gradient field magnetometer.

Appendix E

Vibration Sample Magnetometer (VSM)

The Vibrating Sample Magnetometer (VSM) is the basic instrument for characterizing magnetic materials. Vibration sample magneto meter is the most prevalent example of the magnetometers which employ the inductive technique which measure the voltage induced by a changing flux. Since its invention some forty years ago, it has become the workhorse in both laboratory and production environments for measuring the basic magnetic properties of materials as a function of magnetic field and temperature. Computer control and automation was introduced to the VSM two decades ago, but otherwise there have been no major advancements in performance until quite recently. This quantum improvement in performance has been imposed by the advancements in magnetic recording storage systems and, more specifically, by the advanced magneto-resistive and spin valve heads and the high coercivity and low remanence thickness product media employed in these systems. The magnetic layer(s) in these advanced heads and media have very low magnetic moment per unit area, requiring significantly improved sensitivity and high signal to noise ratio magnetic metrology tools. The VSM, shown schematically in Figure E.1, employs an electromagnet which provides the magnetizing field (DC), a vibrator mechanism to vibrate the sample in the magnetic field, and detection coils which generate the signal voltage due to the changing flux emanating from the vibrating sample. The output measurement displays the magnetic moment M as a function of the applied field H. The magnetic field is usually generated by an electromagnet driven by a DC bipolar power supply. If extremely high magnetic fields are required (> 3 Tesla), the electromagnet is replaced by a superconducting solenoid which significantly increases the operational cost and the time of

the measurements and adversely affects the convenience of use. The magnetic field is usually measured by a Hall-effect device in a computer-controlled feedback loop. The field of the electromagnet is controlled either indirectly by adjusting the target current in the electromagnet or by directly adjusting the field in a feedback loop. The relationship between experimental parameters that facilitates the experimental determination of magnetic moment per unit mass (σ) of the sample is given as:

$$\sigma \propto V/(f.m)$$

Where V is the amplitude of induced voltage, f is the frequency of vibration and m is the mass of the sample.

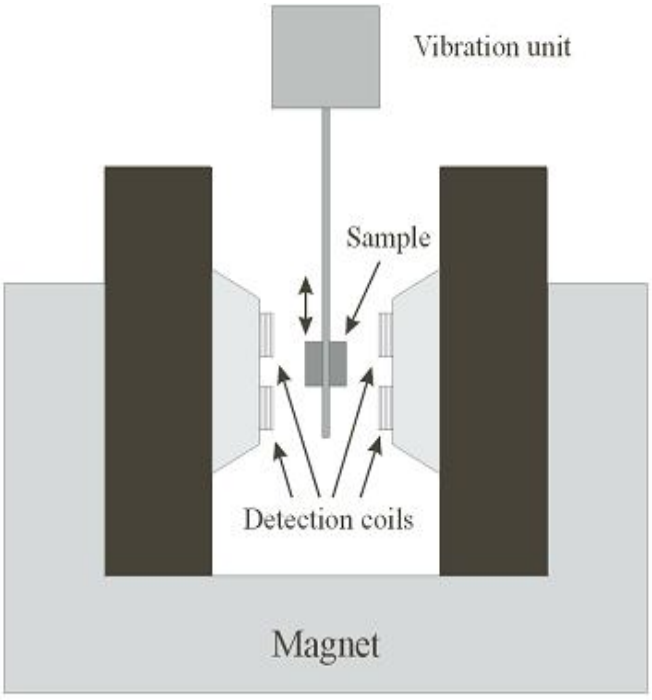

Figure E.1: Schematic of a vibrating sample magnetometer.

Appendix F

Ferromagnetic Resonance

Ferromagnetic resonance is basically referred to the collective excitation of an ensemble of electron spin magnetic moments present in a magnetic material. Existence of both mechanical and magnetic moments of electron leads to the phenomena in presence of magnetic field which can be considered as that of behaviour of a mechanical top in a gravitational field. The electron experience a torque (T) which tries to align the magnetic moment μ_B along the external magnetic field H

$$\boldsymbol{T} = \mu_o \boldsymbol{\mu}_B \boldsymbol{H}$$

This torque also produces a change in the mechanical moment of electron

$$\boldsymbol{T} = d\boldsymbol{J} / dt$$

If $\boldsymbol{J}$ is not parallel to $\boldsymbol{H}$ than above equation states that there will be a precession of $\boldsymbol{J}$ and $\boldsymbol{\mu}_B$ around $\boldsymbol{H}$ i.e.

$$d\boldsymbol{\mu}_B = \gamma_0 \, (\boldsymbol{H} \, \boldsymbol{\mu}_B) \, dt$$

where γ_0 is gyromagnetic ratio ($g \, \mu_B / \hbar$). As at any moment $d\mu_B$ *is* perpendicular to plane containing ($\boldsymbol{H}$, $\boldsymbol{\mu}_B$), so $\boldsymbol{\mu}_B$ moves in a circle around $\boldsymbol{H}$ as shown in figure F.1. The direction of rotation is always determined by right hand rule. The total magnetization in a system of magnetically aligned spins or magnetic moment per unit volume is given by the product of number of electrons with uncompensated magnetic moments per unit volume and $\boldsymbol{\mu}_B$. The macroscopic equation of motion of magnetization vector is given by:

$$\mathrm{d}\boldsymbol{M} / \mathrm{dt} = - \gamma \, (\boldsymbol{M} \times \boldsymbol{H}) - [\lambda \, (\boldsymbol{M} \times (\boldsymbol{M} \times \boldsymbol{H}))] / \mid \mathrm{M}^2 \mid$$

The second term on right hand side of above equation is the damping term that represents

a torque that acts so as to reduce the angle of precession. In above equation of motion $\boldsymbol{H}$ represents the vector sum of all magnetic fields as seen by spinning electrons. Consider a ferromagnetic sample in the form of a ellipsoid with demagnetization factors N_x, N_y, N_z. The external applied field is in z direction. Then the components of the internal magnetic field can be written as;

$$H_{ix} = H_x^{\,0} - N_x M_x$$

$$H_{iy} = H_y^{\,0} - N_y M_y$$

and $$H_{iz} = H_z^{\,0} - N_z M_z$$

where H^i denotes the internal effective magnetic field that includes anisotropy fields and demagnetizing field and H^0 is applied magnetic field.

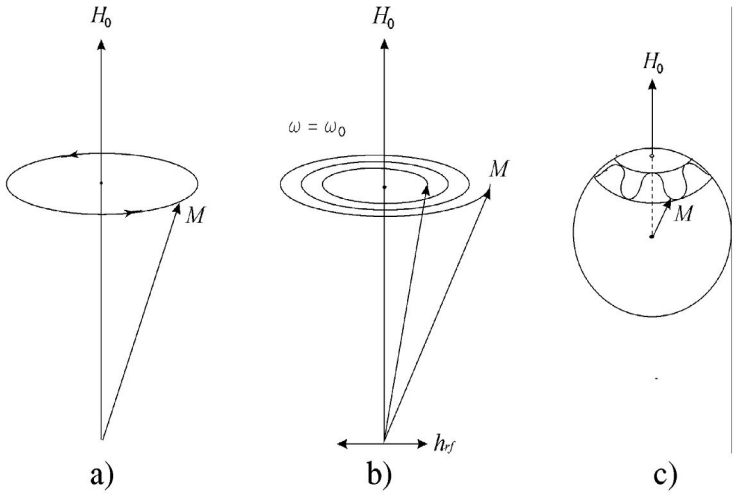

Figure F.1: The precession of the magnetization vector M in **(a)** a constant magnetic field, **(b)** and **(c)** when the frequency of the applied alternating magnetic field (h_f) is near to the natural frequency of precession.

The components of the equation of motion of magnetization for static magnetic field then become;

$$dM_x / dt = \gamma [H_{eff}^0 + (N_y - N_z) M] M_y$$

$$dM_y / dt = \gamma [H_{eff}^0 + (N_x - N_z) M] M_x$$

To first order $dM_z / dt = 0$ and $M_z = M_s$ and ferromagnetic resonance frequency is presented as :

$$\omega_0^2 = \gamma^2 [H_{eff}^0 + (N_y - N_z) M_s] \times [H_{eff}^0 + (N_x - N_z) M_s]$$

In case of thin film with magnetic field applied parallel to the plane of the film $N_x = N_z = 0$ and $N_y = 1$ above equation yields ferromagnetic resonant frequency as:

$$\omega_0^2 = \gamma^2 [H_{eff}^0 (H_{eff}^0 + M_s)]$$

List of Publications

a) Published papers in SCI Journals

[1] "Study of magnetic properties and relaxation in amorphous $Fe_{73.9}Nb_{3.1}Cu_{0.9}Si_{13.2}B_{8.9}$ thin films produced by ion beam sputtering"

F. Celegato, M. Coisson, A. Magni, P. Tiberto, F. Vinai, S. N. Kane, **S. S. Modak**, A. Gupta and P. Sharma, J. Appl. Phys. 102 (2007) 043916.

[2] "Structural and magnetic investigation of gradually divitrified nanoperm alloys"

S. S. Modak, N. Ghodke, B. Rathore, F. Mazaleyrat, M. Lo Bue, L. K. Varga , A. Gupta and S. N. Kane, J. Magn. Magn. Mater. 320 (2008) e828.

[3] "Effect of Annealing on Magnetic and Magnetotransport Properties of $Fe_{84}Zr_{3.5}Nb_{3.5}Cu_8B_1$ Ribbons"

F. Celegato, M. Coïsson, S. N. Kane, F. Mazaleyrat, **S. S. Modak**, P. Tiberto, L. K. Varga, F. Vinai, Physica Status Solidi a 205 (2008) 1749.

[4] "Penetration depth and magnetic permeability calculations on GMI effect and comparison with measurements on CoFeB alloys"

M. Coisson, P. Tiberto, F. Vinai, P. V. Tyagi, **S. S. Modak**, S. N. Kane,

J. Magn. Magn. Mater 320 (2008) 510.

b) Presentation in international conference

[1] **"**Departure from random anisotropy mechanism in soft magnetic nanocrystalline $Fe_{58}Co_{25}Nb_7Cu_1B_9$ alloy",

S. S. Modak, S. N. Kane, F. Mazaleyrat, M. Lo Bue and L. K. Varga,

J. Magn. Magn. Mater. (Under review), Presented in Joint European Magnetic Symposia (JEMS'08), September 14 – 19, 2008, Dublin, Ireland.

c) Papers in national conference proceedings (In a book with ISBN)

[1] In-situ resistance measurement and Joule heating set-up for studying structural transformation in amorphous alloys"

S. S. Modak, S. S. Khinchi, Nandkishor Ghodke, A. Gupta and S. N. Kane

Proceedings of DAE Solid State Physics Symposium vol. 51 (2006) p 343,

Ed. K. G. Bhushan, A. Das and S. K. Gupta, Prime Time Education, Mumbai, India,

ISBN: 81-8372-030-7.

[2] "Wall pinning in devitrified soft magnetic nanocrystalline materials"

S. S. Modak, F. Mazaleyrat, Zs. Gercsi, L. K. Varga, D. Rodionov and S. N. Kane

Proceedings of DAE Solid State Physics Symposium vol. 51 (2006) p 835,

Ed. K. G. Bhushan, A. Das and S. K. Gupta, Prime Time Education, Mumbai, India,

ISBN: 81-8372-030-7.

[3] "Identification of Jiles-Atherton Parameters in Co-based alloys"

B. Rathore, **S. S. Modak** and S. N. Kane

Proceedings of DAE Solid State Physics Symposium vol. 51 (2006) p 837,

Ed. K. G. Bhushan, A. Das and S. K. Gupta, Prime Time Education, Mumbai, India,

ISBN: 81-8372-030-7.

[4] **"**A new grain size and volume fraction dependence of coercive field in soft magnetic nanoCrystalline Alloys"

S. N. Kane, **S. S. Modak**, S. S. Khinchi, L. K. Varga

Proc. of DAE Solid State Physics Symposium vol. 52 (2007) 305,

Eds. A. Das, M. Sunder, S. K. Gupta, Krystal Print Products, Mumbai, India,

ISBN: 81-8372-035-8.

d) Papers to be published in SCI journals

[1] "Influence of Co content and thermal annealing on structural, magnetic and magneto elastic properties of nanocrystalline Fe-Co-Nb-B alloys"

S. S. Khinchi, **S. S. Modak**, L. Kraus, P. Svec, F. Mazaleyrat and S. N. Kane

[2] "Study of magneto-impedance, skin effect and transverse permeability of $Co_{55}Fe_{23}Si_{10}B_{12}$ metallic glass ribbons"

F. Celegato M. Coïsson, S.N. Kane, P.V. Tyagi, **S.S. Modak**, N. Ghodke, F. Celegato, P. Tiberto, F. Vinai and H. K. Lachowicz